Optimisation de la position d'un système houlomoteur : étude comparative des impacts de vagues et de la ressource disponible.

Ximun Lastiri

▶ **To cite this version:**

Ximun Lastiri. Optimisation de la position d'un système houlomoteur : étude comparative des impacts de vagues et de la ressource disponible.. Génie civil. Université de Pau et des Pays de l'Adour, 2023. Français. NNT : 2023PAUU3096 . tel-04737333

HAL Id: tel-04737333

https://theses.hal.science/tel-04737333v1

Submitted on 15 Oct 2024

HAL is a multi-disciplinary open access archive for the deposit and dissemination of scientific research documents, whether they are published or not. The documents may come from teaching and research institutions in France or abroad, or from public or private research centers.

L'archive ouverte pluridisciplinaire **HAL**, est destinée au dépôt et à la diffusion de documents scientifiques de niveau recherche, publiés ou non, émanant des établissements d'enseignement et de recherche français ou étrangers, des laboratoires publics ou privés.

Optimization of the localization of a wave energy converter : cross analysis of wave energy resource versus wave loading

Par:

Ximun LASTIRI

Thèse présentée à l'Université de Pau et des Pays de l'Adour pour obtenir le grade de docteur en génie civil

Après avis de :

Jean-François FILIPOT ..... Rapporteur
Philippe SERGENT ..... Rapporteur

Devant la commission d'examen formée de :

Stéphane ABADIE ..... Directeur de thèse
Volker ROEBER ..... Directeur de thèse
Matthias DELPEY ..... Co-encadrant de thèse
Gregory PINON ..... Examinateur

Soutenue le : 20/12/2023

Optimization of the localization of a wave energy converter : cross analysis of wave energy resource versus wave loading

Author:
Ximun LASTIRI (SIAME, Université de Pau et des Pays de l'Adour)

Supervisors:
Stéphane ABADIE (Directeur de thèse)
Volker ROEBER(Directeur de thèse)
Matthias DELPEY(Co-encadrant de thèse)

Abstract

Wave energy conversion is considered as one of the possible marine renewable energy contributions to a sustainable energy mix in the future. One of the key aspects of a wave energy project is the location of the devices that will harvest the wave energy : the Wave Energy Converters (WECs). This location should answer to different objectives such as a high level of electrical production, low risk levels for the WECs, low environmental impacts, and social acceptance among others. In this context, the goal of this PhD is to develop a methodology to optimize the localization of WECs in the nearshore domain. This work will tackle two of the aforementioned objectives : the utilization of the resource and the risk of catastropic failure.

This manuscript is divided into eight chapters. After a short introduction, the second chapter aims at introducing the basic concepts of wave modeling and computing necessary to understand the manuscript. In Chapter 3, a literature review is carried out to present the current state of the art and to define the scientific questions that are addressed later on. Chapter 4 presents the construction and analysis of a 44-year wave energy hindcast over the South Aquitaine nearshore area. This hindcast was built with the numerical code SWAN. The spatio-temporal variability of the wave energy resource is studied throughout this chapter. Chapter 5 specifically addresses two reasons for the variability observed in Chapter 4. First, the influence of the Capbreton submarine canyon on the nearshore variability is studied. Then, a WEC's estimated energy output is obtained from two calculation methods. After that, Chapter 6 focuses on the survivability aspect of the WECs. First, long term sea state parameters are derived from environmental contours. Then the loads are studied over the complete domain thus giving valuable knowledge on the hazard that the WECs could face in the area. The philosophy behind this methodology is to compute loads from the wave hindcast's statistical parameters. This ensures that the methodology developed here, is applicable to areas where the full spectral information of the sea states is not available. The spatial variability of the loading is then studied and the influence of the hindcast size and the return period analyzed. Finally, Chapter 7 studies the relation between the resource and the the loading and proposes indexes that qualify a point with respect to its quality for WEC installation. A last chapter will finally summarizes the work and present an outlook beyond this PhD.

Résumé de la thèse

L'énergie houlomotrice est une des énergies marines renouvelables permettant d'assurer un mix énergétique soutenable pour le futur. Un des aspects essentiels de tout projet houlomoteur est de toute évidence la localisation des convertisseurs d'énergie houlomotrice (WEC en anglais). Elle doit répondre à plusieurs critères parmi lesquels le niveau de production électrique, l'aléa pour les convertisseurs, l'impact environnemental ou bien l'acceptation sociale du projet. Le but de ces travaux de recherche est donc de présenter une méthodologie d'optimisation de la position de convertisseurs houlomoteurs dans une zone côtière. Ces travaux s'intéressent à deux des aspects évoqués plus haut : la production électrique des convertisseurs et l'aléa associé aux impacts de vagues.

Le manuscrit est divisé en 8 chapitres. Après une brève introduction, le second chapitre vise à introduire les concepts basiques associés à la modélisation des vagues ainsi qu'au calcul numérique de ces dernières. Une revue de la bibliographie est effectuée dans le chapitre 3 en vu de présenter l'état de l'art et de définir les questions scientifiques. Le chapitre 4 présente la construction et l'analyse d'une base de données d'états de mer d'une durée de 44 ans sur l'ensemble de la côte Sud-Aquitaine. Ce rejeu de données a été construit à l'aide du code numérique SWAN. La variabilité spatio-temporelle de la ressource en énergie houlomotrice est mise en évidence tout au long du chapitre. Le chapitre 5 s'attache à répondre aux questionnements mis en évidence par le Chapitre 4, notamment les raisons de la variabilité de la ressource (i.e. l'influence du gouf sous-marin de Capbreton) et de la production d'un convertisseur houlomoteur via la comparaison de deux méthodes.

Le chapitre 6 étudie ensuite la survivabilité des convertisseurs. Dans un premier temps, des états de mers extrêmes sont déduits des contours environnementaux associés à des périodes de retour. La force associée aux impacts de vagues est ensuite calculée sur l'ensemble du domaine, donnant ainsi une information importante vis-à-vis du risque encouru par un convertisseur dans une zone donnée. La philosophie derrière cette méthodologie est de permettre le calcul des forces d'impacts à partir des paramètres statistiques du rejeu de données. Cela permettra d'appliquer la méthodologie développée ici à des zones pour lesquelles on ne dispose pas a priori d'information spectrale sur l'état de mer. La variabilité spatiale des forces d'impacts est ensuite étudiée ainsi que l'influence de la taille du rejeu de données utilisée et de la période de retour choisie. Enfin, le chapitre 7 étudie la relation entre la ressource houlomotrice et les impacts de vagues en proposant des indices qualifiant un point par rapport à sa pertinence pour un projet houlomoteur. Un dernier chapitre de conclusion résume le travail effectué et présente les perspectives de ces travaux.

Acknowledgements

As my PhD comes to an end I want to express my deepest gratitude to everyone who helped me get there.

I want to thank first all the teachers who have taught me over the years, this could not have been possible without you.

Then, I wish to thank all my PhD supervisors. This PhD journey started with Stéphane Abadie trusting me. His help and continuous support have helped me get to the finish line, for that I will ever be grateful. I also wish to thank Volker Roeber who integrated me in the HPC-Waves chair team. His expertise was a valuable asset for this PhD. Finally, I would also like to thank Matthias Delpey who always took the time to share his SWAN knowledge.

These four years would not have been the same without the people I had the pleasure to work with. I wish to thank all my fellow doctoral students and members of the SIAME laboratory, who were always of good support and advice. I also want to thank all the ISA BTP team, you made the day to day life much more lighter. To all the students I had the pleasure to teach, thank you, although you did not always made the things easy, you made me the teacher I am today, for that I am grateful.

I would also like to thank my friends and family. Without you I probably would have quit a million times. I can't thank you enough for keeping faith in me and for showing me the path to follow.

Finally, thank you Charlie for always being there and for your continuous support during this period of our lives.

Bihotzetik milesker deneri.

List of Symbols

MWL	Mean Water Level
H	Wave height
η	Water surface elevation from MWL
L	Wave length
T	Wave period
h	Wave depth
$c = \frac{L}{T}$	Phase velocity
$k = \frac{2\pi}{L}$	Wave number
$\omega = \frac{2\pi}{T}$	Angular frequency
u	Horizontal particle velocity
w	Vertical particle velocity

Contents

Chapter 1

Introduction

1.1 Context

Due to the increase of greenhouse gas concentration, one of today's biggest challenges mankind is facing is the fight against global warming. As electricity and heat production account for a large part of the CO_2 emissions (Figure 1.1), the reduction of its carbon footprint is mandatory to meet the objectives that policymakers set. Among other solutions, developing renewable energies could be a way to reduce the use of fossil fuels. As part of the European effort to reduce fossil energy production, the French government set the target of a 32% share of Renewable Energy in the national final energy mix for year 2030 [French-Government 2017]. This stands for an important challenge for the country, which national production of electricity ranged from 400 to 600 TWh/year during the last ten years [RTE 2019].

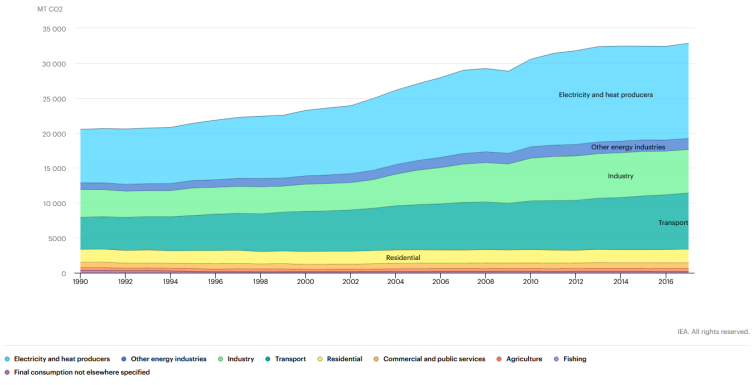

Figure 1.1: World CO_2 emissions by sector between 1990 and 2017. Source: https://www.iea.org

Wave energy conversion is considered as one of the possible marine renewable energy contributions to a sustainable energy mix in the future. France has a very long coastline of about 2400 km, which was shown to offer a significant wave energy resource [Boudière et al. 2013]. The wave energy

resource is quite well distributed along the shoreline as opposed to, e.g., tidal energy where only a few hotspots are suitable for installation. Additionally, available wave energy during the year is usually the highest when the energy demand is also high, i.e., in winter.

1.2 A little while back

Harvesting the wave energy is not a new idea. Indeed, technologies have been developed since at least 1799 when Mr Girard and his son filed a patent (see Figure 1.2) to develop the first ideas for Wave Energy Converters (WECs). This patent listed several ideas for wave energy conversion, including the first sketches of bottom-fixed heave buoy array.

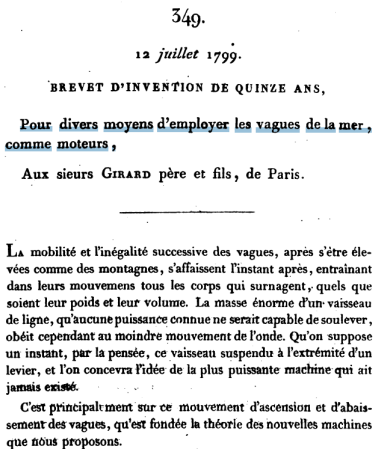

349.

12 *juillet* 1799.

BREVET D'INVENTION DE QUINZE ANS,

Pour divers moyens d'employer les vagues de la mer, comme moteurs,

Aux sieurs GIRARD père et fils, de Paris.

LA mobilité et l'inégalité successive des vagues, après s'être élevées comme des montagnes, s'affaissent l'instant après, entraînant dans leurs mouvemens tous les corps qui surnagent, quels que soient leur poids et leur volume. La masse énorme d'un vaisseau de ligne, qu'aucune puissance connue ne serait capable de soulever, obéit cependant au moindre mouvement de l'onde. Qu'on suppose un instant, par la pensée, ce vaisseau suspendu à l'extrémité d'un levier, et l'on concevra l'idée de la plus puissante machine qui ait jamais existé.

C'est principalement sur ce mouvement d'ascension et d'abaissement des vagues, qu'est fondée la théorie des nouvelles machines que nous proposons.

Figure 1.2: Patent introduction of Girard and son for their WEC idea

In France other projects became a reality. Some of them were small scale project, like the device build by Bochaux-Praceique to power his house, which had a power of 1 kW ([Leishman and Scobie 1976]). Others were of higher magnitude such as the maritime hydrodynamic laboratory installed beneath the lighthouse of Biarritz, France (see Figure 1.3). The project of the french engineer Paul Grasset, consisted in the combination of a ram-pump and the oscillations of the waves. However, due to the economic crisis and World WAR II, the project was abandoned.

Throughout the end of the XX^{th} century, researchers refined various wave energy technologies, such as point absorbers, attenuators, and oscillating water columns, leading to several prototype deployments. Among them, one can cite the LIMPET in Scotland (Figure 1.4), first built in 1991, which was the world's first commercial wave power device ([Heath 2003]).

The 21st century witnessed an increased focus on sustainability, driving investments and research in the field. By the 2010s, a shift towards commercialization became evident with wave energy projects like the Pelamis in Portugal ([Yemm et al. 2023]) and the Carnegie Wave Energy Project in Australia ([Carnegie].

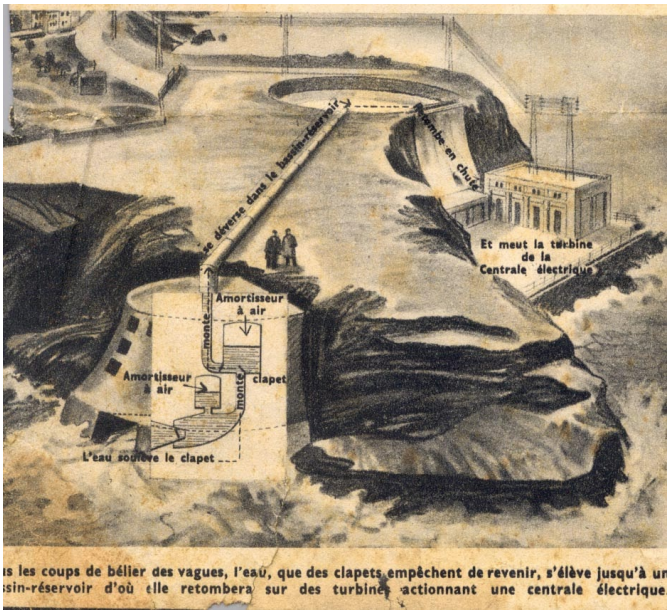

Figure 1.3: Simplified sketch of the WEC project beneath the lighthouse of Biarritz, France

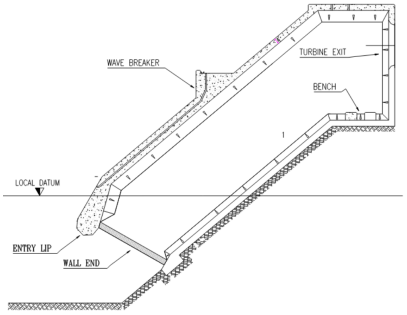

Figure 1.4: (a) Close up view of the seaward face of LIMPET (b) Section through LIMPET Collector from [Heath 2009]

1.3 Challenges

One of the key aspect of a wave energy project is obviously its location. It should answer to different objectives such as a high level of electrical production, low risk levels for the WECs, low environmental impacts, social acceptance among others. The goal of the PhD is to propose a methodology to optimize the localization of WECs over a nearshore area. This work will tackle two of the aforementioned objectives : the resource and the hazard.

1.4 Outline

This manuscript is divided into eight chapters. The first one is a quick introduction. Answering the questions that will be raised over the course of this manuscript requires understanding of the physics of ocean wave motions. Therefore, Chapter 2 introduces the basic knowledge on wave modelling and computing. In Chapter 3, a literature review is carried out, to present the current state of the art and define the scientific questions that are addressed later on.

Chapter 4 presents the construction and analysis of a 44-year wave energy hindcast over the South Aquitaine nearshore area. This chapter raises additional questions on the variability of the wave energy resource. Chapter 5 first addresses the reasons behind the wave energy resource variability, by studying first the influence of wave forcing, and then, the influence of a major bathymetric feature, the Capbreton's submarine canyon. The variability of the estimated energy output of a WEC is also addressed, by comparing two computation methods, highlighting the interest of having the spectral information.

Chapter 6 focuses on the survivability aspect of the WECs. Wave impact loads are computed from the wave hindcast's statistical parameters. This will ensure that the methodology developed here is applicable to areas where the full spectral information of the sea states is not available. The loads are studied over the complete domain thus giving valuable knowledge on the hazards that the WECs could face in the area.

Finally, Chapter 7 aims at studying the relation between the resource and the loading by proposing indexes that qualify a point with respect to its quality for WEC installation. A last chapter finally summarizes the work conducted during the PhD and present the perspectives that are open.

Chapter 2

Modeling and computing of ocean waves

Understanding the physics and dynamics of ocean waves is a fundamental endeavor in the field of oceanography, with broad implications for a wide range of interdisciplinary research areas. In this chapter, we explore the various methods and models used to simulate and predict the behavior of ocean waves.

This begins by discussing the basic physics of ocean waves, including both monochromatic and irregular waves. Then mathematical models used to simulate ocean waves are explained, followed by an introduction to the numerical methods used to solve these models.

2.1 Modelling ocean waves

Ocean waves are dynamic disturbances that propagate across the surface of Earth's oceans, driven primarily by the wind's interaction with the water. These waves are characterized by their periodic rise and fall, creating a complex interplay of energy transfer and motion. Ocean waves are created offshore and then propagate towards the shore. Wave propagation is driven by many phenomena such as refraction, diffraction, or shoaling among others and those phenomena are in turn driven by the characteristics of the waves such as the wave height, the wave period or the water depth (see Figure 2.1). This section of this manuscript is a summary from the MSc course of [Abadie], which is itself based on [Dean and Dalrymple 1984]

2.1.1 Linear wave theory

By making the hypothesis that the boundary layer is thin enough, we can consider that the flow is irrotational (i.e. $\vec{rot}(\vec{V}) = 0$) and assume that waves can be described as potential flow.

Continuity equation

We assume here that the fluid is incompressible with constant density. This assumption is valid in most cases except in the presence of strong salinity gradient or in the case of breaking waves (due to the introduction of air bubbles).

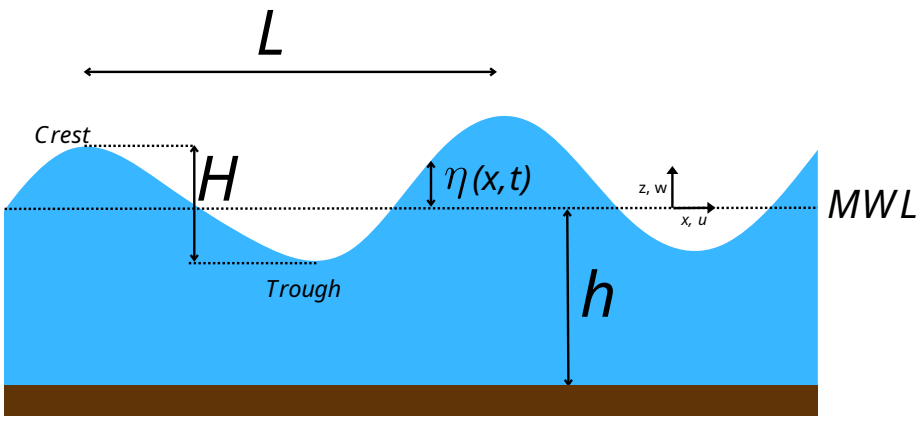

Figure 2.1: Parametrization of the free surface

$$\frac{\partial u}{\partial x} + \frac{\partial w}{\partial z} = 0 \text{ or } div(\vec{v}) = 0 \tag{2.1.1}$$

Laplace equation

Considering that the flow is irrotational, the continuity equation (2.1.1) can be written with the velocity potential ϕ, finally becoming the Laplace equation.

$$\frac{\partial^2 \phi}{\partial^2 x} + \frac{\partial^2 \phi}{\partial^2 z} = 0 \tag{2.1.2}$$

Boundary conditions

Kinematic bottom boundary condition

Considering the bottom as impermeable, there can not be vertical flow at the bottom.

$$\frac{\partial \phi}{\partial z} = 0 \Big|_{z=-h} \tag{2.1.3}$$

Kinematic free surface condition

By writing the relation between the particle velocity at $z = \eta$ and the vertical velocity of the surface, we obtain the following equation. :

$$w = \frac{\partial \eta}{\partial t} + u \frac{\partial \eta}{\partial x} \tag{2.1.4}$$

Dynamic free surface condition

The dynamic free surface condition consists in expressing the fact that the pressure along the free surface must be equal to the atmospheric pressure. Using the Bernoulli equation, we obtain the following equation :

$$-\frac{\partial \phi}{\partial t} + \frac{1}{2}(u^2 + w^2) + \frac{P_{atm}}{\rho} + gz = C(t) \text{ at } z = \eta(x,t) \tag{2.1.5}$$

Periodicity condition

We suppose a progressive wave that is periodic of constant form. This requirements writes :

$$\phi(x,t) = \phi(x+L,t) = \phi(x,t+T) \tag{2.1.6}$$

Linear theory solution

First we make the assumption that the potential is the product of three functions, each one depending on only one function.

$$\phi(x,z,t) = X(x).Z(z).\tau(t) \tag{2.1.7}$$

Since we know that ϕ is periodic in T, and that it appears only in the function τ let's assume that :

$$\tau(t) = sin(\omega t) = sin(2\pi \frac{t}{T}) \tag{2.1.8}$$

The Laplace equation (2.1.2) is then,

$$\frac{\partial^2 X(x)}{\partial x^2}.Z(z).sin(2\pi \frac{t}{T}) + X(x).\frac{\partial^2 Z(z)}{\partial z^2}.sin(2\pi \frac{t}{T}) = 0 \tag{2.1.9}$$

Or,

$$\frac{1}{X}.\frac{\partial^2 X(x)}{\partial x^2} + \frac{1}{Z}.\frac{\partial^2 Z(z)}{\partial z^2} = 0 \tag{2.1.10}$$

The two elements of equation (2.1.10) are necessarily constant values of opposite signs such as :

$$\frac{1}{X}\frac{\partial^2 X(x)}{\partial x^2} = -k^2 \tag{2.1.11}$$

and,

$$\frac{1}{Z}.\frac{\partial^2 Z(z)}{\partial z^2} = +k^2 \tag{2.1.12}$$

We then obtain :

$$X(x) = Acos(kx) + Bsin(kx) \tag{2.1.13}$$

$$Z(z) = C.exp(kz) + D.exp(-kz) \tag{2.1.14}$$

The potential is now :

$$\phi(x,z,t) = (Acos(kx) + Bsin(kx))(C.exp(kz) + D.exp(-kz))(sin(\omega t)) \tag{2.1.15}$$

The periodicity of the function is achieved by considering $k = \frac{2\pi}{L}$ and by keeping only $Acos(kx)$. We write the bottom boundary condition (2.1.4), with the potential found in equation (2.1.15).

$$-Acos(kx)\left(k.C.exp(kz) - D.exp(-kz)\right) sin(\omega t) = 0 \text{ at z=-h} \tag{2.1.16}$$

Which gives,

$$C = D.exp(2kh) \tag{2.1.17}$$

Using the free surface conditions is a little more complex since, the free surface itself is unknown. First for the dynamic free surface condition, let's apply a Taylor series expansion to the left hand term of Bernoulli's equation (2.1.5) with $P_{atm} = 0$ (relative pressures) for $z = \eta$.

$$-\frac{\partial\phi}{\partial t}+\frac{1}{2}(u^2+w^2)+gz\Big|_{z=\eta} = -\frac{\partial\phi}{\partial t}+\frac{1}{2}(u^2+w^2)+gz = C(t)\Big|_{z=0} +\eta\left(\frac{1}{2}(u^2+w^2)+gz = C(t)\Big|_{z=0}\right)+... = C(t) \tag{2.1.18}$$

Given the hypothesis that waves are infinitely small, one can assume that $\eta, u, w, P << 1$. The product of these quantities is then negligible, which gives :

$$-\frac{\partial\phi}{\partial t}\Big|_{z=0} + g\eta = C(t) \tag{2.1.19}$$

And,

$$\eta = \frac{1}{g}(\frac{\partial\phi}{\partial t}\Big|_{z=0}) + \frac{C(t)}{g} \tag{2.1.20}$$

Substituting the expression of the potential :

$$\eta = \left(\frac{G.\omega}{g}cos(kx)cosh(k(h+z))cos(\omega t)\Big|_{z=0}\right) + \frac{C(t)}{g} \tag{2.1.21}$$

Or,

$$\eta = \left(\frac{G.\omega.cosh(kh)}{g}cos(kx)cos(\omega t)\right) + \frac{C(t)}{g} \tag{2.1.22}$$

Since η has a spatial and temporal mean value equal to zero we have $C(t) = 0$. By introducing the wave height as $H = \frac{2\omega.Cosh(kh)}{g}$ we obtain the final expression of the free surface.

$$\eta = \frac{H}{2}cos(kx)cos(\omega t) \tag{2.1.23}$$

From equation (2.1.23), we deduce the expression of the potential of velocities :

$$\phi = \frac{H.g.cosh(k(h+z))}{2.\omega.cosh(kh)}cos(kx)sin(\omega t) \tag{2.1.24}$$

Using the kinematic free surface condition will allow us to have a relation between the wavelength, the wave period and the depth. As we did for the dynamic free surface boundary condition we apply a Taylor development of the boundary condition at $z = \eta(x, t)$.

$$(w - \frac{\partial\eta}{\partial t} - u\frac{\partial\eta}{\partial x})\Big|_{z=\eta} = (w - \frac{\partial\eta}{\partial t} - u\frac{\partial\eta}{\partial x})\Big|_{z=0} + \eta\frac{\partial}{\partial z}(w - \frac{\partial\eta}{\partial t} - u\frac{\partial\eta}{\partial x})\Big|_{z=0} + ... = 0 \tag{2.1.25}$$

Assuming that $\eta << 1$ all products with this quantity equals to 0. So we have :

$$w = \frac{\partial \eta}{\partial t}\bigg|_{z=0} \tag{2.1.26}$$

However η does not depend on z, so :

$$(-\frac{\partial \phi}{\partial z})\bigg|_{z=0} = \frac{\partial \eta}{\partial t} \tag{2.1.27}$$

By substituting the expression of ϕ and η from equation (2.1.24) and (2.1.23) we obtain the following equation, called the dispersion relation.

$$\omega^2 = g.k.tanh(kh) \tag{2.1.28}$$

Velocity components for a progressive wave

We consider the following progressive wave with water elevation given by :

$$\eta = \frac{H}{2} cos(kx - \omega t) \tag{2.1.29}$$

With the associated velocity potential :

$$\Phi = \frac{H}{2}\frac{g}{\sigma}\frac{cosh(k(h+z))}{cosh(kh)} sin(kx - \omega t) \tag{2.1.30}$$

By introducing the dispersion relation (Equation 2.1.28), we obtain the following velocity potential :

$$\Phi = \frac{H}{2}\frac{\sigma}{k}\frac{cosh(k(h+z))}{sinh(kh)} sin(kx - \omega t) \tag{2.1.31}$$

From this potential, one can compute the horizontal velocity u and the vertical velocity w

$$u = -\frac{\partial \Phi}{\partial x} = \frac{H}{2}\sigma\frac{cosh(k(h+z))}{sinh(kh)} cos(kx - \omega t) \tag{2.1.32}$$

And,

$$w = -\frac{\partial \Phi}{\partial z} = \frac{H}{2}\sigma\frac{sinh(k(h+z))}{sinh(kh)} sin(kx - \omega t) \tag{2.1.33}$$

Pressure field under a progressive wave

The pressure field associated with a progressive wave is computed from the unsteady Bernoulli equation :

$$\frac{p}{\rho} + gz + \frac{u^2 + w^2}{2} - \frac{\partial \Phi}{\partial t} = C(t) \tag{2.1.34}$$

Where C(t) was shown to be equal to 0 earlier (see Equation 2.1.22). Replacing the potential velocity, and neglecting small velocity squared terms gives :

$$p = -\rho \cdot g \cdot z + \rho \cdot g \cdot \frac{H}{2}\frac{cosh(k(h+z))}{cosh(kh)} cos(kx - \omega t) \tag{2.1.35}$$

Or,

$$p = -\rho \cdot g \cdot z + \rho \cdot g \cdot \eta \cdot K_p(z) \tag{2.1.36}$$

Where,

$$K_p(z) = \frac{cosh(k(h+z))}{cosh(kh)} \tag{2.1.37}$$

The first term of Equation 2.1.36, $-\rho.g.z$, represents the hydrostatic pressure term, and the second one, $\rho.g.\eta.K_p(z)$, represents the dynamic pressure.

Energy and energy propagation in progressive waves

Wave energy has two components: a potential energy and a kinetic energy. The potential energy results from the displacement of water volumes while the kinetic energy results from the movement of the water particles.

To compute the potential energy (for 1 m width), we first compute the area of the displaced water (noted S in Figure 2.2) with $\eta = (H/2)cos(kx - \sigma t)$:

$$S = \int_{-L/4}^{L/4} \eta(x)dx = \frac{HL}{2\pi} \tag{2.1.38}$$

Then, we compute the distance between the centers of gravity (Z_g in Figure 2.2) of the water volumes initially in the through that was elevated by the action of the wave. Z_g is computed with the following expression :

$$Z_g = \frac{1}{S}\int_{-L/4}^{L/4} \eta(x)\eta(x)dx = \frac{H\pi}{16} \tag{2.1.39}$$

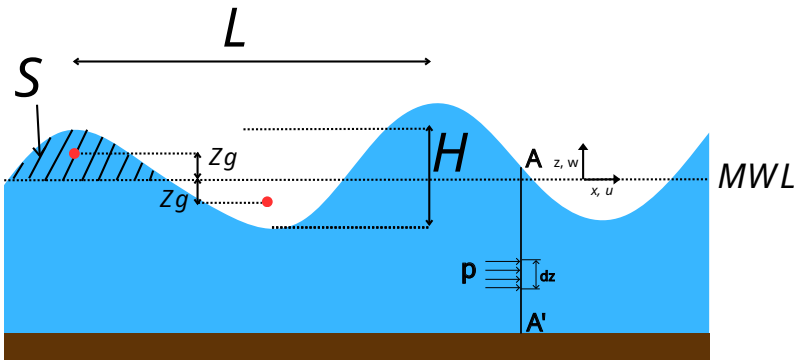

Figure 2.2: Definition sketch for determination of potential energy

Finally, the potential energy (PE) of the wave is :

$$PE = m \cdot g \cdot \Delta z \tag{2.1.40}$$

When replacing the corresponding values this becomes :

$$PE = \rho \cdot V \cdot g \cdot \Delta z = \rho \cdot g \cdot (S.1) \cdot (2 \cdot Z_g) = \rho \cdot g \cdot \frac{H^2 L}{16} \tag{2.1.41}$$

Averaging the Potential Energy over one wave length finally yields :

$$\overline{PE} = \rho \cdot g \cdot \frac{H^2}{16} \tag{2.1.42}$$

The kinetic energy (KE) is associated with a mass of fluid moving at a given velocity. We can define the kinetic energy of a small parcel of fluid moving at velocities u and w :

$$d(KE) = d \cdot m \cdot \frac{u^2 + w^2}{2} = \rho \cdot dx \cdot dz \cdot \frac{u^2 + w^2}{2} \tag{2.1.43}$$

To obtain the kinetic energy over one wave length, we integrate the previous equation over the water depth and a wave length then divide by the wave length :

$$\overline{KE} = \frac{1}{L} \int_x^{x+L} \int_{-h}^{\eta} \rho \cdot \frac{u^2 + w^2}{2} \cdot dz \cdot dx \tag{2.1.44}$$

Replacing, the known expression for the velocities u and v and carrying out the computation yields :

$$\overline{KE} = \frac{1}{16} \rho \cdot g \cdot H^2 \tag{2.1.45}$$

Finally, the total average energy per unit surface area (noted E) is :

$$E = \overline{PE} + \overline{KE} = \frac{1}{8} \rho \cdot g \cdot H^2 \tag{2.1.46}$$

Waves are able to transfer energy. The rate at which the energy is transferred is called the wave energy flux, and for linear theory it is the rate at which work is being done by the fluid on one side of a vertical section, on the fluid on the other side. At a location, the instantaneous energy flux of a slice A-A' (see Figure 2.2), is the work done by the dynamic pressure $p_d = \rho.g.\eta.K_p(z)$ in the direction of wave propagation :

$$P = \int_{-h}^{\eta} p_d \cdot u \cdot dz \tag{2.1.47}$$

The average wave energy flux is then obtained by averaging over a wave period :

$$\overline{P} = \frac{1}{T} \int_t^{t+T} \int_{-h}^{\eta} p_d \cdot u \cdot dz \tag{2.1.48}$$

After some computations the above equations is reduced to :

$$\overline{P} = \left(\frac{1}{8} \rho.g.H^2 \right) \frac{\sigma}{\omega} \left(\frac{1}{2} \left(1 + \frac{2kh}{sinh(2kh)} \right) \right) \tag{2.1.49}$$

Or, with $C = \frac{\sigma}{\omega}$

$$\overline{P} = E \cdot C \cdot n = E \cdot C_g \tag{2.1.50}$$

C_g is called the group velocity and is the velocity at which the energy propagates. It has to be noted that in deep water, where $sinh(2kh) \to \infty$, we have $C_g = \frac{C}{2}$, and in shallow waters, where $sinh(2kh) \to 2kh$ we have $C_g = C$.

2.1.2 Transformation of water waves entering shallow waters

When propagating towards shallow water, some properties (such as the wave height or the wave direction) of ocean waves change. From the beginning of this manuscript waves have been considered to only propagate in the x-direction, corresponding to the normal of the coastline. However, in reality waves have also propagates in the long-shore direction. For a wave propagating only in the x direction we have seen the following representation for the free surface elevation :

$$\eta(x,t) = \frac{H}{2} cos(kx - \omega t) = \frac{H}{2} cos(\Omega) \tag{2.1.51}$$

Modifying this equation to include propagation in y-direction gives :

$$\eta(x,t) = \frac{H}{2} cos(k_x \cdot x + k_y \cdot y - \omega t) \tag{2.1.52}$$

With, $k_x = |k| \cdot cos(theta)$ and $k_y = |k| \cdot sin(theta)$, the projection of the wave number k in the x-y space (see Figure 2.3).

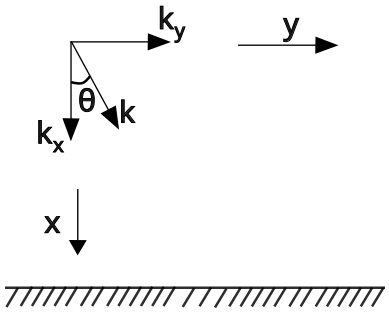

Figure 2.3: Projection of the wave number in x-y space

Here, the gradient operator ∇ is only the operator over the horizontal x and y variables. We then have :

$$k = \nabla\Omega \tag{2.1.53}$$

And,

$$\sigma = -\frac{\partial\Omega}{\partial t} \tag{2.1.54}$$

We can see that,

$$\frac{\partial}{\partial t}(\nabla\Omega) + \nabla(-\frac{\partial\Omega}{\partial t}) = 0 \tag{2.1.55}$$

And using Equations 2.1.53 and 2.1.54 we finally obtain :

$$\frac{\partial k}{\partial t} + \nabla\sigma = 0 \tag{2.1.56}$$

This equation states that any temporal variation of the wave number k induces a spatial variation of the pulsation σ. Therefore if a wave field is stationary, it means that the period T of the waves are homogeneous in space.

We saw earlier that $k = \nabla\Omega$. Therefore taking its curl yields :

$$\nabla \times k = 0 \tag{2.1.57}$$

Then, substituting the components of Ω in the x-y space gives :

$$\frac{\partial(k \cdot sin\theta)}{\partial x} - \frac{\partial(k2 \cdot cos\theta)}{\partial y} = 0 \tag{2.1.58}$$

This equation is called the refraction equation. It states that, variation in wave number, must be compensated by change in wave direction. If there are no variation along the y axis, the previous equation reduces to $\frac{d(ksin\theta)}{dx} = 0$ which leads to:

$$k \cdot sin\theta = constant \tag{2.1.59}$$

Or, if we divide by σ,

$$\frac{sin\theta}{C} = constant \tag{2.1.60}$$

Which is a form of Snell's law :

$$\frac{sin\theta_0}{C_0} = \frac{sin\theta_1}{C_1} \tag{2.1.61}$$

Snell's law indicates that for a wave approaching a coastline with straight and parallel contours, since its velocity decreases, its wave direction θ also decreases tending to approach the shore normally.

Wave shoaling consists in the increase of wave height when approaching the shore. This process is induced by the conservation of wave energy. Wave rays are the lines perpendicular to the wave crests, along which the wave energy propagates (see figure 2.4). Here, we will consider no energy losses or inputs across the wave rays (i.e. the wave energy flux across b_0 is the same as across b_1 and b_2). However, due to the convergence or divergence of wave rays, the wave energy integrated along b_0 might be different than the one across b_1 or b_2. Therefore the conservation of the energy integrated along b_0 and b_1, as computed in equation 2.1.50, requires that :

$$(E_0 \cdot C_{g0}) \cdot b_0 = (E_1 \cdot C_{g1}) \cdot b_1 \tag{2.1.62}$$

Using the expression for the wave energy E at each location yields :

$$H_1 = H_0 \sqrt{\frac{C_{g0}}{C_{g1}}} \cdot \sqrt{\frac{b_1}{b_2}} = H_0 \cdot K_S \cdot K_r \tag{2.1.63}$$

Where K_S is the shoaling coefficient and K_r the refraction coefficient.

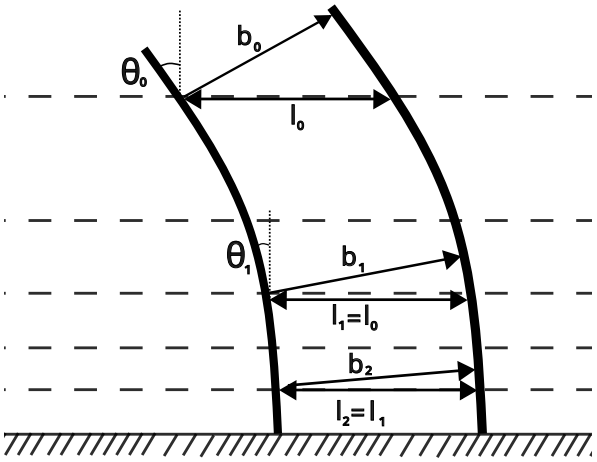

Figure 2.4: Characteristics of wave rays during refraction over idealized bathymetry

2.1.3 Irregular waves

Real sea states are always composed of a superposition of frequencies. Therefore, to be able to properly model the complexity of the waves, additional statistical and probabilistic tools are required.

Wave by wave analysis

The wave by wave analysis consists of measuring the water level elevation at a given point for a given period of time. A wave is defined as the difference between crest to through between two consecutive positions where $\eta = 0$. The waves are then ordered from the largest to the smallest, from 1 to N. Then, it is possible to classify the sea states with various quantities such as H_{max}, the maximum wave height, $H_{1/3}$, the average of the highest third of all waves (also called significant wave height H_S) or, H_1 the mean wave height. We can also define the probability that the wave height is higher than an arbitrary height $\hat{\mathrm{H}}$ as

$$P(H > \hat{\mathrm{H}}) = \frac{n}{N} \tag{2.1.64}$$

Here we assume that the sea state is composed of M wave trains with pulsation close to a central pulsation ω.

$$\eta(t) = \sum_{m=1}^{M} \frac{H_m}{2} cos(\omega_m t - \epsilon_m) \tag{2.1.65}$$

Which expression in complex notation gives : $\eta(t) = Re\left(\sum_{m=1}^{M} \frac{H_m}{2} e^{i(\omega_m t - \epsilon_m)}\right)$ Factoring out the carrier frequency ω we obtain,

$$\eta(t) = Re\left(e^{i\omega t} \sum_{m=1}^{M} \frac{H_m}{2} e^{i((\omega_m - \omega)t - \epsilon_m)}\right) \tag{2.1.66}$$

To study the wave height distribution we focus only on the slowly varying envelope :

$$\sum_{m=1}^{M} \frac{H_m}{2} e^{i((\omega_m - \omega)t - \epsilon_m)} \tag{2.1.67}$$

It has been shown by [Longuet-Higgins and Stewart 1962] that if the components of the previous equation are statistically independent and a large number of waves is studied, the probability of a single wave height H being equal or higher than an arbitrary wave height $\hat{\mathrm{H}}$ is given by :

$$P(H \geq \hat{\mathrm{H}})) = e^{-\left(\frac{\hat{\mathrm{H}}}{H_{rms}}\right)} \tag{2.1.68}$$

And since $P(H \geq \hat{\mathrm{H}})) = \frac{n}{N}$ we have :

$$\frac{n}{N} = e^{-\left(\frac{\hat{\mathrm{H}}}{H_{rms}}\right)} \tag{2.1.69}$$

Which leads to :

$$\hat{\mathrm{H}} = H_{rms}\sqrt{ln(\frac{1}{p})} \tag{2.1.70}$$

From the previous equation it is possible to derive the probability density function f_H

$$f_H = \frac{d}{dH}\left(P(H < \hat{\mathrm{H}})\right) = \frac{d}{dH}\left(1 - e^{-(\frac{\hat{\mathrm{H}}}{H_{rms}})^2}\right) = 2\frac{\hat{\mathrm{H}}}{H_{rms}^2} e^{-(\frac{\hat{\mathrm{H}}}{H_{rms}})^2} \tag{2.1.71}$$

Then we can write,

$$P(a < H < b) = \int_a^b f_H(H)dH \tag{2.1.72}$$

This probability density function corresponds to the Rayleigh distribution shown in Figure 2.5 .

Then to compute the mean value of the pN highest waves we write:

$$\overline{H}_{H>H_p} = \frac{\int_{H_p}^{\infty} H f_H(H)dH}{\int_{H_p}^{\infty} f_H(H)dH} \text{ with, } H_p = H_{rms}\sqrt{ln(\frac{1}{p})} \tag{2.1.73}$$

Spectral analysis

The wave-by-wave analysis done in the time domain does not allow the full analysis of complex waves that occur in the ocean. Indeed, analysis carried out in the time-domain provides insights into the temporal characteristics of a signal, such as amplitude and duration, but it lacks the ability to reveal the frequency content and variations within the signal. Therefore analysis of the ocean waves are usually carried out through the computation of variance density spectrum of the wave elevation, called $E'(f)$. This continuous function is obtained by deriving the Fourier transform of the auto-covariance function $C(\tau)$:

$$E'(f) = \int_{-\infty}^{\infty} C(\tau)e^{-2\pi i f \tau} d\tau \tag{2.1.74}$$

The auto-covariance function is $C(\tau) =< \eta(t)\eta(t+\tau) >$ and represents the covariance of the sea

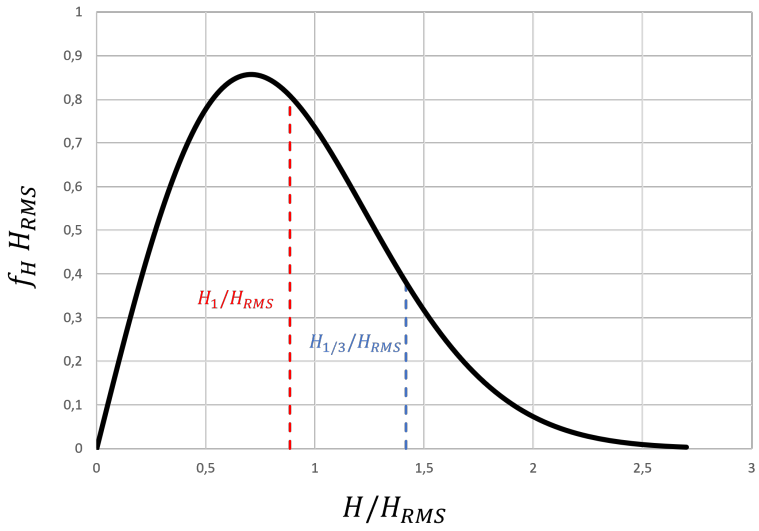

Figure 2.5: Rayleigh distribution probability function

surface elevation with a time lag τ. For stationary wave conditions, we consider the following $E(f)$ spectrum :

$$E(f) = 2E'(f) \text{ with f}\geq 0 \text{ and E(f)=0 for } f < 0 \tag{2.1.75}$$

The variance of the sea surface elevation is distributed along all the frequency components of the sea state and therefore can be read as a variance density. This variance is given by the following expression :

$$< \eta^2 >= C(0) = \int_0^{+\infty} E(f)df \tag{2.1.76}$$

This variance $< \eta^2 >$ can be related to the energy E_{tot} of the waves per unit surface with :

$$E_{tot} = \frac{1}{2}\rho g < \eta^2 > \tag{2.1.77}$$

Wave energy is not only distributed along frequencies but also along the different propagation directions. Similarly, we then have :

$$< \eta^2 >= \int_0^{+\infty} \int_0^{2\pi} E(f,\theta)df\,d\theta \tag{2.1.78}$$

Based on the energy density spectrum, the n-th spectral moments are built following this expression :

$$m_n = \int_0^{+\infty} f^n E(f)df \tag{2.1.79}$$

These spectral moments allow to compute the statistical parameters used to characterize a sea state :

$$H_s = 4\sqrt{m_0} \tag{2.1.80}$$

$$T_{m01} = \frac{m_0}{m_{-1}} \tag{2.1.81}$$

2.2 Computing ocean waves

The spectral modelization presented above allows us to represent and analyze the ocean. Computational models are then used to propagate the ocean waves (i.e. the wave spectras) from the generation zone to the coast. Various wave propagation models are used depending on the extent of the domain studied. In this PhD, the SWAN (Simulating WAves Nearshore) model developped by [Booij, Ris, and L. H. Holthuijsen 1999] has been used.

2.2.1 Model: SWAN

SWAN is a third-generation wave model. It means that all involved physical processes are modelled explicitly, without imposing spectral shapes or energy levels. SWAN includes the formulation from the WAM model [Komen, Cavaleri, and Donelan 1996] for deep water and adds new formulations for nearshore processes such as bottom friction or depth-induced breaking.
Instead of the energy density spectrum presented above, wave models use the action density spectra, noted N, due to its conservative nature even in the presence of current [Whitham 1974]. The action density is defined by the following equation :

$$N = \frac{E}{\omega} \tag{2.2.1}$$

The main equation solved by the wave model SWAN is the so-called action balance equation [Hasselmann et al. 1973].

$$\frac{\partial N}{\partial t} + \nabla \overrightarrow{x} . ((\overrightarrow{c_g} + \overrightarrow{u})N) + \frac{\partial c_\omega N}{\partial \omega} + \frac{\partial c_\theta N}{\partial \theta} = \frac{S_{tot}}{\omega} \tag{2.2.2}$$

The left side of the equation represent the kinematic part of the equation, while the right side represents the sink and source term of wave action density. The $\nabla \overrightarrow{x} . ((\overrightarrow{c_g} + \overrightarrow{u})N)$ term represents the advection of action density spectra in geographical space while the $\frac{\partial c_\omega N}{\partial \omega}$ and $\frac{\partial c_\theta N}{\partial \theta}$ represents the advection of action density spectra in spectral space.
The right side of the equation represents the source and sink terms of the wave action density. The S_{tot} term is decomposed into a several sub-terms as detailed in the following expression :

$$S_{tot} = S_{in} + S_{nl4} + S_{ds} + S_{nl3} + S_{db} + S_{bot} \tag{2.2.3}$$

The first three term dominate in deep water while the three others dominate in shallow water [L. Holthuijsen 2007],

- S_{in} : interactions with atmosphere, especially generation by wind
- S_{nl4} : non-linear interactions between quadruplets of wave
- S_{ds} : energy dissipation by whitecapping
- S_{nl3} : non-linear interactions between triplets of waves
- S_{db} : depth induced breaking
- S_{bot} : dissipation by bottom friction

The equation is solved by means of finite difference schemes.

Chapter 3

Literature review

Finding n optimal location for a wave energy converter as explained in Chapter 1 is an extremely complex multi-criteria process. It can involve several fields of studies (e.g. physics, biology, socioeconomics...). The work carried out during this PhD intends to pave the road for further studies that may include other aspect than physics.

At the beginning of any WEC installation project understanding the full harvesting process of the wave energy is obviously a key aspect. Wave energy assessment, as a first step towards having an idea of the distribution of the wave energy over a studied domain is a critical step since it may give an essential information on the feasibility of the project. Many studies have focused on the spatio-temporal variability at various scales using validated numerical models. A quick summary of these studies will be presented in this manuscript. Once the variability of the resource is better understood, it is essential to focus on the technology that will be used to harvest this energy. A large number of prototypes have been and are still being developed. The properties and specifics of some WECs are also presented and discussed in this chapter.

However, placing such complex devices in the open ocean is far from trivial. Harvesting the wave energy means that the more energy there is, the better. But a higher amount of energy also means that the devices placed in the ocean will endure harsher conditions. It appears then necessary not only to assess the amount of energy available but also the magnitude of the loads that the WECs will receive during their operational lifetime. The survivability of the WECs is then as important as the resource. An analysis of the failure of some WEC will be carried out in order to identify the main hazard for these structures and a review regarding the computations of the loads will therefore be carried out.

To choose the optimal location of the WECs, the aforementioned information (i.e. the wave energy resource and the loads) need to be analyzed. A review of methodologies available to combine geographical datasets will finally be undertaken.

3.1 Harvesting the wave energy

3.1.1 Resource assessment

As underlined earlier, the first mandatory step in the deployment of WECs, is the assessment of the available resource. Since for most of the devices, the energy produced is the only output, it

is essential to know its spatio-temporal variability. This is why several studies have focused on this subject. Those studies are usually carried out the same way. Focusing on nearshore domains, the output of coarser numerical models are used as input data for specific nearshore wave propagation models such as SWAN, WAM or MIKE21. The models are then run over periods ranging from a few years to a few decades. These simulations are all validated with measurements to ensure that the outputs of the numerical simulations are representative of the reality. Then, the outputs are analyzed and the reasons of the variability are detailed. A summary of the wave energy assessment studies done in the south-west part of Europe (Figure 3.1) is presented in Table 3.1.

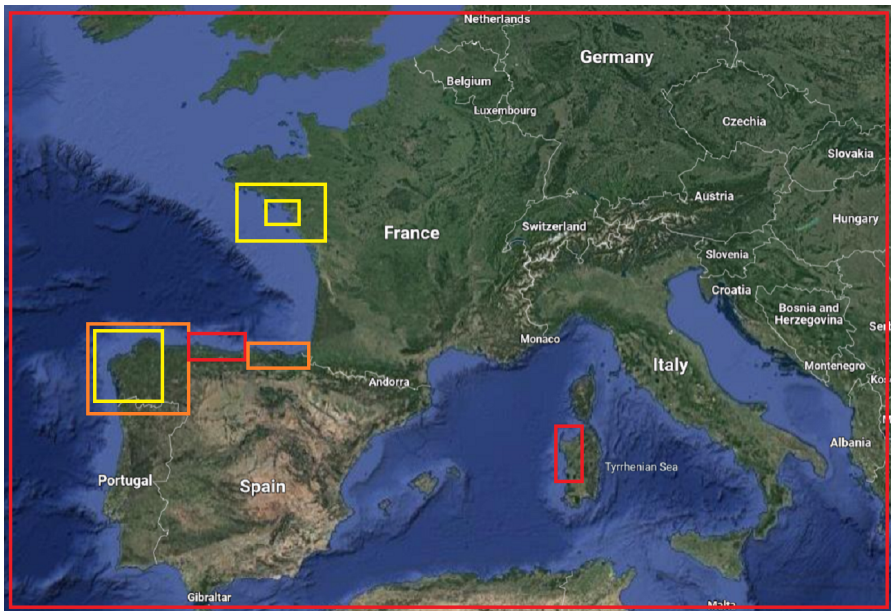

Figure 3.1: Localization of previous wave energy assessment studies

These studies have shown that wave energy has a lot of variability both in time and in space. Levels of mean wave energy fluxes range between 5 and 35 kW/m. Some very localized wave energy hotspots are also identified showing the importance of having an adequate spatial resolution.

Local wave energy assessment are complemented by studies analyzing long term trends and the consequences for WECs [Ulazia et al. 2017] or specific links with larger climatic trends [Reguero, Losada, and Méndez 2015] such as the North Atlantic Oscillation for example. The North Atlantic Oscillation (NAO) is a climatic phenomenon characterized by the variation in atmospheric pressure between the Icelandic Low and the Azores High over the North Atlantic Ocean ([Visbeck et al.]). It exerts significant influence on weather patterns and climate variability in the North Atlantic region, affecting temperature, precipitation, and storm tracks.

3.1.2 Example of Wave Energy Converters

In the recent years, a large variety of WEC have been developed, taking advantage of various technologies. In this section of the manuscript, some of the techniques are briefly presented. The

Researcher (date)	Location	Model used	Spatial discretization	Period studied
Iglesias and al., (2009)	N-W Spain (Galicia)	SWAN	$\Delta x = 350m \Delta y = 200\text{-}820m$	1958-2001
Iglesias and Carballo (2009)	Northern Spain (Death coast)	SWAN	$\Delta x = \Delta y = 1$ km	1958-2001
Iglesias and Carballo (2010)	Northern Spain (Asturias)	SWAN	$\Delta x = 350m \Delta y = 200\text{-}820m$	1958-2001
Iglesias and Carballo (2010)	N-E Spain (Bay of Biscay)	SWAN	$\Delta x = 400m \Delta y = 333m\text{-}1km$	1958-2001
Vicinanza and al., (2013)	Italy (Sardinia)	MIKE 21	$\Delta x = \Delta y = 100m$	1989-2009
Gonçalves and al. (2014)	Western France (Britany)	SWAN	$\Delta x = 3km \Delta y = 6km$ $\Delta x = 400m \Delta y = 400m$	1998-2000

Table 3.1: Summary of wave energy assessment carried out in Europe

following non-exhaustive list is based on a benchmark study done by [Babarit et al. 2012], to avoid presenting commercial devices. Since the study does not rely on existing prototypes, the dimensions and output powers mentioned hereafter may differ from reality. The operation processes of the devices, such as detailed description of the Power-Take-Off (device that transfers a mechanical power to another piece of equipment), will not be detailed here.

Bottom-referenced heaving buoy

This device consists in a buoy of around 3 m floating at the sea water level and anchored to the sea bottom (see Figure 3.5). The heave and surge motions of the buoy, driven by the waves, induces motion of a linear generator. This kind of device is well suited for water depth between 40 and 100m and can reach annual mean absorbed power values between 1 and 5 kW (an instantaneous power of 5 kW is for example reached for $H_s = 4m$ and $T_p = 12s$). Another similar technology consists in a bottom referenced buoy that is submerged instead of floating at the surface.

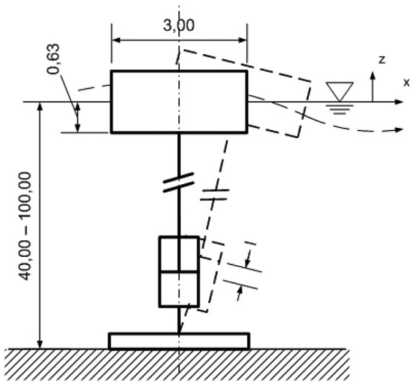

Figure 3.2: Sketch of a small bottom-referenced heaving buoy

Floating two-body heaving buoy

This WEC technology consists in two body of different drafts sliding along one another. The first body is a torus of around 20m diameter and around 2m draft while the second one is a float of a approximately 50m. The relative motion between the two bodies drives the Power-Take-Off system off around 100-400 kW (an instantaneous power of 400 kW is for example reached for $H_s = 4m$ and $T_p = 13s$). Given the size of the device, this kind of WEC should only be considered for deep waters.

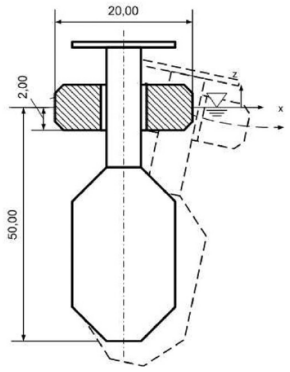

Figure 3.3: Sketch of a floating two-body heaving buoy

Bottom-fixed heaving buoy array

This technology is composed of several floats connected to a structure. This structure can be a jack-up structure fixed in seabed, or an existing onshore structure like a jetty. The heave motion of the floats, connected to the structure via an arm, is converted into hydraulic energy through rams. This energy is in turn converted into electricity. An array composed of 20 floats of 5m diameter has a mean absorbed power of around 100 to 600 kW (an instantaneous power of 600 kW is for example reached for $H_s = 3.5m$ and $T_p = 13s$).

Bottom-fixed oscillating flap

This kind of WEC consists of a pitching flap fixed to the sea bottom. A pump placed at the rotating shafts pumps pressurised oil to an onshore station. This devices are well suited for the nearshore area since a connection to the land is necessary. A single device composed of a 26m wide flap has an approximate absorbed power of 200 to 900 kW (an instantaneous power of 900 kW is for example reached for $H_s = 3m$ and $T_p = 10s$).

Oscillating water column

This technology is the one that differs the most from the other technologies presented above since it is not directly the wave motion that is converted into energy. Here, the device encloses a water column, then the motion of the latter relative to the device creates a pressure variation which in turn drives air through an air-turbine. This technology can either be used onshore (e.g.

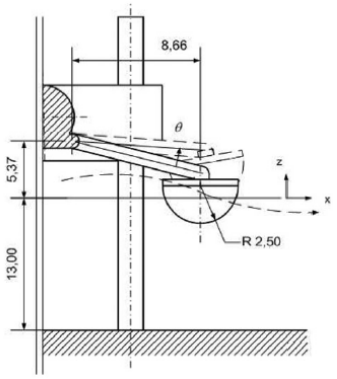

Figure 3.4: Sketch of a bottom-fixed heaving buoy array

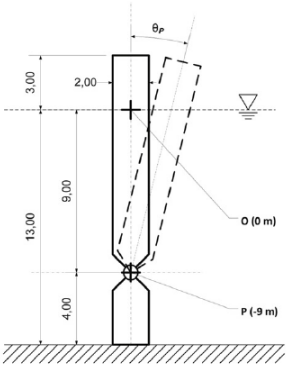

Figure 3.5: Sketch of a small bottom-referenced heaving buoy

coupled with breakwaters) or offshore (e.g. floating devices). The mean absorbed power ranges from 100 kW to 700 kW (an instantaneous power of 700 kW is for example reached for $H_s = 4m$ and $T_p = 13s$).

3.2 Survivability of a WEC

WEC are quite complex devices that are placed in a harsh environment. Given their expected lifetime of few decades ([DNV 2010]), events that may affect their survivability are likely to occur. Anticipating these events is key to ensure the durability of any wave energy conversion project. Several risks should be accounted for WEC survivability analysis. Among them, mechanical failures include risks associated with corrosion, fatigue and failure of moving pieces such as bearing or gears. Also, since the WECs are high-technology equipment, electrical components and control system are required for its proper functioning. This components may suffer problems that could lead to the malfunctioning of the WEC. Finally, wave motion, which is ironically the resource of any WEC, is also one of the biggest challenge to overcome with respect to survivability.

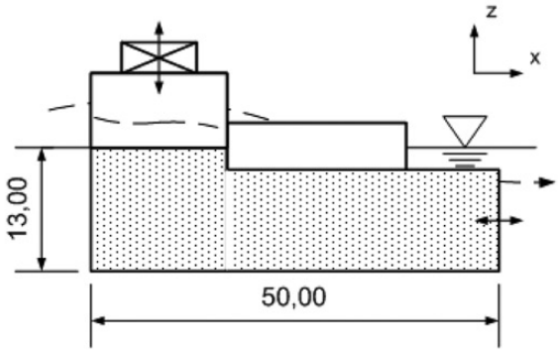

Figure 3.6: Sketch of a small bottom-referenced heaving buoy

Figure 3.7: (Left) Picture of the WEC of Mutriku after the storm (Right) Picture of a damaged chamber of the WEC

3.2.1 Failure of some WECs

As stated above, WECs are subject to harsh conditions and lots of them have suffered failures. The exacts reasons of the failures are not always known. Some studies have tried to make conjectures beforehand. Studying a floating object, numerical and experimental studies by [Elhanafi et al. 2017] have shown that, it was not necessarily the highest wave in an irregular wave train that caused the largest force in the mooring lines but rather an adverse combination of waves with positions of the device. Other numerical studies (e.g. [Bucchi and Hearn 2016]) have shown the interest of using structural Finite Element Modelling to compute stresses inside WEC structures.

In other cases, a post-failure analysis was carried out. In the case of the OWC device installed in Mutriku (Spain), a numerical analysis was carried out by [Medina-Lopez et al. 2017], after a winter storm in 2009 partially damaged the WEC. The study suggests that even operational wave conditions may have exceeded the resistance of the structure. The 2009's storm may have caused pressure 6 times higher than the maximal resistance, leading to the damages visible in Figure 3.7.

3.3 WEC localization

As already mentioned before, the available energy is not the only factor when deciding the location of a wave energy farm. The failure risks have been discussed previously but other aspects should be taken into account. Economical aspects are always to be considered in choosing location. For instance, depending on the WEC technology used, a link between the installation cost and the distance to the shore is clear. Therefore nearshore location could be more interesting from this point of view. However, other economical activities such as sea transport or fisheries should also be taken into account. Therefore, when deciding of the localization of a WEC project, a list of all the parameters influencing the final decision should be made.

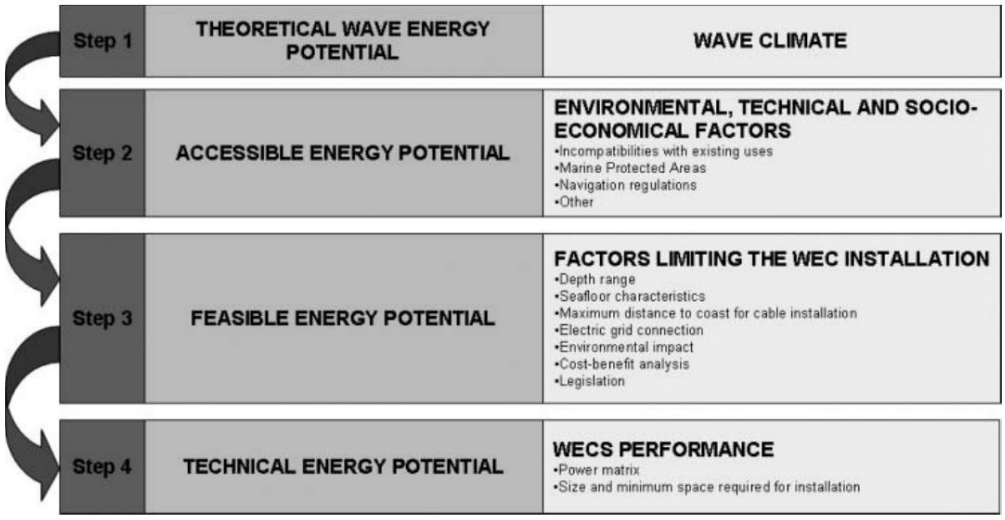

Figure 3.8: 4 step procedure for the choice of localization of a WEC presented in [Galparsoro et al. 2012]

These parameters should not be computed at some specific locations but rather computed over large geographical domains. A methodology towards a marine spatial planning including 17 layers of information was proposed by [Galparsoro et al. 2012]. This study proposed the creation of various sub-indexes allowing to reach to a final Suitability Index which defines the best locations for a WEC. It is the impression of the author of this manuscript that although this methodology appears to be very promising, the tuning of the sub-indexes require complex decision making and that a wrong tuning could lead to misrepresent the importance of a given parameter. Additionally, the hazard that the WEC will face through their operational lifetime is not taken into consideration in the process.

3.4 Problematic of the PhD

Regarding the current state of the art presented in this chapter, it appears necessary to complement certain aspects of this field. When addressing the wave energy resource harvesting, two aspects should be focused on : the variability of the resource and the harvesting of the resource. On the one hand, the nearshore wave energy resource was shown to vary a lot between close locations but also in time. Therefore, a first challenge that arises is the description of the nearshore variability of wave energy resource over long periods. Once this variability is better described, understanding the reasons behind it is also of major interest.

However, the available wave energy resource is not how the performance of a WEC is evaluated. The performance of a WEC is based on the produced amount of electrical energy. Therefore, the actual energy produced should also be considered and a comparison of the computation methods would be highly beneficial. Being able to convert accurately a given available resource to an electrical energy is key to assess the interest of a location from a production point of view.

Even if a location has strong potential production wise, it does not necessarily mean that is the optimal location for WEC. In this chapter, the role of impact loads on the structural integrity of WECs was highlighted. The structural designs of WEC could be improved if the magnitude of the impact loads over the lifetime of the WEC were known. Alternatively, studying the spatial distribution of this loads could allow to choose a relatively sheltered location for the WEC.

In the light of this chapter, the choice of a localization for a WEC requires a compromise between high wave energy resource and low hazard for the device. Therefore, a cross-analysis must be carried out in order to understand whether or not there is correlation between these two aspects. These results are expected to provide policymakers guidelines and additional resources to improve localization of WECs.

Chapter 4

Wave Energy Assessment in the South Aquitaine Nearshore Zone from a 44-Year Hindcast

Note : This chapter is an article published in the Journal Of Marine and Science Engineering [Lastiri et al. 2020]

Wave resource assessment is the first step toward the installation of a wave energy converter (WEC). To support initiatives for wave energy development in the southwest of France, a coastal wave database is built from a 44 year hindcast simulation with the spectral wave model SWAN (Simulating WAve Nearshore) run on a high resolution unstructured grid. The simulation includes shallow-water processes such as refraction, shoaling, and breaking. The model is validated against a five year coastal wave buoy recording. The study shows that most of the resource is provided by sea states with wave heights ranging from 2 to 5 m, with wave periods from 10 and 15 s, and coming from a very narrow angular sector. The long hindcast duration and the refined unstructured grid used for the simulation allow assessment of the spatio-temporal distribution of wave energy across the coastal area. On the one hand, large longshore variations of the resource caused by steep bathymetric gradients such as the Capbreton submarine canyon are underlined. On the other hand, the study highlights that no specific long term trend can be extracted regarding the coastal wave energy resource evolution. The provided down-scaled local wave resource information may be used to optimize the location and design of a future WEC that could be deployed in the region.

4.1 Introduction

To meet the objectives that policymakers set regarding the reduction of human carbon footprint, the development of new energy sources is mandatory. Wave energy conversion is considered as one of the possible marine renewable energy contributions to a sustainable energy mix in the future. France has a very long coastline of about 2400 km, which was shown to offer a significant wave energy resource [Boudière et al. 2013]. The wave energy resource is quite well distributed along the shoreline as opposed to, e.g., tidal energy where only a few hotspots are suitable for installation.

Additionally, available wave energy during the year is usually the highest when the energy demand is also high, i.e., in winter. The first step toward wave energy exploitation is the assessment of the wave energy resource on site. Wave resources were already quite well studied at a regional scale for the northern part of Spain, from Galicia to Basque Country ([Iglesias and Carballo 2009]; [Iglesias and Carballo 2010]; [Iglesias, López, et al. 2009]) , as well as locally along the western coast of France, e.g., in Le Croisic area [Gonçalves, Martinho, and Guedes Soares 2014]. When assessing the available resource, its space–time variability is a key parameter. This variability may be especially strong in the coastal area due to wave–bottom interactions, which may induce large variations in the wave field both in space and in time. Space variability is obviously interesting for the installation of a wave energy converter (referred to as WEC in the rest of this paper) as it is of the utmost importance to determine an optimal WEC location [Vicinanza, Contestabile, and Ferrante 2013]. The time variability is also crucial to properly anticipate the energy effectively available throughout the year, as major seasonal differences may be observed in some regions [Sierra et al. 2017]. Finally, the extreme sea states and long term variability of the wave climate should also be addressed to ensure that the sizing of the WEC is compatible with survivability in both current and future conditions [Ulazia et al. 2017]. The objective of the present study is to provide an assessment of the local wave energy resource distribution along the south Aquitaine coastal area, a region that was identified as potentially suitable for WEC deployment by previous studies [Dufour et al. 2013]. To that end, a numerical modeling strategy is deployed using a fine computational domain based on an unstructured mesh to capture the different processes affecting the wave field over the shelf, especially the effect of a remarkable topographic feature: the Capbreton submarine canyon. The 44 year duration of the obtained high resolution database is also used to analyze long term trends of the local wave resource. The paper is organized as follows: Section 2 describes the data used, the parameterization of the model, and its validation. The analysis of the obtained results is detailed in Section 3. Those results are discussed in Section 4, and conclusions are drawn in Section 5.

4.2 Materials and Methods

4.2.1 Offshore Wave Data

The present study relies on a new wave hindcast dataset produced with a spectral wave model to provide a refined long term database of coastal sea states in the studied region. The data used to prescribe offshore boundary conditions in our wave hindcast simulation were from the so called BOBWA (Bay Of Biscay Wave Atlas) dataset covering 44 years (i.e., from 1958 to 2001). The BOBWA database was constructed from a hindcast simulation with a North Atlantic wave modeling system based on the WAVEWATCH III® code and forced by 40 year European Center for Medium Range Weather Forecasts Re Analysis (ERA 40) wind fields, providing refined spatial resolution (0.5° for water depth superior to 4000 m and 0.1° elsewhere) over the Bay of Biscay [Charles et al. 2012]. The validation of the wave model was based on 10 buoys moored at different locations across the Bay of Biscay, at depths ranging from -17 m to -54 m. One deep water buoy was also used (water depth -4500 m). The computed wave fields were then used in the analysis of mean and extreme wave height trends and variability. The BOBWA dataset provides hourly wave spectra at several points along the south Aquitaine coastal area studied in this paper, from Hendaye at the Spanish border up to Contis approximately 80 km north. In order to use this incident wave information properly, the offshore limit of our computational domain was adjusted

to the most onshore BOBWA output points as illustrated in Figure 4.1. The offshore boundary of our coastal model included 10 of these points, thus allowing for a spatially varying boundary condition. As the next BOBWA output points are located much farther offshore, an alternative (more offshore) delimitation of our computational domain would require significantly increasing the model complexity by taking into account additional forcing such as wave generation by wind among others; at the same time, it would require lowering model resolution to limit computation time. Considering this, the preferred compromise here was to focus on the coastal area and the related specific processes.

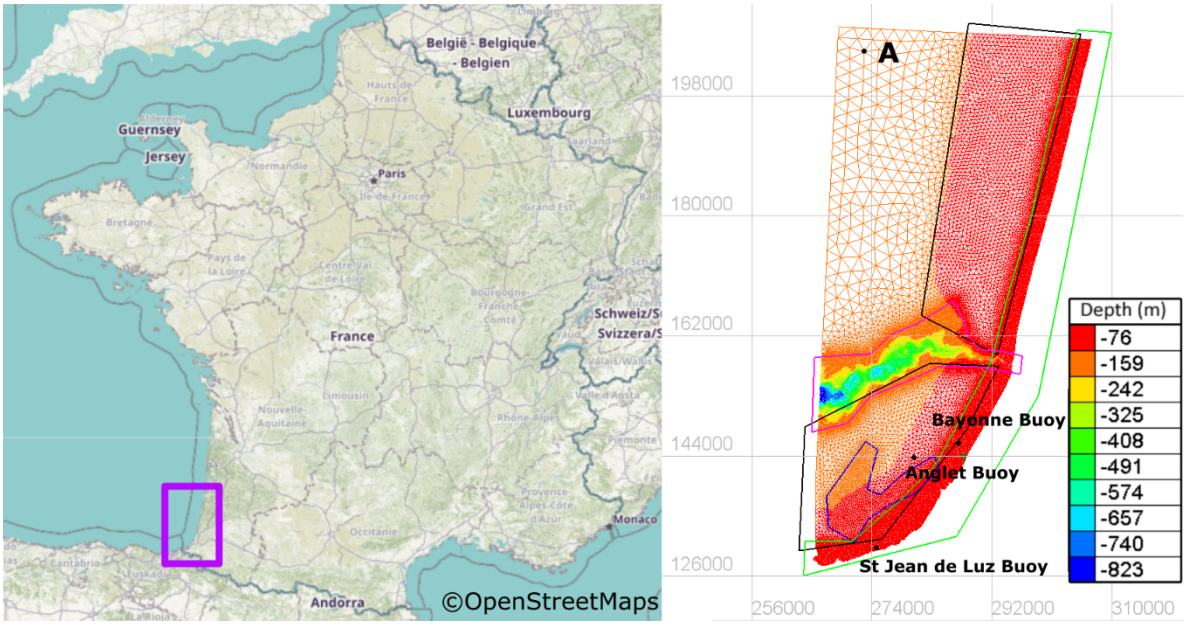

Figure 4.1: Unstructured mesh used in the present study, with bathymetry given by the color scale. Superimposed polygons indicate areas with different spatial resolution.

4.2.2 Validation Data

Measurements from a non directional wave buoy moored off Bayonne port in 20 m depth were used for validation. The wave buoy provided almost 8000 wave observations from 1989 to 1994 (approximately evenly distributed). These data were used to verify the validity of our model set-up, especially its ability to properly represent wave propagation in limited water depth up to the inner shelf.

4.2.3 Computationnal Grid

The model used here was built with the code SWAN in its unstructured version ([Booij, Ris, and L. H. Holthuijsen 1999]; [Dietrich et al. 2012]). SWAN (Simulating WAve Nearshore) is a state of the art third-generation wave propagation model dedicated to the study of coastal and

nearshore regions. It is based on solving the conservation of the wave action density by means of a finite difference scheme. The numerical scheme used was the so called cyclic scheme of Stelling and Leendertse, which reverts to BSBT (backward space/backward time) in the neighboring of open boundaries, land boundaries, and obstacles. To solve local bathymetric features that may affect the wave field during coastal propagation, an optimized unstructured mesh was used for the computation. Figure 4.1 shows the mesh implemented on the study area with the bathymetry indicated by the color scale. In this figure, the Capbreton submarine canyon is the most obvious feature in terms of depth variation, cutting the studied domain in two with a roughly east–west orientation. The canyon is characterized by strong bathymetric gradients, with depth dropping from about 100 m up to 800 m in the middle of the shelf. The coast is composed of sandy beaches north of Bayonne (Figure 4.1) usually associated with little bathymetric variations in the longshore direction, while rocky coasts are found down in the south where the bathymetry is more heterogeneous in both longshore and cross shore directions. The bathymetry was assumed to be constant over the hindcast period. The bathymetry initial dataset was composed of several inputs unevenly resolved, provided by different surveys including SHOM (French Naval Hydrographic and Oceanographic Service) data and several additional surveys with locally higher resolutions. The unstructured mesh featured 45,000 nodes distributed irregularly in space according to the different areas presented in Figure 4.1). These areas were determined by inspecting the depth gradient; the domain was divided into several areas based on averaged depth gradient characteristics and then using specific adapted constant mesh values in each area. More precisely, north of the canyon, the grid step was set to 150 m from the shore to -20 m depth, 600 m from -20 m to 80 m, and 2000 m beyond. South of the canyon, the grid step was 150 m from shore to -40 m, 300 m in the blue area depicted in Figure 4.1 where the bathymetry has quite sharp variations, and 600 m beyond. Over the canyon, the grid step was set to 100 m to solve locally very strong bathymetric gradients. Finally, this mesh allowed resolving the main bathymetry features while keeping the computational time within reasonable limits and avoiding convergence problems sometimes met with high-energy events.

4.2.4 Parameterization

The model was run in non stationary mode at mean tide water level (i.e., +2.25 m compared to depth shown in Figure 4.1). The contribution of wave generation by wind was assessed when building the model, confirming that the computational domain was small enough to neglect local generation (not shown here). Additional tests also confirmed that triad interactions had little effect on model results off a very shallow areas near the breaking zone, which were not targeted in this study. However, depth induced breaking was considered, using the bore based model of [J. Battjes and Janssen 1978] extended by [Eldeberky and J. Battjes 1995]. However, given that the surf zone was not properly resolved by the 100-m grid resolution in the coastal area, here, the depth related sink term was essentially used to avoid non realistic wave heights onshore. The resolved angular sector was limited from 240° to 0° (0° meaning waves coming from the north) to spare central processing unit (CPU) time. Therefore, waves propagating from other directions were neglected. This sector was chosen by analyzing measured wave data collected 6 km off Biarritz [Abadie et al. 2006], which confirmed that other angular sectors' contributions were negligible (not shown). The resolved angular sector was meshed with 40 bins, thus providing a directional resolution of 3°. The simulated frequency range extended from 0.0373 Hz to 0.25 Hz and was discretized with 20 frequencies distributed such that $\delta f = 0.1f$. Stationary case tests conducted with refined spectral discretization

showed no noticeable difference with the above mentioned frequency–direction discretization, suggesting that it was fine enough to properly solve the main processes involved in the studied coastal wave propagation. The computational time step used was 15 min while the output time step was set to 3 h. The maximum number of iterations in the SWAN internal sweeping procedure was 50.

4.2.5 Validation

The left panel of Figure 4.2 provides a scatter plot comparing simulated significant wave heights (H_s) and the five year record of the Bayonne wave buoy (at 20 m depth). For this sample, the simulation tended to slightly overestimate the significant wave height between 0 and 3 m. However, the coefficient of determination computed (0.87) showed a strong correlation between measured and simulated data. Both the normalized bias indicator (noted NBI) and the symmetrically normalized root-mean-square error introduced by Hanna and Heinold in 1985 (noted HH) [Hanna and Heinold 1985]; [Mentaschi et al. 2013] were low (0.09 for NBI and 0.20 for HH). This confirmed that wave height was reasonably well simulated in our hindcast at the buoy location. The scatter plot in the right panel of Figure 4.2 represents the simulated energy period Te versus the energy period obtained from measurements. From this illustration, the model seemed to overestimate the energy period. Even if the coefficient of determination was lower than for H_s (0.72), the model fairly estimated the energy period between 10 and 14 s (i.e., where the density of point was the highest). The bias indicator NBI was 0.12. The error HH was, however, higher compared to the H_s (0.27). This is rather consistent with [Cahill and Lewis], who already highlighted that the wave period is a parameter harder to estimate compared to the wave height. Simulated energy flux was calculated by integrating energy flux density over frequency and directional spaces, i.e., $P_w = \frac{\rho g}{1000} \int_0^{2\pi} \int_0^{\infty} C_g(f,D) E_{f,th}(f,\theta) df d\theta$. The measured energy flux was approximated by the following expression based on spectral bulk variables: $P_w = (\rho g^2 H_{m0}^2 T_e)/64\pi$, where $T_e = Tm{-}1;0$ is the energetic period. This formulation corresponds to a deep-water configuration, which may not be very accurate in the buoy location, but which had to be used due to the lack of detailed spectral information in the field data. This may have contributed to the obtained simulation/measurements energy flux differences. Moreover, the energy flux discrepancies (HH value of 0.39) were more important than for H_s because P_w depends on the square of the wave height; thus, the error in H_s was also squared when considering the error in P_w.

4.3 Results

4.3.1 Spatial Distribution of the Coastal Wave Energy Resource

The new hindcast simulation performed in this study provides a refined description of wave power spatial distribution across the south Aquitaine shelf. This detailed information is of great interest for WEC future development. Figure 4.3 shows the spatial distribution of the mean wave power in the studied domain, obtained from the average over the 44 years of the hindcast simulation. This plot reveals a remarkable difference in the wave energy resource between the north ($y > 160,000$ m) of the domain and the southern part, with significantly higher energy in the north. The delimitation between both areas corresponds to the Capbreton canyon, which cuts the domain in two following the x direction around y $\approx 160,000$ m. North of the canyon, the mean wave energy flux ranged from 25 to 34 kW/m with an average of 27 kW/m. South of the canyon, the wave energy flux progressively decreased to values between 10 and 25 kW/m with an average around 20 kW/m. This decrease was

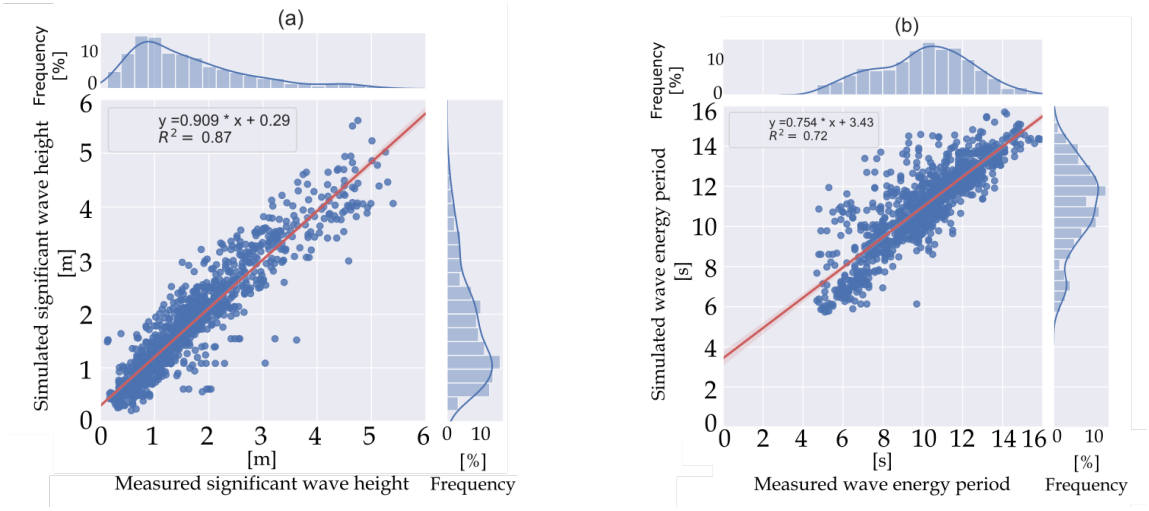

Figure 4.2: H_{m0} scatter plot; (b) T_e scatter plot

mainly due to refraction of the wave field over the strong bathymetric gradients on each side of the canyon, which tended to focus energy in the north while creating a "shadow area" in the south. It can be noted here that the refined grid resolution over the specific bathymetric feature of the canyon seemed to be crucial to capture the related impact on the local wave resource, whereas this effect could be underestimated or even ignored by coarser regional simulations. Another contribution to the north–south coastal energy gradient may have arisen from the protective effect of the Spanish coast for wave systems propagating from the southern part of the Atlantic basin with west incident direction. However, these systems are not dominant in the studied region, suggesting a more limited impact on the obtained spatial distribution.

Upon examining the results further onshore in Figure 4.3, the effect of wave–bottom interactions was found to further intensify, resulting in a very heterogeneous wave energy distribution. Along the coast, some areas clearly focused wave energy while others received significantly less energy, mostly due to local refraction by the bathymetry. For instance, due to refraction over the Capbreton submarine canyon, wave power was very weak (5–6 kW/m) in front of Capbreton (see the location of the Capbreton Marina, noted F in Figure 4.3). Conversely, right in the south and in the north of Capbreton, energy was focused and power reached 25–27 kW/m in the Capbreton/Labenne area in the south (noted G in Figure 4.3) and more than 30 kW/m in front of Hossegor/Seignosse zone (noted E in Figure 4.3), with the latter being famous for its world-class surfing spots. Another hotspot of wave power was found in front of Vieux Boucau approximately 20 km north of Capbreton (noted D in Figure 4.3). In this place, a maximum mean wave power of 34 kW/m was obtained, which was the maximum over the whole studied domain. In the southern half of the domain ($y < 160,000$ m), very localized spots with higher wave energy were obtained, here again due to refraction over the complex bathymetry in this mixed sandy/rocky region. Such wave energy "patches" were found, e.g., along Anglet shore close to the Adour estuary (noted H in Figure 4.3), or in the Saint Jean de Luz nearshore area (noted I in Figure 4.3), which is also known for a localized bathymetry focusing effect (e.g., the so called Belharra giant wave). To further quantify these strong local variations in wave energy, Figure 4.4 depicts the longshore profiles of wave energy

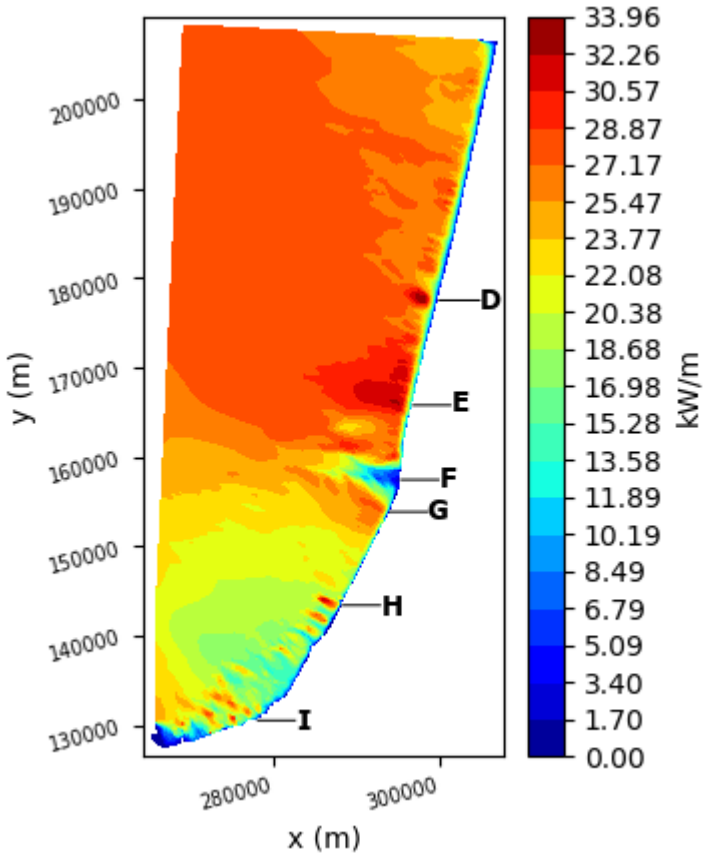

15cm

Figure 4.3: Spatial distribution of wave energy flux averaged (kW/m) over 1958–2001

resource following 20 m (top) and 10 m (bottom) isobaths. The key points mentioned above are clearly visible again on this plot, especially the remarkable drop in wave energy related to the Capbreton canyon. Furthermore, the wave energy maximum located off Vieux Boucau can be seen at 10 m depth. Another interesting feature when comparing results at 20 m and 10 m depths was the shoreward increase wave energy at this point, resulting in the 34 kW/m maximum at 10 m water depth. This emphasizes again the interesting additional information provided at the local scale by the refined computational grid. Moreover, it suggests that shallow-water wave focusing may have generated local maxima in wave energy that exceeded the offshore resource, confirming that the maximum resource was not always to be found offshore.

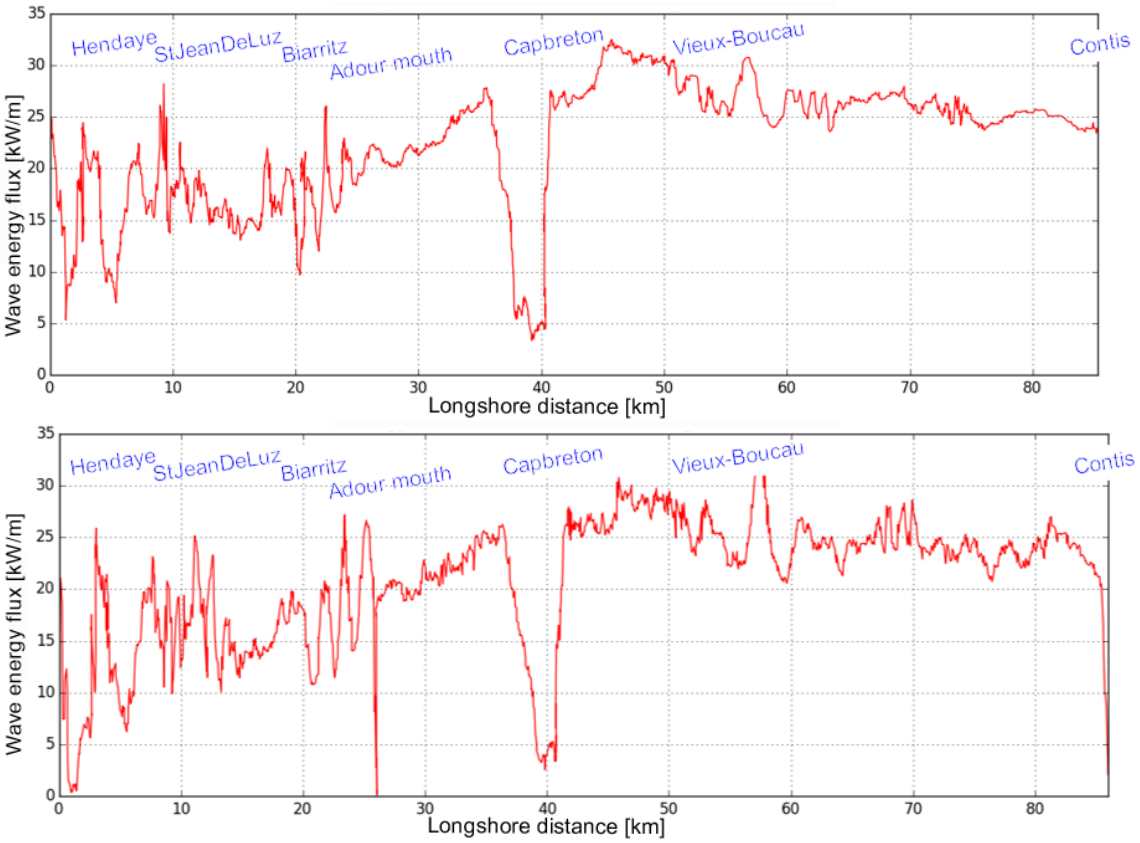

Figure 4.4: Mean energy flux longshore profiles following isobaths at 20 m (top) and 10 m (bottom).

4.3.2 Offshore and Nearshore Wave Parameter Distribution

In view of the results of the previous section, two hotspots are specifically studied in this section: (i) Point A in Figure 4.1, which benefits from optimum incoming wave energy in the offshore part of the domain; (ii) the Hossegor/Seignosse area, which appears to be the main nearshore energy hotpot. Firstly, Figure 4.5 shows the distribution of the annual wave energy depending on the significant

wave height H_{m0} and the energy mean period T_e. The wave energy was obtained by integrating the wave power over the time frames corresponding to the corresponding wave parameters. Figure 4.5 shows that most of the annual energy was provided by sea states with wave heights ranging from 2 to 5 m and wave periods from 10 to 15 s at point A. The distribution was a little bit different at the Hossegor/Seignosse hotspot with larger heights and period ranges involved, i.e., 2–10 m and 8–18 s, respectively, although most of the energy was still carried by waves with characteristics similar to point A. At both hotspots considered, coarsely, half of the annual energy was roughly provided by numerous sea states with moderate energy fluxes (Pw $<$ 50 kW/m), while the other half was generated by rarer events of larger intensities. Remarkably, the latter were more frequent in the Hossegor/Seignosse area than at the offshore location considered. Thus, the coastal propagation, especially the focusing on Hossegor/Seignosse, tended to shift the availability of the wave resource toward larger wave heights and periods, in addition to an overall broadening of range of wave parameters with significant energy flux compared to the offshore.

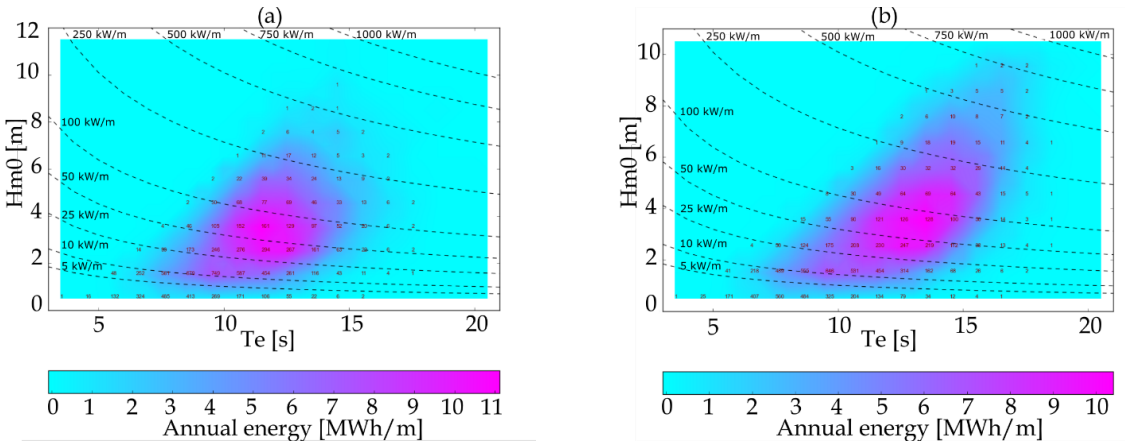

Figure 4.5: Annual wave energy in [MWh.m-1] versus wave height and energy period: (a) point A; (b) Hossegor/Seignosse. Dashed lines represent isolines of energy flux

The annual energy distribution is also plotted in terms of significant wave height and peak direction in Figure 4.6. At point A, the energy was provided by a directional window between 280° and 310°, with most of the energy being provided by a 10° angular sector between 290°and 300°. At Hossegor/Seignosse, the energy was provided by a directional window between 275° and 305°, while most of the energy was provided by a 10° angular sector between 285° and 295°. Here again, this new set of information about the local wave resource may be of interest for WEC design and sizing, as well as efficiency evaluation at a specific installation point in the coastal area.

4.3.3 Time Variability of the Coastal Wave Energy Resource

We now examine the time variability of the resource. By considering seasonal variations, Figure 4.7 firstly shows the distribution of wave power in winter and summer. In winter, the distribution of hotspots was similar to that obtained when considering the entire year. A maximum winter wave power of about 62 kW/m was obtained in two locations. Although the wave resource was of the same magnitude, the spatial extent of the hotspots was different. The hotspot off Vieux Boucau

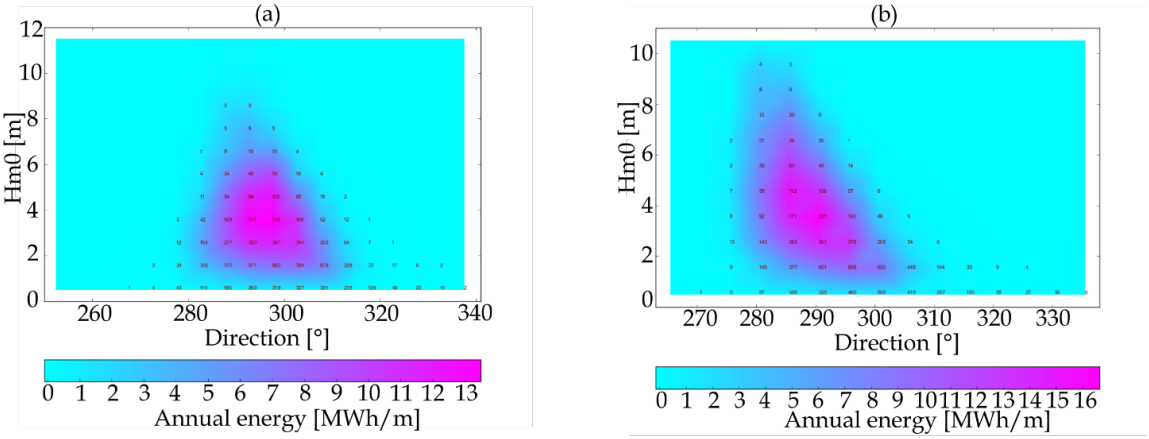

Figure 4.6: Annual wave energy in $[MWh.m^{-1}]$ versus wave height and direction: (a) point A; (b) Hossegor/Seignosse

in the north was much smaller than the hotspots off Capbreton/Hossegor. In the southern part of the domain, the wave power ranged from 20 to 40 kW/m outside very local focusing points.

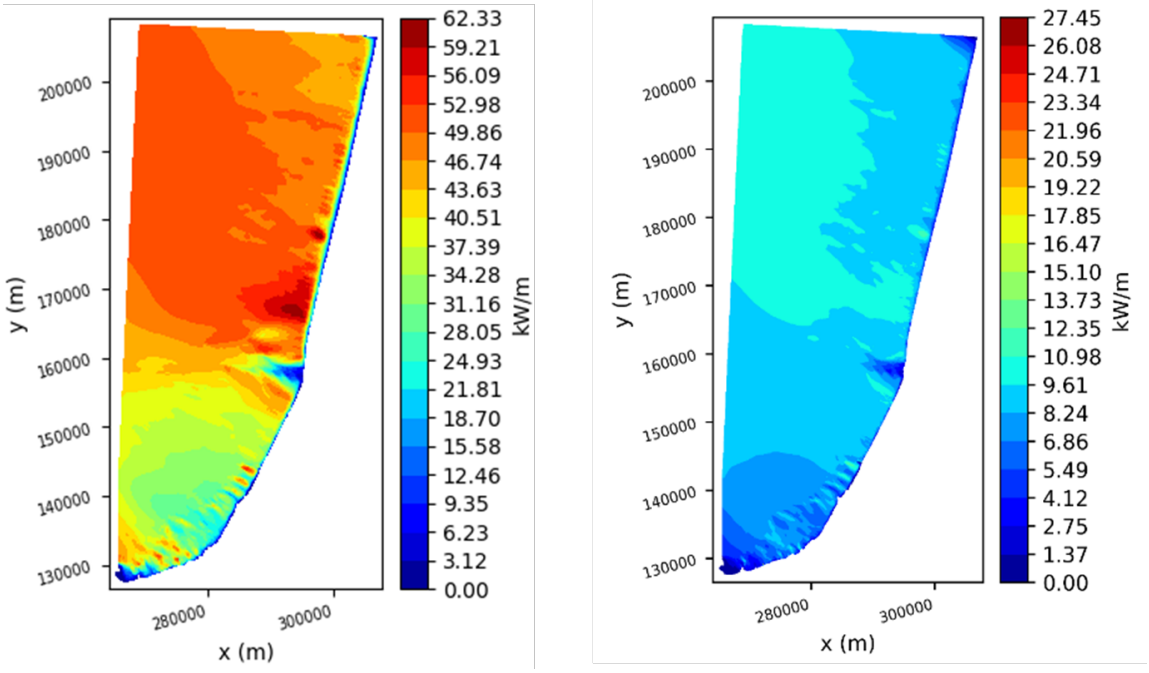

Figure 4.7: Spatial distribution of wave energy flux (kW/m) in winter (left panel) and summer (right panel) averaged over 1958–2001

In summer, the situation drastically changed, with very low values of wave energy. The effect of the submarine canyon on the distribution of the wave energy resource is still visible in the right panel of Figure 4.7; however, there were no more areas with a strong focusing effect, and the discrepancies between the northern and southern part of the domain were also not as important as for the winter season. North of the submarine canyon, the wave power varied between 8 and 11 kW/m, while, in the south, the values were quite similar, ranging from 5 to 10 kW/m. Comparing these values to the mean values in winter, an energy decay of about 80% was observed in the north and an energy decay of roughly 75% was observed in the south.

The computation of the variability index introduced by [Cornett 2008] was performed to generalize the analysis of the variability to the whole domain. The coefficient of variation (COV) was obtained by dividing the standard deviation of the monthly mean wave power by its mean value over 44 years. Therefore, a COV equal to 1 corresponds to the case where the standard deviation is equal to the mean value. Examining the COV map plotted in Figure 4.8, we can observe that the temporal variability of the wave energy flux was rather uniform over the whole domain. However, it can be noted that the variability was slightly higher north of the Capbreton submarine canyon.

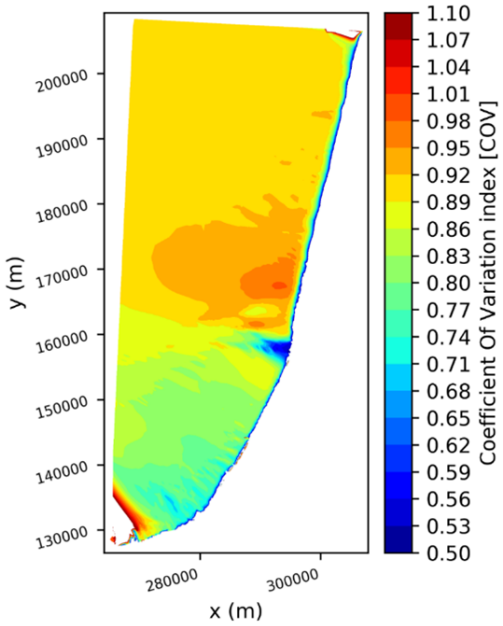

Figure 4.8: Spatial distribution of wave energy flux temporal variability represented by the coefficient of variation COV

The same analysis was carried out for the seasonal variation index (SV) and the monthly variation index (MV). Here, considering the 44 year mean wave energy flux, the seasonal variability index was obtained by computing the difference between the mean values of the most energetic season (December–February) and the mean values of the least energetic one (June–August), normalized with respect to the annual mean. For the monthly variation index, the same computation was done using the most and least energetic months.

Figure 4.9 reveals the same pattern for the spatial distribution of the wave energy variability

indexes as in Figure 4.8, with an accentuated separation between the south and the north of the Capbreton submarine canyon. In the southern part of the domain, SV ranged between 1.1 and 1.3 and MV ranged between 1.3 and 1.7. In the northern part of the domain, SV ranged between 1.4 and 1.7 and MV ranged between 1.8 and 2. Here again, the variability appears to be higher in the northern part of the domain. Additionally, we can observe that the areas with the highest wave energy resource described in Section 3.2 of the present study were also the areas with the highest variability.

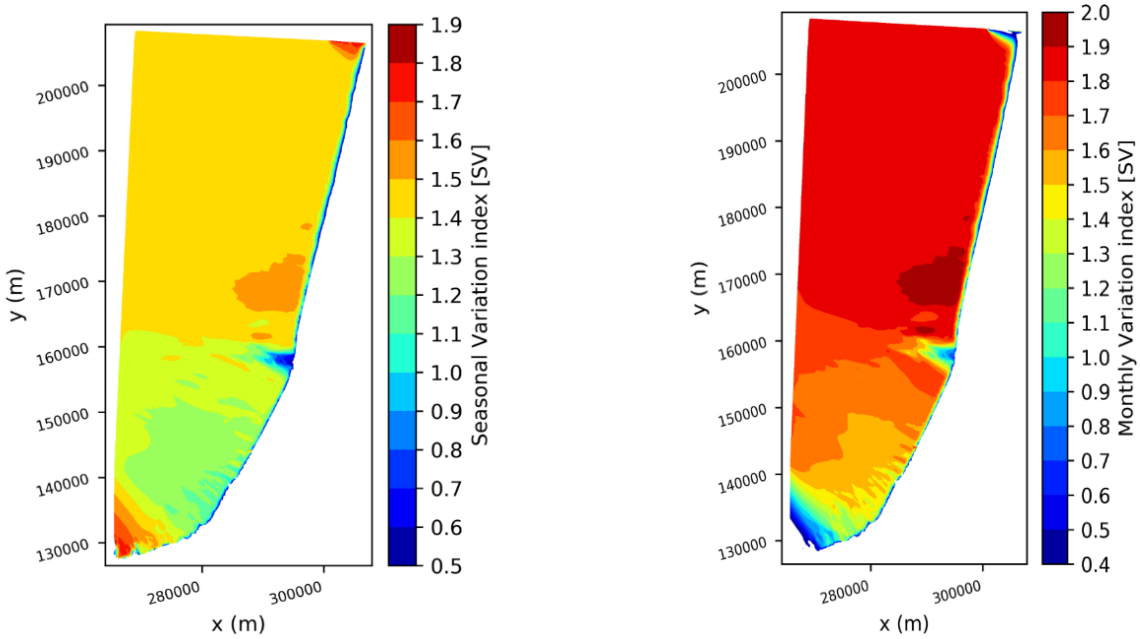

Figure 4.9: Spatial distribution of seasonal variability index of wave energy flux (SV) (left panel) and monthly variability index of wave energy flux (MV) (right panel)

Given the rather long duration of the coastal wave hindcast produced for this study, we examined the temporal variability in the wave resource to identify if a long-term trend was present. In fact, a WEC device has a lifetime of some decades; therefore, its design must fit the local resource to perform optimally over the whole period of exploitation. As shown in previous paragraphs, the south Aquitaine coastal shelf can be divided into two areas with different wave energy levels, namely, north and south of Capbreton canyon. To assess the long term variability of the resource in these two areas, two points were specifically studied, one in the north (located offshore of Capbreton at 23.9 m water depth, represented by green squares in Figure 4.10) and the other one in the south (located offshore Bayonne breakwater at 26.4 m water depth, represented by red triangles in Figure 4.10). In Figure 4.10, extractions of the annual wave energy flux, inter-annual variability between two consecutive years, annual wave energy maximum, and the 98th percentile of the annual wave energy on these two control points are plotted for the 44 year hindcast duration. Linear regressions

are also plotted to assess the evolution of these parameters over the hindcast duration.

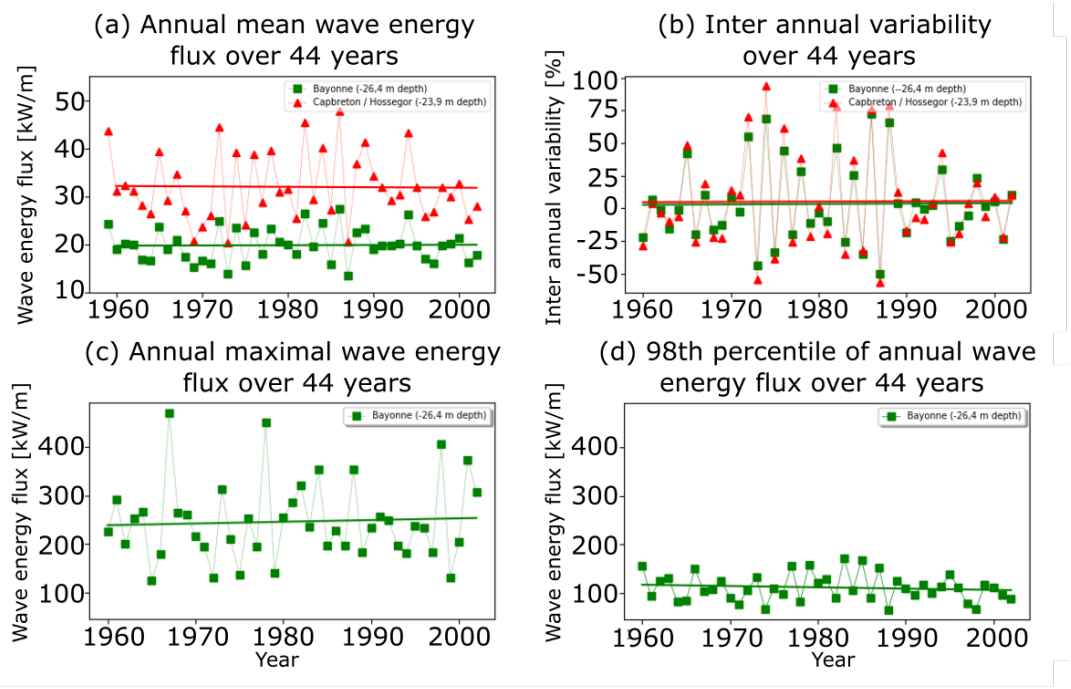

Figure 4.10: (a) Annual wave energy flux for the Bayonne (green squares) and Capbreton (red triangles) locations over the 44-year hindcast period. (b) Inter-annual variability between two consecutive years as a percentage. (c) Annual maximal wave energy flux for the Bayonne location. (d) The 98th percentile of the annual wave energy flux for the Bayonne location

As expected, the levels of wave energy observed in the a panel of Figure 4.10 were different at the two considered points. At the Bayonne location, wave power ranged between 15 and 25 kW/m with an average value around 20 kW/m. At the Capbreton/Hossegor location, the wave power ranged between 20 and 47 kW/m with an average value around 30 kW/m. Between two consecutive years, the resource was shown to vary significantly. The figure also highlights the fact that, even if the two points present different seafloor characteristics (sandy seafloor with small bathymetric gradients in the north and rocky seafloor with sharp bathymetric gradients in the south), the wave power evolved in a similar way, meaning that the inter-annual variability depended highly on the forcing. The similitude in the behavior of the wave energy was confirmed by the (b) panel of Figure 4.10, where the inter annual variability is plotted for the two locations. Although the evolution was almost identical, it appears that the inter annual variability was slightly higher at the Capbreton/Hossegor point. The relative variations in Capbreton/Hossegor ranged between -57% and +93%, while, in the Bayonne location, the variations ranged between -50% and +72%.

Looking for long term trends in the plotted timeseries, Figure 4.10 shows that the strong inter-annual variability and the absence of repetition patterns in this variability do not allow making

conjectures on long term resource evolution. When computing linear regressions, it appears that the linear correlation coefficients are extremely low, indicating that a linear evolution of the wave energy resource is to be discarded. The slopes of these regressions, although close to 0, are not relevant given the absence of any linear behavior in the simulated timeseries. Higher-order regressions were also tested (2, 3, 4) with the same results, i.e., a very low regression coefficient.

4.4 Discussion

The extensive dataset provided by the high resolution coastal wave hindcast allowed an assessment of the local wave energy resource variability in both time and space. When studying the spatial variability of the resource, the most remarkable feature was the strong effect of the Capbreton's submarine canyon. The latter induced a separation of the coastal area in two domains: one domain lying north of the submarine canyon where wave energy was focused, and the other one in the south, where the coast seems to be sheltered by the refraction over the submarine canyon. Furthermore, the strong longshore variability in the southern part of the studied area was also noticeable. Compared to the northern part, the wave energy fluctuated much more over the locally very heterogeneous bathymetry. While the northern part is characterized by a sandy coast with more uniform bathymetry, the southern part is composed of a rocky seafloor related to steep bathymetric gradients. Although these gradients were smaller than those observed in the submarine canyon, they had a strong impact in terms of local focusing effect of the wave energy resource in the coast south of Bayonne. Overall, local wave refraction appeared to be the major process controlling local wave resource in the coastal area. Although a coastal region was potentially shown to have an interesting wave energy overall resource, local effects in finite depth may have strongly modulated the resource, sometimes by a factor of two. This may be an opportunity to increase the production or a threat for the system survivability, depending on the configuration. In any case, results obtained in this study strongly support the need for high resolution coastal wave investigation to properly optimize coastal WEC installation.

Regarding long term temporal trends, in light of the present work, it seems not possible to draw any conjecture about future wave energy resource evolution. Over the 44 years covered by the hindcast, the wave energy was shown to vary a lot between two consecutive years, with variations values reaching up to 93%. However, this very high variability could be explained by more global phenomena like the North Atlantic Oscillation (NAO). Good correlations were obtained between wave energy resource and climate indices [Santo et al. 2015][Dodet, Bertin, and Taborda 2010]. The work of [Dodet, Bertin, and Taborda 2010] indicates positive trends, both in H_s ($+0.005\ m.year^{-1}$) and in T_p ($+0.01\ s.year^{-1}$) at the 45°N latitude. However, this trends are not visible in the hindcast studied here. Understanding and better quantifying the link between wave energy resource and the pressure anomalies, together with improving the ability of predicting accurately those pressure anomalies, would benefit the ability to predict future wave energy resources. Even if multi-annual predictions of the NAO are not yet achieved, recent studies showed that it might be possible using enhanced models capable of better capturing the behavior of the atmosphere and its driving factors.

The present study also showed the wave conditions to be very different along the year. The values of the COV found in this work are in good agreement with previous studies carried out at global scale [Martinez 2020]. While, in winter, the wave energy resource was very high, in summer, it decreased significantly. This underlines the fact that annual mean values of wave energy should

not only be considered when designing a WEC project as they do not carry all the information about the resource, especially its intra annual variability. It is important to emphasize that the expected energy production of a WEC will be very different between winter and summer, and that policymakers should not expect a WEC device to produce an average amount of electricity all over the year. Moreover, these relative variations were also shown to be similar between the northern and southern parts of the domain. However, even if the relative variations were equal, the absolute variations were not, due to the different wave energy levels. Thus, the variations in the southern part of the south Aquitaine coastal shelf ranged between 2 and 12 kW/m between two consecutive years, while, in the north, these variations ranged between 2 and 27 kW/m. Therefore, from a WEC installation point of view, it seems important to consider two aspects, namely, the wave energy overall resource and the resource temporal stability. Indeed, previous studies already mentioned that stable energy levels might be more interesting than fluctuating high-energy values [Roland and Ardhuin 2014]. Nevertheless, this study highlights the interest of a long hindcast period as it can provide valuable information to WEC designers about several important aspects. These variations are interesting both for an energy production optimization process or for resistance design against extreme events (e.g., winter storms).

During the implementation of the model, some simplifying hypotheses were made. Although their contributions were shown to be negligible due to the small domain studied, various coastal phenomena were disabled (e.g. bottom friction, wave–wave interaction, white capping effect). Further refined studies on, e.g., a specific location potentially eligible for WEC installation, could need further research to include their impact on the wave energy. In addition, a strong hypothesis was made concerning the bathymetry. Due to the lack of continuous bathymetric information over the 44 years of the simulation, the bathymetry was assumed to be constant. This may be a strong hypothesis if the depth considered for the WEC deployment is very shallow (< 20 m), especially considering the sandy seafloor north of Bayonne. In such locations, sediment transport could modify the bathymetry, which, in turn, could affect the wave propagation, thus resulting in variations in the wave energy resource [Hequette and Aernouts 2010]. Dredging works are also often conducted near the Bayonne harbor and may be important to consider. Finally, a last source of discrepancies could be related to numerical aspects, especially numerical diffusion and/or limiters used by SWAN, which may affect the representation of wave refraction over steep bathymetric gradients [Booij, Ris, and L. H. Holthuijsen 1999]; [Roland and Ardhuin 2014]. However, studies carried out over complex bathymetries ([Magne et al. 2007], [Varing et al. 2020]) tend to show the ability of wave spectral models to reproduce wave propagation patterns accurately, while underestimating peak values.

4.5 Conclusions

In this paper, a local wave energy assessment was provided in the south Aquitaine coastal area. Using a high resolution unstructured spectral wave model implementation, a 44 year coastal wave hindcast was built. This hindcast was validated against wave buoy data collected over five years. The spatial mapping of the resource underlines the great impact of the submarine canyon of Capbreton, resulting in a remarkable south–north energy gradient in the region; the average power was 27 kW/m north of the canyon and 20 kW/m in the south (i.e., a variation of about 35%). Similarly, the presence of such bathymetric gradients induced specific wave energy focalization in hotspots, with the most important being found off the coast of Vieux-Boucau and between Hossegor and Seignosse. Alongside the study of the spatial variation of the wave energy resource, the quantifica-

tion of temporal variability was addressed, benefiting from the rather long duration of the hindcast dataset. The variability of the resource was shown to be very high at both intra-annual (decay of 80% between summer and winter) and inter annual levels (up to 93% variation between two consecutive years). However, no long term trend was identified due to chaotic inter annual variability.

An extra step toward the installation of WEC devices in the French Basque coastal area would require precisely defining their locations. The energy focusing locations described in this paper would, therefore, need higher-space resolution meshes to capture very local variations, which could be part of further investigations.

Chapter 5

Origin and influence of the wave energy spatial, temporal and spectral distribution

A high level of spatio-temporal variability was highlighted in Chapter 4. Variability was observed at both regional and local scale. In Chapter 4, first conclusions were made, but additional results are required to verify them and understand what physical processes are the main driver of the variability over the domain. Two aspects are further studied in the present Chapter: the incident wave forcing and the influence of the Capbreton submarine canyon (locally known as "gouf").

Without any doubt, the forcing by incident waves from the offshore has a major influence on the nearshore wave field. In fact, from the results of Chapter 4, we observe that a gradient is already present at the boundary of the domain (see Figure 4.3). However, understanding which aspects of the forcing induces what kind of variability in the nearshore field is key for understanding the behavior at a given shallow location.

Additionally, regarding the South Aquitaine nearshore area, the influence of the submarine canyon of Capbreton on the nearshore variability of the wave climate is not fully characterized and has to been further investigated. Therefore, additional simulations will be carried out in this chapter to identify the role of this bathymetric feature.

5.1 Origin of the wave energy distribution

5.1.1 Material and methods

Parametric analysis of offshore boundary conditions

In order to study the influence of the forcing on the whole domain used in Chapter 4, a parametric analysis is carried out, taking in consideration the wave climate studied in Chapter 4. The grid presented in Chapter 4 is forced with a homogeneous JONSWAP spectra along its borders. The influence of the significant wave height H_s, the peak period T_p and wave direction (See Table 5.1)

	H_S	T_p	Wave Direction	Number of simulation
Variability on H_s	Varying from 0.5m to 5.5m with $\Delta = 0.5m$	12s	290°	11
Variability on T_p	$H_s = 2m$	Varying from 5s to 18s with $\Delta = 1s$	290°	14
Variability on wave direction	$H_s = 2m$	12s	Varying from 270 °to 360° with with $\Delta = 5°$	19

Table 5.1: Summary of the parametric analysis

on the nearshore variability is then studied. To make the results more readable, the outputs of the model (i.e. H_s, T_E and wave energy) are normalized with the corresponding incident wave parameter.

To illustrate the effects of the varying offshore boundary condition on the nearshore wave energy, three specific locations are studied, (See Figure 5.1) : the bay of St Jean de Luz (point A) , the northern breakwater of the Port de Bayonne (point B), and a location North of the Capbreton submarine canyon (point C).

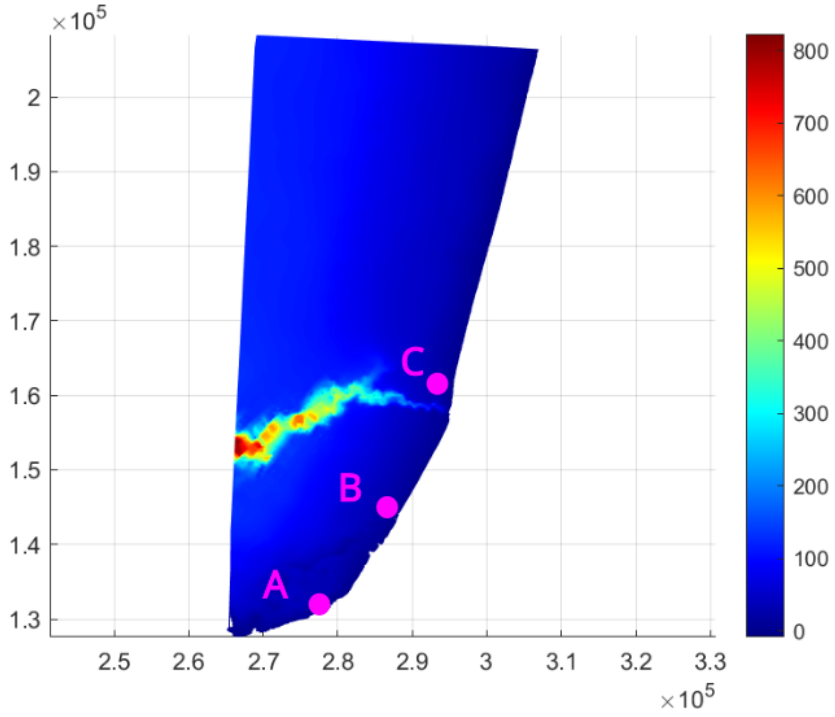

Figure 5.1: Real bathymetry of the domain with the three locations studied. A : Saint Jean de Luz, B : Port de Bayonne's northern breakwater C : Capbreton

Test computational domain with homogenized coastal bathymetry

To study the impact of the Capbreton canyon on the wave field, a test computational domain is created with an artificial homogenized bathymetry (see panel (a) in Figure 5.2). This new bathymetry is based on the same bathymetry that was used in Chapter 4. But the main feature of this new bathymetry is the absence of Capbreton's submarine canyon. In order to create this bathymetry, the location of the gouf was identified by isolating the area surrounded by the strong bathymetry gradients that form the edge of the gouf (see panel (b) of Figure 5.2). Then, over this area, the bathymetry data was removed and replaced by a new bathymetry, obtained through a nearest neighbour interpolation. This operation was carried out with the mesh interpolation tools of the BlueKenue software.

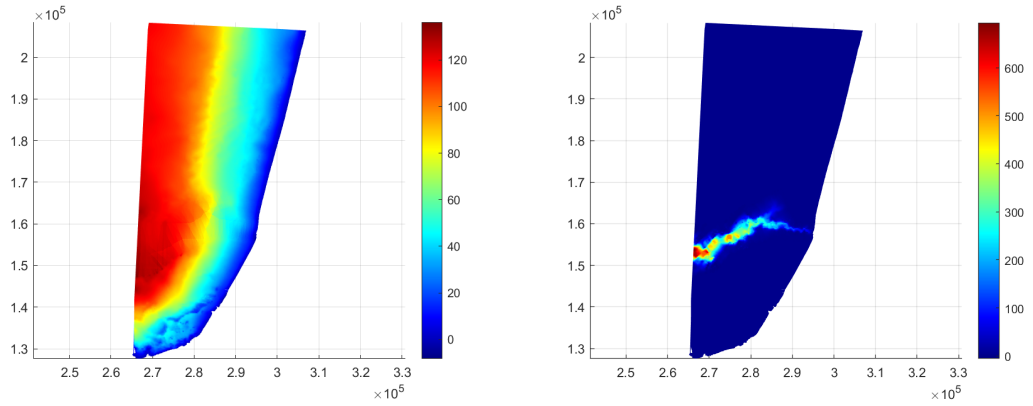

Figure 5.2: (a) Test computational domain without the submarine canyon of Capbreton (b) Bathymetry of the the submarine canyon of Capbreton that was subtracted to the real bathymetry

5.1.2 Results

Influence of the forcing on the nearshore wave field

A high nearshore variability of the sea states was highlighted in Chapter 4. However, the reason behind this variability needs further investigations. In this section the influence of the forcing on the nearshore variability will be assessed. First, the influence of the offshore wave height on the nearshore wave field is presented in Figure 5.3, 5.4 and 5.5. We observe similar wave patterns over the domain for the three cases studied here suggesting that an increase in wave height does not change the wave propagation processes.

Three locations are specifically studied to compare the behaviour of the wave variability at these locations (Figure 5.6). We observe that all locations behave the same way, where an increase in height of the forcing waves induces a linear increase of the local significant wave height. Although the increase is linear at the three locations, the increase is stronger at the Bayonne and Capbreton locations compared to the Saint Jean de Luz location. For Bayonne and Capbreton, an increase of 1m in the incident significant wave height results in a 1m increase in the nearshore while for Saint

Jean de Luz this increase only reaches 0.5m. However, the increased incident wave height does not have an impact on the local wave period.

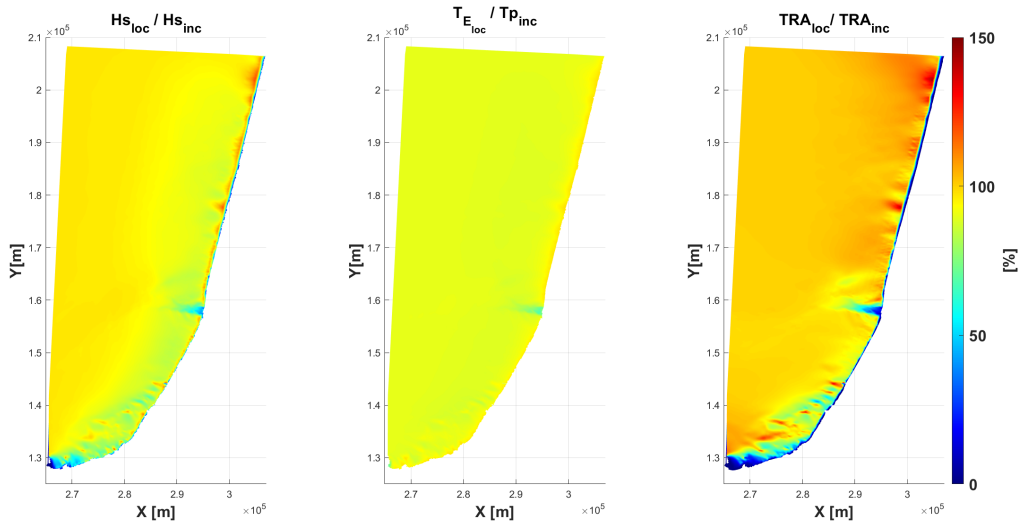

Figure 5.3: Relative difference between local and incident bulk parameters. The grid is forced with the following JONSWAP spectrum : H_s=2m, T_E=12s and $\theta = 290°$

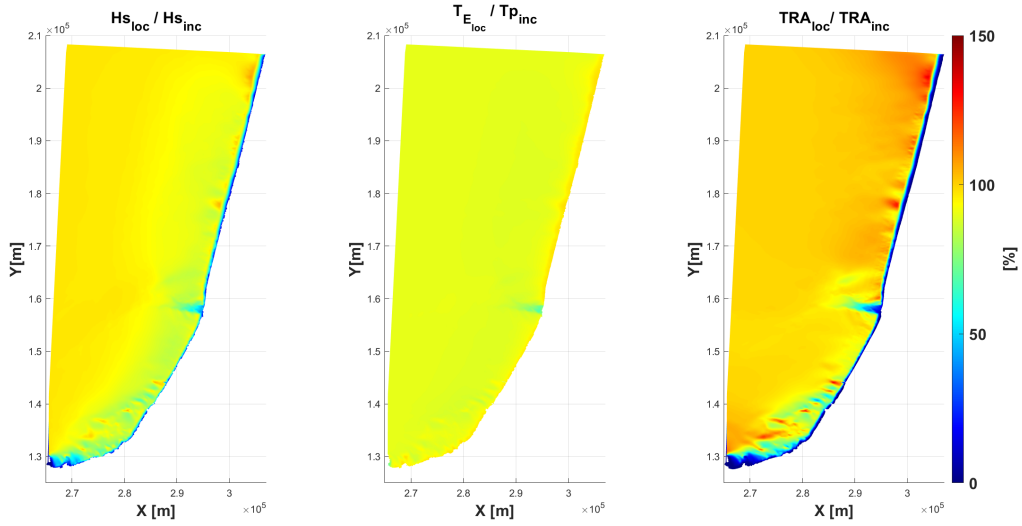

Figure 5.4: Relative difference between local and incident bulk parameters. The grid is forced with the following JONSWAP spectrum: H_s=4m, T_E=12s and $\theta = 290°$

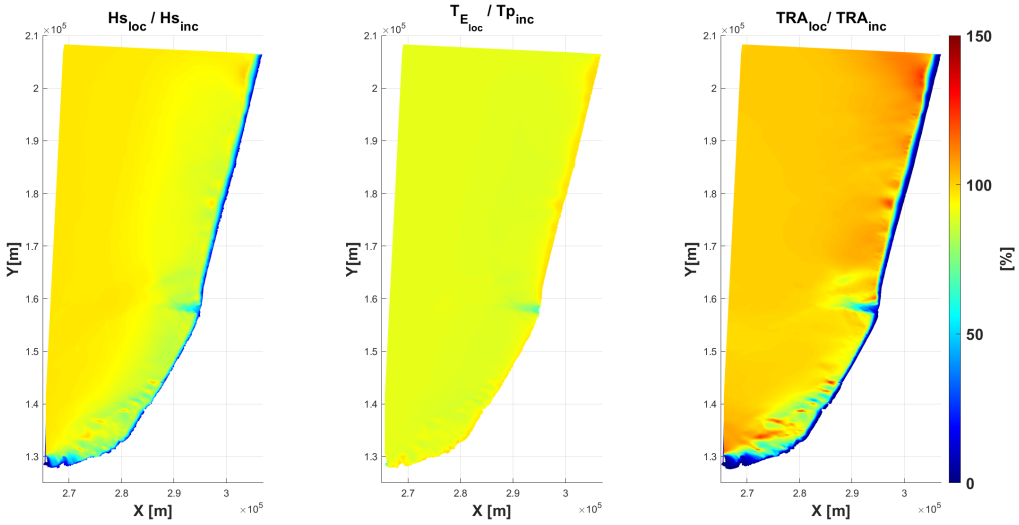

Figure 5.5: Relative difference between local and incident bulk parameters. The grid is forced with the following JONSWAP spectrum: H_s=6m, T_E=12s and $\theta = 290°$

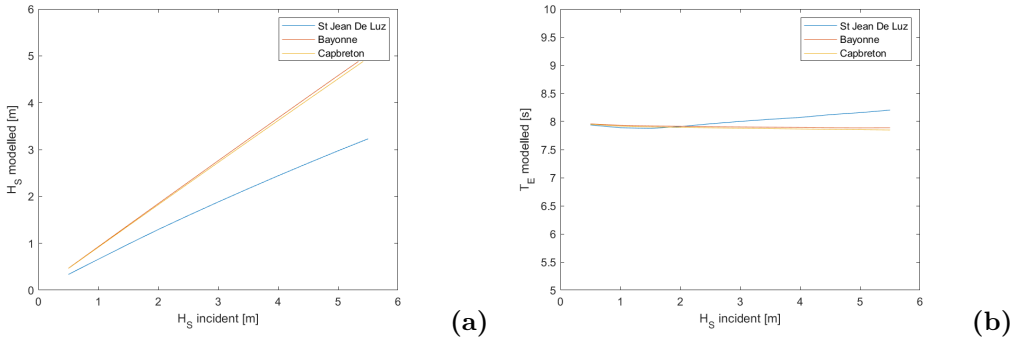

Figure 5.6: (a) Evolution of H_s at three nearshore locations with varying incident offshore H_s (b) Evolution of T_E at three nearshore locations with varying incident H_s

In Figure 5.7, 5.8 and 5.9, we study the influence of the peak period on the nearshore domain. While for $T_p = 6s$, the wave climate appears to be almost uniform throughout the whole domain, increased values of T_p change drastically this result. In fact, we observe that focusing effect start appearing with $T_p = 12s$, especially in the nearshore area. This effect is further amplified with $T_p = 18s$ where the focusing hotspots that were observable for $T_p = 12s$ are intensified.

The influence of the peak spectra T_p is very similar at the three locations studied (see Figure 5.10. The increase in wave period does not seem to affect much the local wave height while the mean wave period T_E is increased. This indicates that the points are not in the focusing areas.

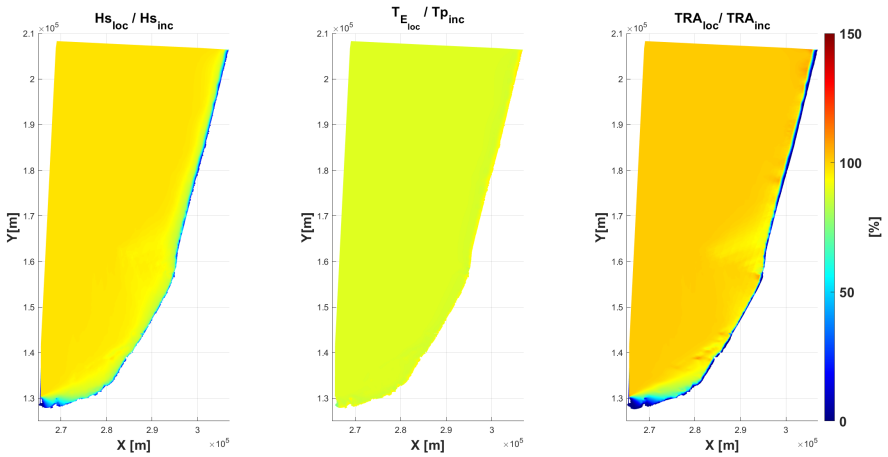

Figure 5.7: Relative difference between local and incident bulk parameters. The grid is forced with the following JONSWAP spectrum: H_s=3m, T_E=6s and $\theta = 290°$

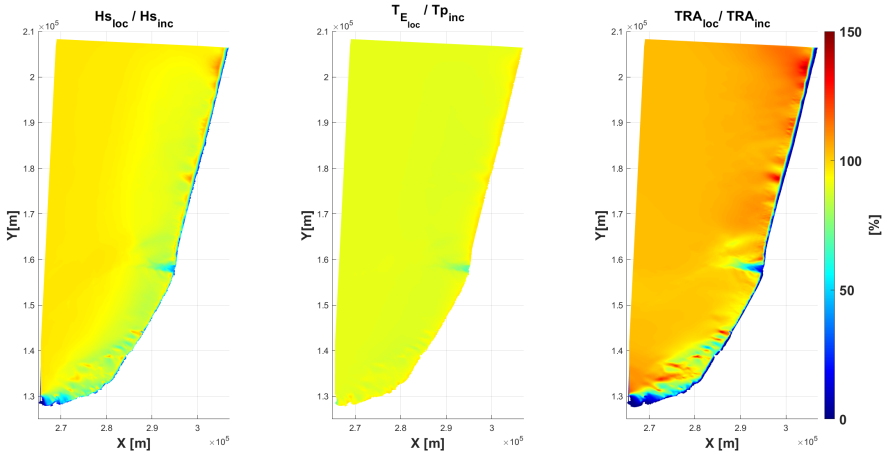

Figure 5.8: Relative difference between local and incident bulk parameters. The grid is forced with the following JONSWAP spectrum: H_s=3m, T_E=12s and $\theta = 290°$

The influence of the wave direction on the wave climate is shown in Figure 5.11, 5.12 and 5.13. When looking at the evolution of the statistical parameters of the sea state at the three locations, we also observe that the evolution of the significant wave height at each location is similar (5.14). However, each location has a preferential wave direction that maximizes the nearshore significant wave height. At Capbreton and Bayonne locations, the significant wave height is the highest for wave direction around 308° while at the Saint jean de Luz location the significant wave height is the highest for wave direction around 325°. This variation can be explained by the fact that the Saint Jean de Luz harbour is oriented towards the north while the coast at Bayonne and Capbreton

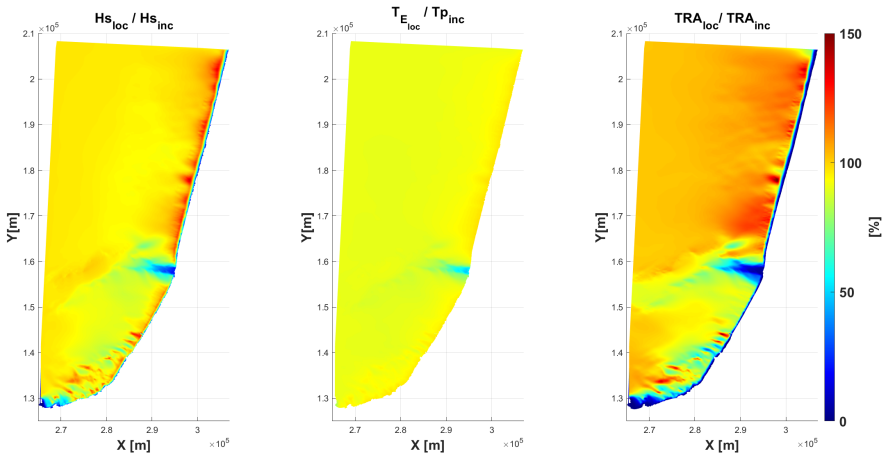

Figure 5.9: Relative difference between local and incident bulk parameters. The grid is forced with the following JONSWAP spectrum: H_s=3m, T_E=18s and $\theta = 290°$

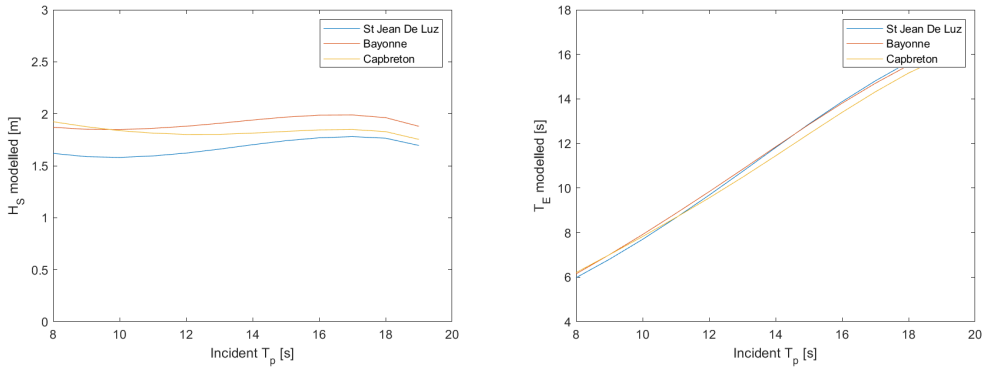

Figure 5.10: (a) Evolution of H_s at three nearshore locations with varying incident T_p (b) Evolution of T_E at three nearshore locations with varying incident T_p

is more north-west oriented.

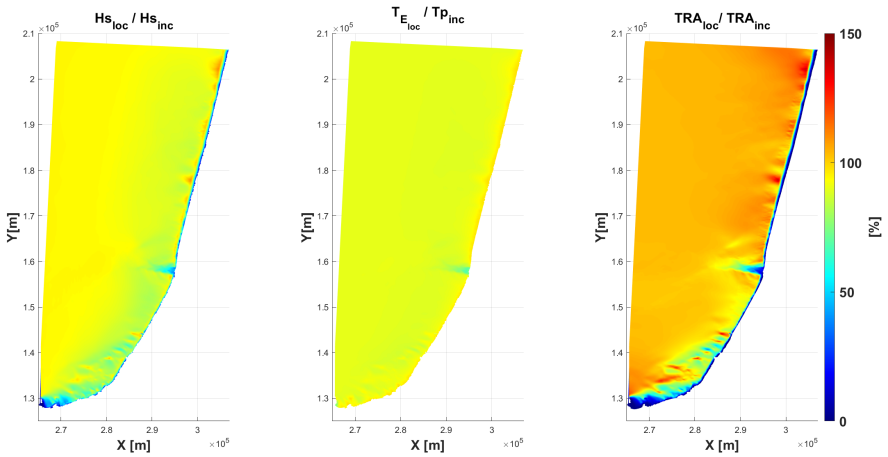

Figure 5.11: Relative difference between local and incident bulk parameters. The grid is forced with the following JONSWAP spectrum: H_s=3m, T_E=12s and $\theta = 280°$

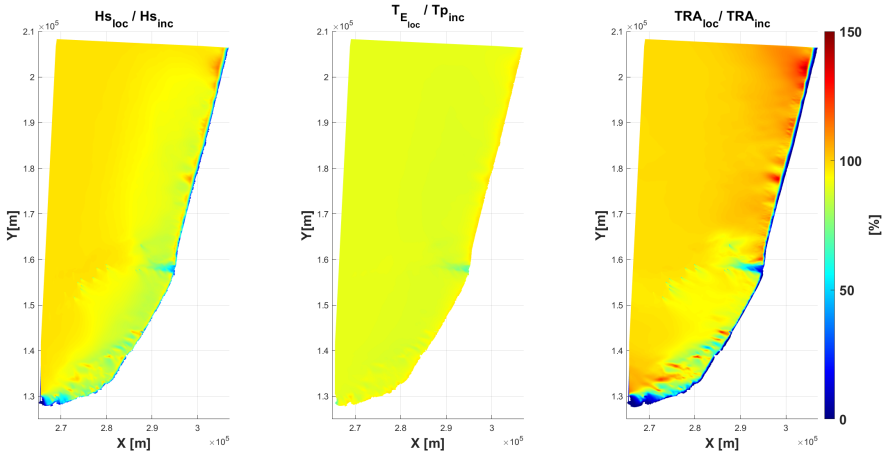

Figure 5.12: Relative difference between local and incident bulk parameters. The grid is forced with the following JONSWAP spectrum: H_s=3m, T_E=12s and $\theta = 300°$

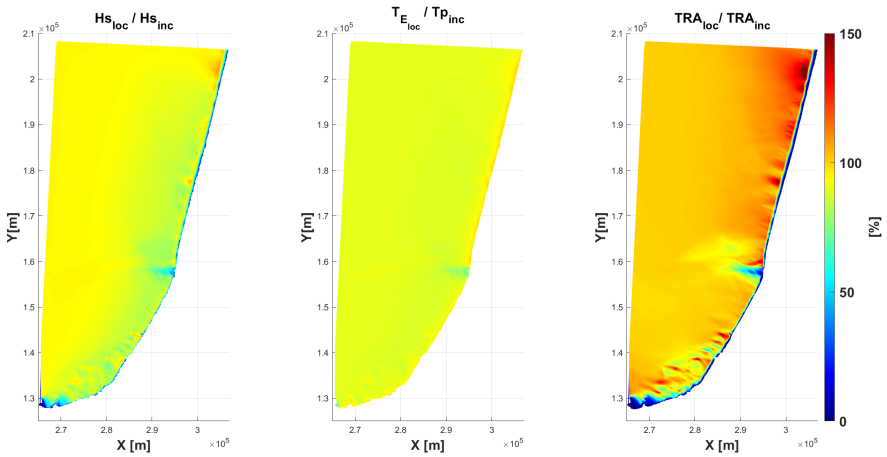

Figure 5.13: Relative difference between local and incident bulk parameters. The grid is forced with the following JONSWAP spectrum: H_s=3m, T_E=12s and $\theta = 320°$

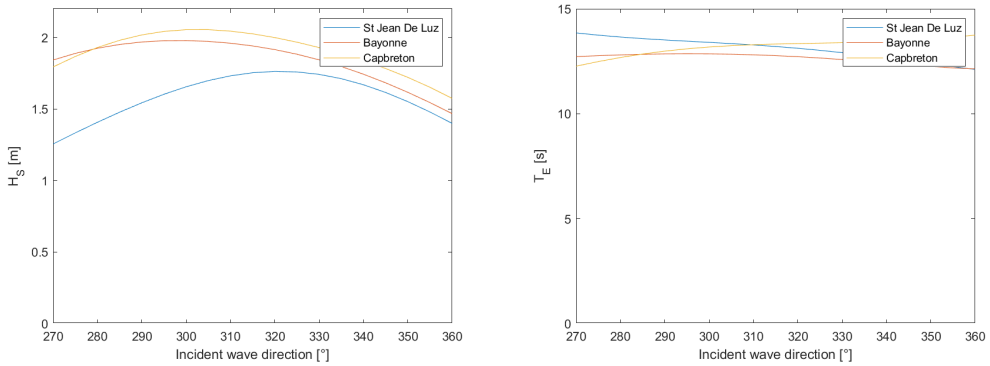

(a) **(b)**

Figure 5.14: (a) Evolution of H_s at three nearshore locations with varying incident wave direction (b) Evolution of T_E at three nearshore locations with varying incident wave direction

Influence of a submarine canyon on the nearshore wave field

To further understand the influence the Capbreton's submarine canyon has on the nearshore wave field, both the bathymetry presented in Chapter 4 and the artificial bathymetry introduced above (Figure 5.2) are forced with homogeneous JONSWAP spectrum. To compare the results, the outputs from the simulations ran with the artificial bathymetry will be subtracted from the output of the simulations with the real bathymetry. Therefore, a positive value at a location will mean that the presence of the submarine canyon increases the computed parameter at this specific location and a negative, the reverse conclusion. The results are plotted in Figure 5.15, 5.16 and 5.17.

As stated in Chapter 4, the submarine canyon has an effect on the nearshore wave climate. However this effect seems to be localized in the vicinity of the canyon, in fact, in a symmetric band approximately 20km wide. Regarding the significant wave height, we observe in the left panel of Figure 5.15, that it is increased both north and south of the canyon. Over the canyon location a large decrease area is observed with values reaching 180 %. The increase levels are rather small, between 2 and 7%. A specific location (X=294km and Y = 160km) has a higher increase level around 14 %. The mean energetic wave period does not seems to be much affected by the absence of the canyon except a high decrease level (- 55%) at the very nearshore (X=294km and Y = 158km) . The same evolution pattern observed for the significant wave height can be seen when looking at the evolution of the wave energy flux. The levels of increase and decrease are however of higher magnitude with decrease values over the canyon reaching -45 % and increase ones, north of the canyon (X=294km and Y = 160km) reaching 30 %. This increasing effect is due to the fact that the wave energy flux is proportional to $H_s.T_e^2$. Therefore, we observe an amplification of the increase (or decrease) where both H_s and T_p were increased (or decreased).

Figure 5.16 shows the evolution of the focusing effect mentioned above with increasing wave periods. The trends are similar geographically, however the magnitude of the evolution is significantly increased. This is mainly caused by increased refraction over the gouf. Indeed, when the wave period is higher, the waves start to refract further offshore. We observe this behaviour in Figure 5.16, around $X = 2.7.10^5 m$, $Y = 1.55.10^5 m$. At this location, for $T_p = 12s$ (upper row of Figure 5.16), we do not observe any difference between the configuration with and without the gouf. However, when the peak period is increased to 18s, a focusing effects start appearing even though the localisation is quite offshore. We also note that higher peak periods tends to increase the size of the area where we observe focusing / converging and diverging effects. However, the northern and southern part of the domain do not seem to be affected by the presence of the gouf, since the result are similar with and without it.

Figure 5.17 shows the evolution of the focusing effect mentioned above with different incident directions. The behaviour of the focusing effect does not seem to be much affected by the change in wave direction.

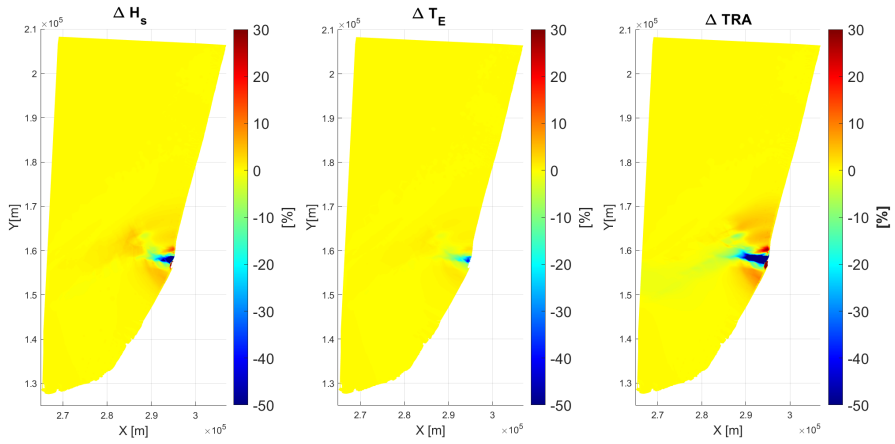

(a)

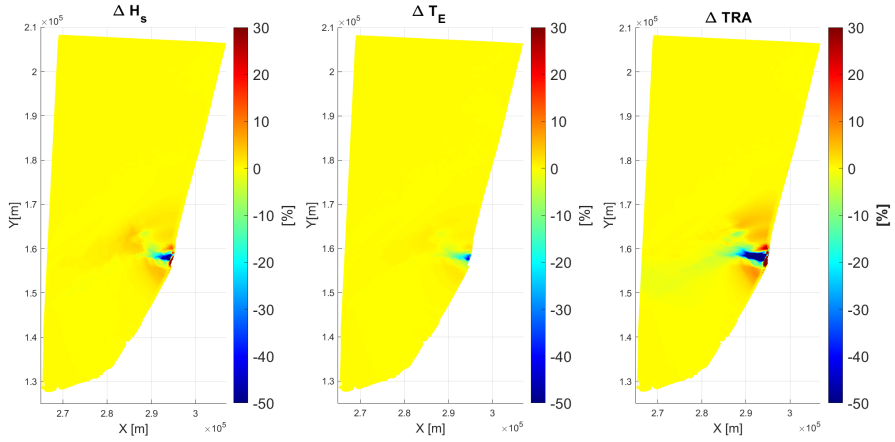

(b)

Figure 5.15: Relative difference between bulk parameters computed with and without the presence of the gouf with increasing H_s. The models are forced with the following JONSWAP spectra (a) H_s=2m, T_e=12s and $\theta = 290°$ (b) H_s=5m, T_e=12s and $\theta = 290°$.

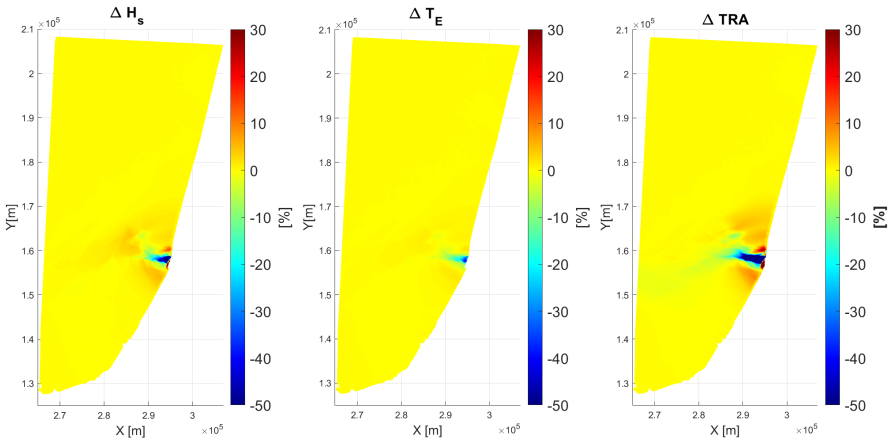

(a)

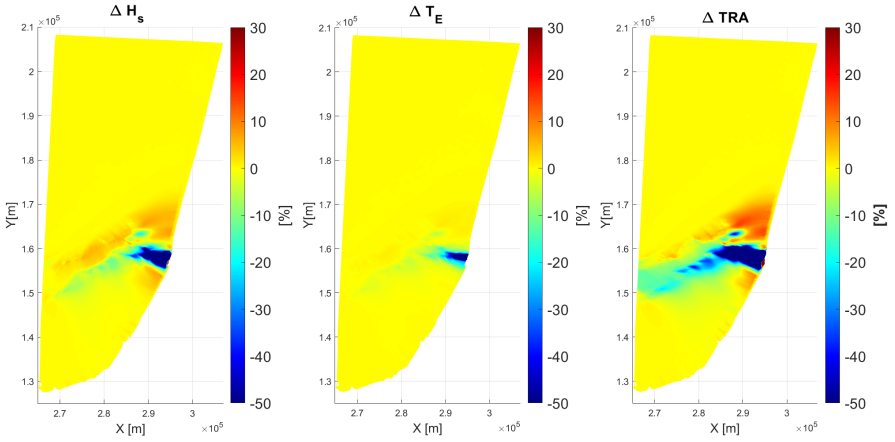

(b)

Figure 5.16: Relative difference between bulk parameters computed with and without the presence of the gouf with increasing T_p. The models are forced with the following JONSWAP spectra (a) H_s=3m, T_e=12s and $\theta = 290°$ (b) H_s=3m, T_e=18s and $\theta = 290°$.

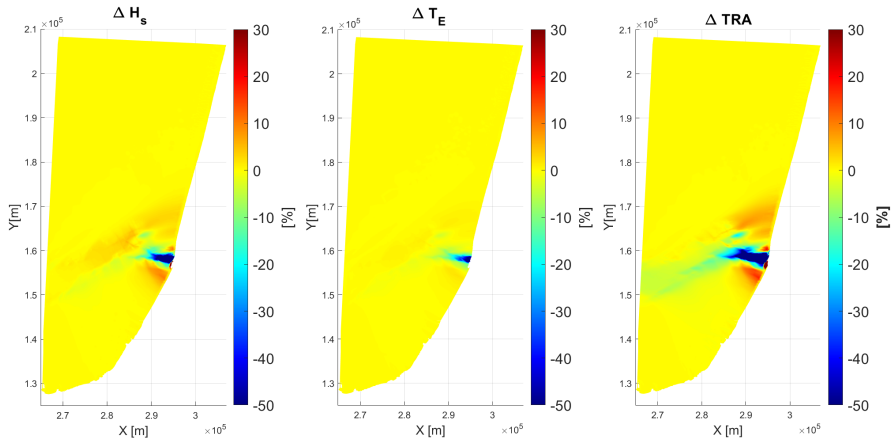

(a)

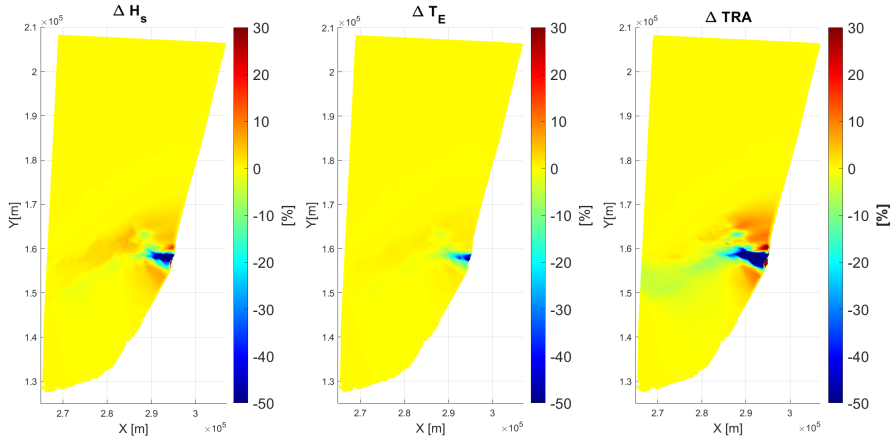

(b)

Figure 5.17: Relative difference between bulk parameters computed with and without the presence of the gouf with increasing Wave direction. The models are forced with the following JONSWAP spectra. (a) H_s=3m, T_e=14s and $\theta = 280°$ (b) H_s=3m, T_e=14s and $\theta = 300°$.

5.1.3 Discussion

The spatio-temporal variability of the wave energy in the South Aquitaine nearshore zone was studied in this chapter. First, the influence of the offshore boundary condition was studied and then the effect of the submarine canyon on the nearshore variability, assessed. The preponderant role of the wave period in the variability was established. This effect could be explained by the

topography of the studied domain since longer waves tend to refract more over strong bathymetry gradient present both in the southern part of the domain and over the Capbreton submarine canyon. An analysis of the effect of the submarine canyon was then carried out. When forced with a homogeneous spectra along the border of our nearshore computational domain, the effect of the submarine canyon was shown to be located in the canyon area. This means that the origin of the North/South gradient observed in Chapter 4 should be found offshore of the domain studied so far.

In order to investigate the origin of the North/South gradient mentioned above, a larger computational domain (see Figure 5.18) is set up. The bathymetry of the extended domain includes now a portion of the continental slope, which makes the transition between the abyssal plain and the continental shelf. We also observe the progressive narrowing of the Capbreton submarine canyon inside the domain. This new computational grid is forced with homogeneous JONSWAP forcing, to separate the respective effects of the canyon versus the spatial variability already included in incident waves. The parametric test over incident values of H_s, T_p ad wave direction is repeated here. Values considered are given in Table 5.2.

	H_S	T_p	Wave Direction	Number of simulation
Variability on H_s	Varying from 1m to 10m with $\Delta = 1m$	14s	300°	10
Variability on T_p	$H_s = 5m$	Varying from 10s to 18s with $\Delta = 2s$	300°	5
Variability on wave direction	$H_s = 5m$	14s	Varying from 280 °to 340° with with $\Delta = 20°$	4

Table 5.2: Summary of the parametric analysis

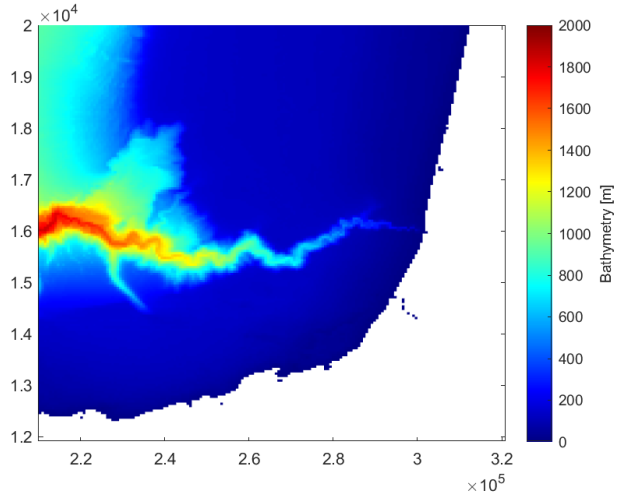

Figure 5.18: Bathymetry of the extended domain used to assess the origin of the North/South gradient observed in Chapter 4

Figure 5.19 shows the spatial distribution of the wave energy flux over the computational domain computed with different forcing H_s. We observe that the spatial distribution of the wave energy is not changed when increasing the forcing wave height. Wave energy hotspots are visible both in

the southern and northern portion of the domain. These results are consistent with the previous results indicating that the forcing wave height is not one of the driver of the nearshore variability.

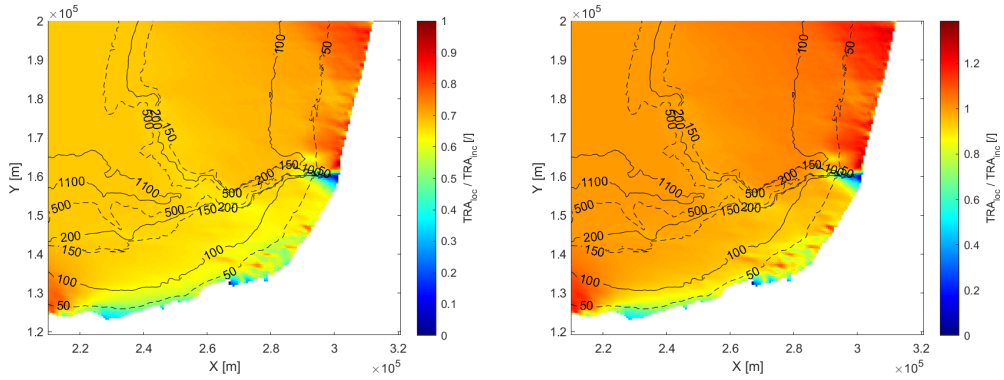

Figure 5.19: Relative difference between local and incident wave energy flux. The model is forced with the following JONSWAP spectra. (a) H_s=3m, T_p=14s and $\theta = 300°$ (b) H_s=10m, T_p=14s and $\theta = 300°$.

The results section of this chapter has already highlighted the strong influence of the wave period on the nearshore variability. Figure 5.20 shows the distribution of the wave energy flux with different wave periods. We observe that for a peak wave period of 10s, there is not much variability in the offshore area of the domain. Variability starts appearing only in the nearshore area. However with the peak period increased to 18s, the results are completely different. High levels of variability between the northern and southern part of the domain are obvious. Additionally, it is interesting to remark that the highest levels of wave energy flux are located in the nearshore area, over the areas already identified in Chapter 4.

The fact that an increase in wave period increases the variability over the domain supports the hypothesis that refraction is a major driver regarding the wave propagation patterns. Figure 5.21 shows a test case where the refraction was turned off in SWAN. This test case was run with a H_s=5m, T_p=18s and $\theta = 300°$ JONSWAP spectra. With the refraction turned off, both the wave direction and the wave energy are almost constant throughout the domain, confirming the strong influence of the refraction for the nearshore variability. We also observe in the left panel of Figure 5.21, shoaling and de-shoaling areas. However, we note that although the wave height is increased and decreased, the wave energy remains constant, indicating that the variation of the wave height is compensated by the variation of the group velocity c_g.

To further understand how the wave propagates over the domain, Figure 5.22 shows the evolution of the wave direction with increased wave period. In the following plots, the incidence range was reduced to the interval [290°, 320°] to increase the contrast. In the left panel of Figure 5.22 (i.e. with the following incident wave forcing : H_s=5m, T_p=10s and $\theta = 300°$), we observe three main types of behaviour. Over the offshore region, the wave direction does not change and remains constant at 300°. Waves start to refract and to change direction only in the coastal region where the water depth is approximately half the wave length in deep water, L_0. For the current wave forcing, L_0 is equal to 156m. Wave should then start to refract around a 80m water depth, which is consistent

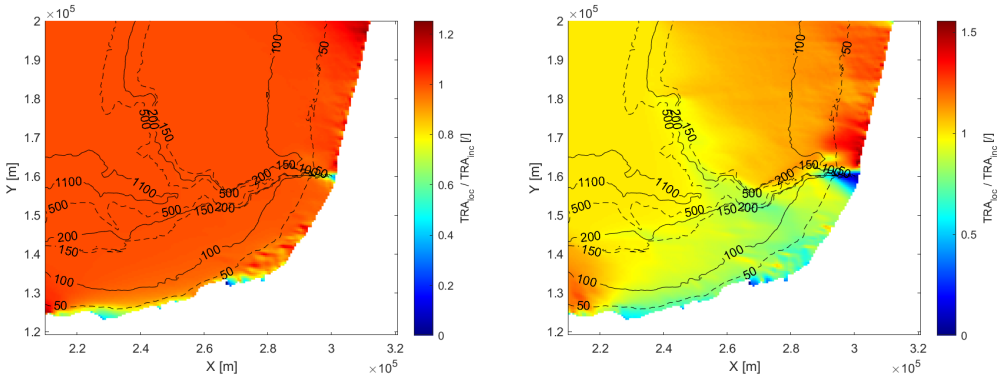

Figure 5.20: Relative difference between local and incident wave energy flux. The model is forced with the following JONSWAP spectra. (a) H_s=5m, T_p=10s and $\theta = 300°$ (b) H_s=5m, T_p=18s and $\theta = 300°$.

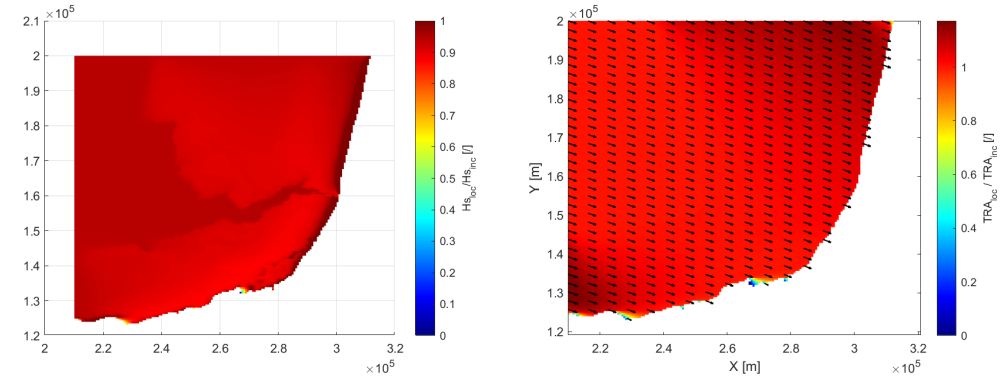

Figure 5.21: Relative difference between local and incident bulk parameters with refraction turned off. The model is forced with the following JONSWAP spectra : H_s=5m, T_p=18s and $\theta = 300°$. (a) Spatial distribution of the H_s (b) Spatial distribution of the wave energy flux, with vectors indicating the wave propagation direction

with the results shown in the left panel of Figure 5.22. In the northern part of the domain, the direction changes to around 295°and in the southern part, it changes to around 303°. Although the same behaviour is still visible in the right panel of Figure 5.22, additional refraction areas are visible further offshore since the wave length L_0 has increased to 480m. Two areas of abrupt transition are especially worth mentioning. The first one separates the northern part from the southern part of the domain around Y=145km. South of this limit, the wave direction is almost exclusively higher than 305°, while in the North, the wave direction is lower than 290°. The second interesting area is located around X=250km and Y $\geq$ 150km. It marks the limit where the initial wave direction of

300°starts shifting to lower values. Both of these areas are located over deep offshore bathymetry gradients visible in Figure 5.18.

In the light of these additional results, wave refraction appears to be occurring at two different scales. First, long waves (i.e. with $T_p > 14s$) refract over offshore bathymetry gradients such as the continental slope and canyon borders. The shape of these gradients appears then to be the reason of the North/South gradient highlighted in Chapter 4. Then a refraction also occurs for shorter waves for smaller water depths. This secondary refraction induce the local wave energy hotspots.

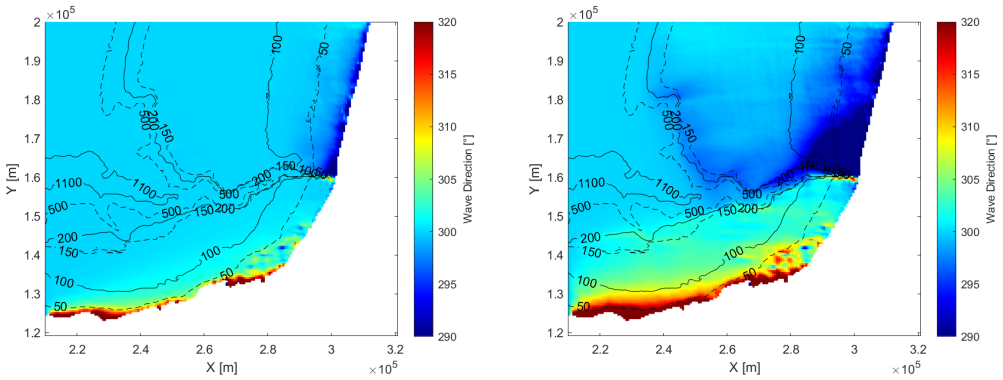

Figure 5.22: Spatial distribution of the wave direction. The model is forced with the following JONSWAP spectra :(a) H_s=5m, T_p=10s and $\theta = 300°$ (b) H_s=5m, T_p=18s and $\theta = 300°$

Finally, the influence of the wave direction on the wave propagation processes is studied. Three wave directions are considered, starting with an almost western swell (280°) and following with a more north-western swell (300°) and finally an almost northern swell (340 °). Figure 5.23 shows the evolution of the wave energy flux for the three wave directions aforementioned. We observe that for the 280°, wave direction the southern coast of the domain receives less wave energy flux compared to the other direction, due to the fact that waves need to refract in order to be able to reach the coast. Then, with more northern swells, the wave energy distribution over the south coast becomes more uniform. The Figure 5.23 also highlights the fact that the wave direction does not change the localisation of wave energy hotspots, only the amount of wave energy they receive. We also remark that with more northern swells, the shadowing effect of the submarine canyon increases.

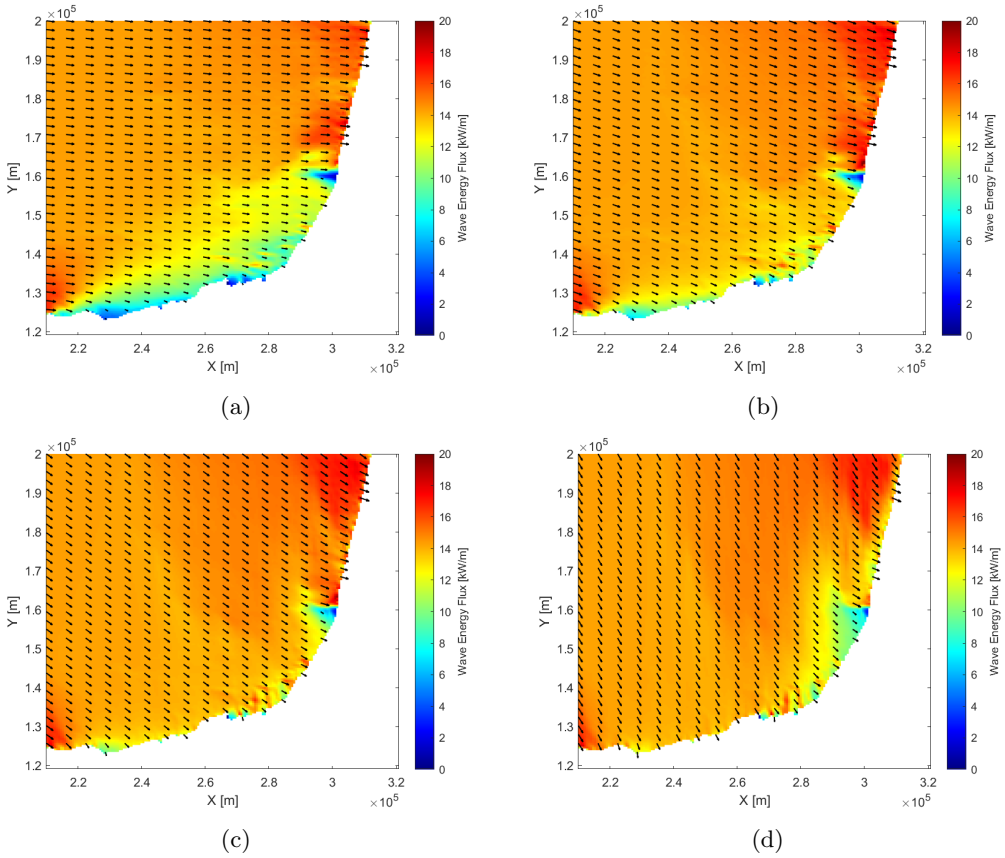

Figure 5.23: Spatial distribution of the wave energy flux. The model is forced with the following JONSWAP spectra. (a) H_s=5m, T_p=14s and $\theta = 280°$ (b) H_s=5m, T_p=14s and $\theta = 300°$ (c) H_s=5m, T_p=14s and $\theta = 320°$.(c) H_s=5m, T_p=14s and $\theta = 340°$

5.2 Influence of high-resolution spatio-temporal and spectral distribution on WEC production estimates

As explained in Chapter 3, most of the wave energy assessment studies mostly focus on studying the statistical bulk parameters used to characterize a sea state (e.g. H_S, T_e). However in order to estimate as accurately as possible the resource, a more detailed description the sea state might be useful. Therefore, a complementary data at high resolution ([Delpey et al. 2021]) is used to give further insight on the spatio-temporal variability in the nearshore area.

This additional data also provides spectral outputs for several nearshore locations, and thus allows to investigate the influence of the spectral distribution on the WEC production estimates. In this chapter, the energy production of a given WEC is computed through two methods. First, a spectral transfer function is used to compute the energy production. Then, from the same spectral transfer function, a power matrix is derived, allowing to compute the energy production from the sea-state's bulk parameters. The comparison of the two outputs will allow us to understand the influence of the spectral distribution on WEC production estimates.

5.2.1 Material and methods

Additional wave data

As mentioned earlier, a high-resolution wave hindcast ([Delpey et al. 2021]), covering a period from 2000 to 2010 is used to investigate the influence of spatio-temporal variability of wave energy on WEC production estimates. An unstructured grid with spatial discretization ranging from 2 km to 10m (see Figure 5.24) is forced with data from the HOMERE database ([Boudière et al. 2013] [Roland and Ardhuin 2014]). This wave hindcast also provides the full wave energy spectrum $E_{f,\theta}$ at 4 nearshore locations (points DL01 to DL04 in Figure 5.24) and 15 locations near the Bayonne breakwater(points DN01 to DN15 in Figure 5.24), an information which is used to compute the output of a WEC.

Computation of the power output of a WEC

We propose to compare the estimated production of WEC through two different methods of computation. The first method consists in applying a spectral transfer function to the modelled wave spectra, which stands for the most accurate method to predict production (providing that such a transfer function is available). The second method consists in using the bulk parameters of the sea states and the power matrix of a given WEC to compute the estimated energy production.

As shown in Chapter 3, there are a lot of WEC technologies. Computing energy outputs requires to choose one specific WEC, since a WEC should be designed for a given location. It is understood that the WEC chosen here may not be the best fit for the local wave climate, The WEC used for the computations presented in this work is a generic heaving device corresponding to an omnidirectional point absorber (see Figure 3.5) from which a power transfer function was built [Maisondieu and Le Boulluec 2016].

The power harvesting capacity of a WEC is defined by its power transfer function $R_p(f, \theta)$. The

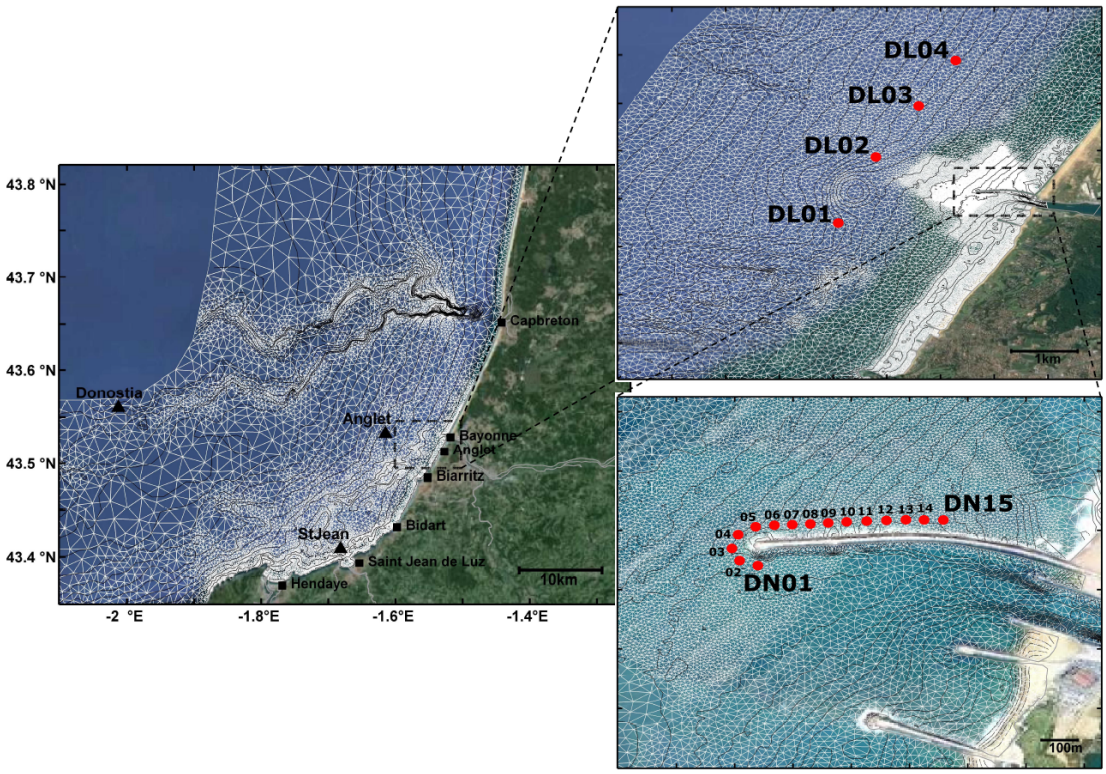

Figure 5.24: Meshing of the model used in [Delpey et al. 2021]

instantaneous power of a WEC is then computed as :

$$P(t) = 2 \int_f \int_\theta R_p(f,\theta) S(f,\theta,t) df d\theta \tag{5.2.1}$$

The WEC presented in [Maisondieu and Le Boulluec 2016] is omnidirectional. It means that it can extract wave energy coming from all directions. Therefore, both the wave spectra $S(f,\theta)$ and the power transfer function $R(f,\theta)$ are integrated over the direction and reduced to $S(f)$ and $R_p(f)$ respectively. The instantaneous wave power is then given by :

$$P(t) = 2 \int_f R_p(f) S(f,t) df \tag{5.2.2}$$

The power transfer function $R_p(f)$ used in this work is shown in Figure 5.25.

Most of the studies use only a discrete transfer function (*i.e.* a power matrix) to estimate the extracted power P_t ([Penalba et al. 2018]). These tables allow to approximate directly the extracted power P_t of the WEC given discrete statistical parameters such as H_s or T_E. An example of such a power matrix is given in Figure 5.26. As said previously each power transfer function and power matrices are computed for a specific WEC. Since a generic WEC is used in the present work, from which we know only the power transfer function, we have to compute its power matrix. Based on

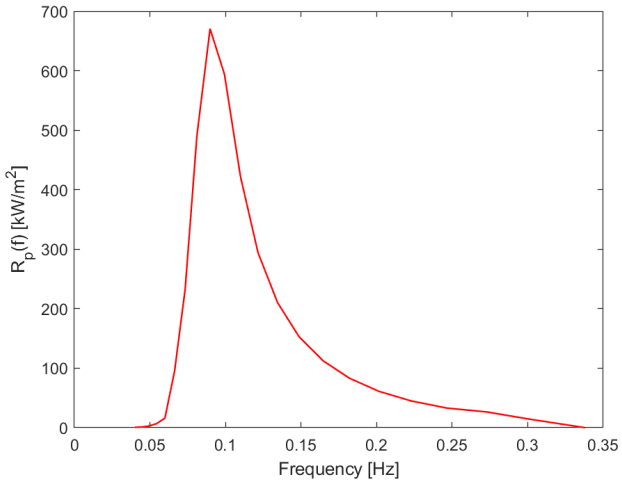

Figure 5.25: Spectral transfer function of the WEc presented by [Maisondieu and Le Boulluec 2016]

equation 5.2.2, one can compute each element $P_{ij}(H_{s_i}, T_{p_j})$ of the power matrix, using on the one hand, the spectral transfer function of the WEC $R_p(f)$ and on the other hand, a known spectra $S_{Hs_iTp_j}(f)$ that we are able to compute from the statistical parameters H_s and T_p. This reads as :

$$P_{ij}(Hs, Tp) = 2 \int R_p(f) S_{Hs_i, Tp_j}(f) df \tag{5.2.3}$$

These (H_{si}, T_{pj}) duets should cover a wide range of values in order to make the Power Matrix as complete as possible. For the computations below, a JONSWAP spectrum has been used. We acknowledge the fact that the use of a JONSWAP spectrum gives good average values but can underestimates peak values [Maisondieu and Le Boulluec 2016]. Figure 5.26 represents the power matrix computed as explained previously, with the spectral transfer function shown in Figure 5.25.

Once the power matrix is computed, an occurrence matrix has to be built. At each time step of the wave hindcast, from the given wave spectra a statistical parameters are computed, and the total amount of hours for each (H_s, T_p) duet is stored on the occurrence matrix (see Figure 5.27) .

Finally, the computation process for both methodologies is summarized in the Figure 5.28 and 5.29.

5.2.2 Results

Influence of spatio-temporal distribution of wave energy on WEC production estimates

The spatio-temporal variability of the wave energy resource was extensively studied over Chapter 4 and 5. However, given the high nearshore variability highlighted throughout this manuscript, this variability should also be studied at smaller scales, to ensure that the WEC fully benefits from incoming waves. Figure 5.30 shows the mean annual energy produced by the WEC along the breakwater computed with the spectral transfer function presented in Figure 5.25. The point DN03

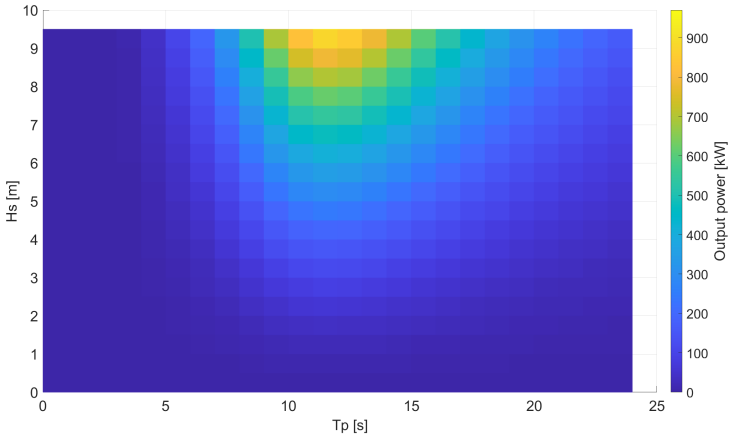

Figure 5.26: Power matrix based on the generic WEC presented by [Maisondieu and Le Boulluec 2016]

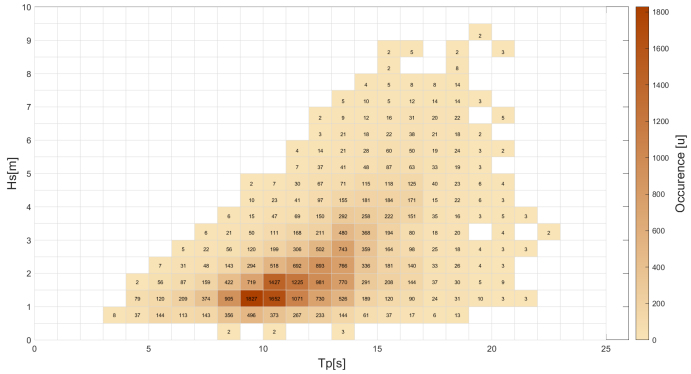

Figure 5.27: Example of an occurrence matrix computed at location DL01 from Figure 5.24

is the most offshore of the breakwater and the point DN15, the most nearshore one (Figure 5.24). The points are approximately 40m distant from each other. We observe that the production varies significantly along the breakwater. Between a WEC positioned at points DN05 and DN06, we observe a decrease of the production of around 12,8%, which gives an average decrease rate of 0.3% / m. It is however noted that further studies are required to confirm the precision of the model at this scale, in order to properly estimate these small-scale variations. If we make the assumption that a 10% variation between two locations is significant in the selection of the location of the WEC, a proper localization study for a WEC should be carried out at a scale of around 30m. However most of the studies assessing the wave energy potential such as [Iglesias and Carballo 2010]; [Vicinanza, Contestabile, and Ferrante 2013] use quite coarse grid of few hundreds of meters thus making impossible to accurately estimate the production of a WEC.

Generally speaking, it makes sense to install the devices in the offshore where the energy is usually the highest. However, we have shown in Chapter 4 that focusing effects may create energy

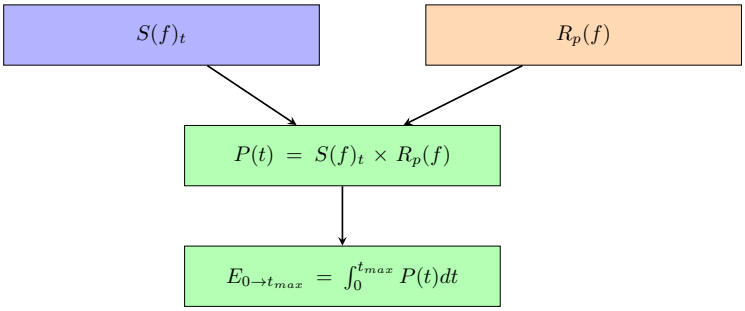

Figure 5.28: Method 1 : Computation of the total wave energy produced with a spectral transfer function. The green boxes corresponds to computed parts, the red boxes to data from literature and blue boxes to data from our model.

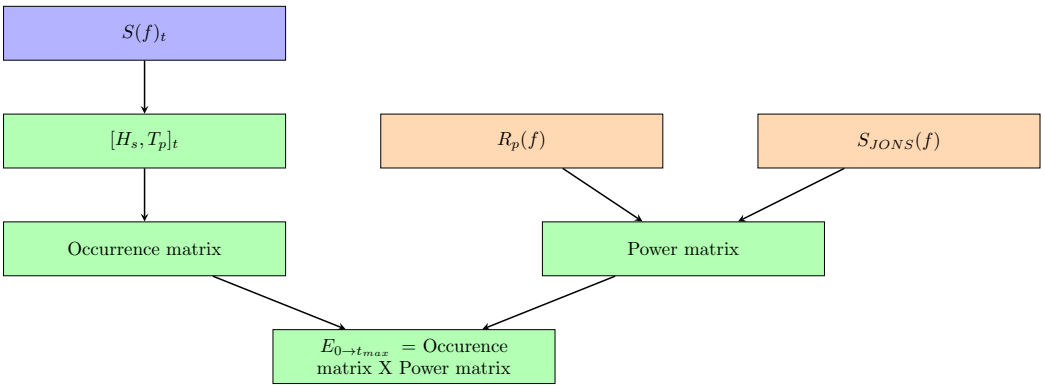

Figure 5.29: Method 2 : Computation of the total wave energy produced with a power matrix. The green boxes corresponds to computed parts, the red boxes to data from literature and blue boxes to data from our model..

hotspots closer to the shore. To verify whether this focusing effects exists in the area of the Bayonne breakwater, we compare the production along the breakwater (DN01-DN15) and the production at the two points located right offshore (DL02-DL03). The mean annual production of a WEC located in DL02 and DL 03 is equal to 0.78 GWh and 0.83 GWh, respectively. Depending on the location on the breakwater that we consider, the energy produced is either higher offshore (DN06, DN07, DN08 and DN10), similar (DN02, DN09 and DN15), or higher near the breakwater (DN01, DN03, DN04, DN05, DN 11, DN12, DN13 and DN14). These variations are probably caused by focusing effects that tend to reduce the production at certain spots and to increase it at others. Again, this illustrates the need for high-resolution hindcasts when assessing the suitability of an area with respect to WEC installation.

The temporal variability of the energy output is also a key aspect of any wave energy project. Figure 5.31 shows the evolution of the annual energy production for each location along the Bayonne breakwater over 10 years. The energy production can vary a lot between two consecutive years (up to 25 %). This strong inter-annual variability was already shown in Chapter 4. Over the period

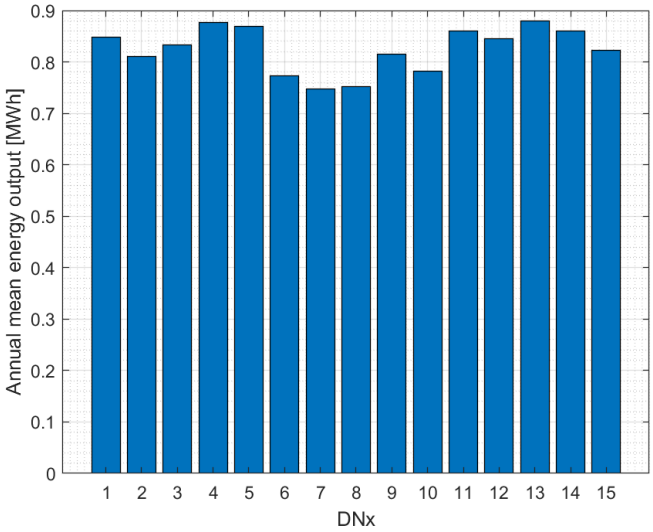

Figure 5.30: Mean annual production over 10 year computed with the spectral transfer function at each DN x location presented in Figure 5.24

2000-2010, the annual maximal production is 0,92 MWh (DN13 in 2003) and the minimal production is 0,52 MWh (DN07 in 2006).

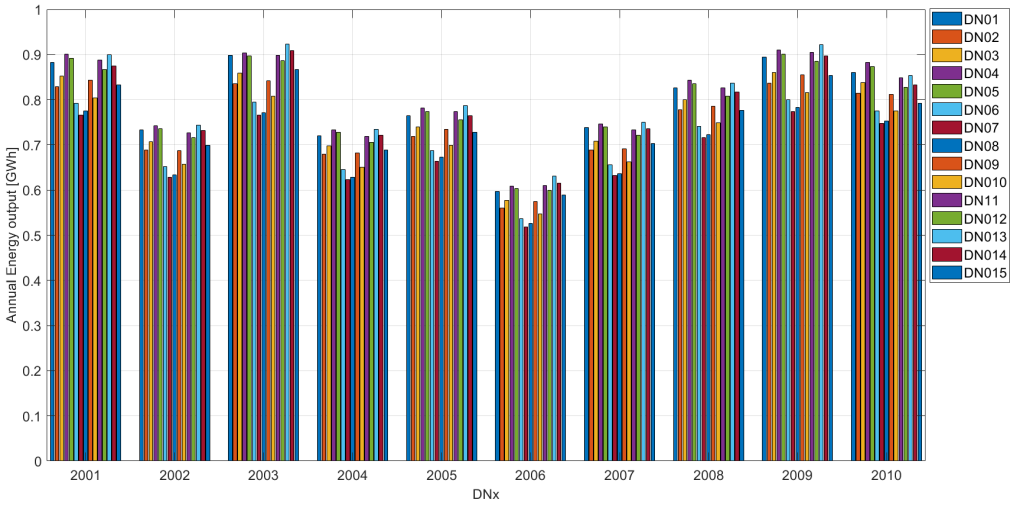

Figure 5.31: Annual productions over 10 year computed with the spectral transfer function at each DNx location presented in Figure 5.24

Influence of the spectral distribution of wave energy on WEC production estimates

As explained in Chapter 3, most of the wave energy assessment studies mostly focus on studying the statistical bulk parameters used to characterize a sea state (e.g. H_S, T_e). However in order to estimate as accurately as possible the resource, a more detailed description of the spectral content of the sea state might be useful. A specific investigation is then carried out about the role of the influence of the spectral distribution on the prediction of energy production by a WEC. The figure 5.32 shows the mean annual energy produced by the WEC along the breakwater computed with the power matrix of Figure 5.26. The evolution of the produced energy along the breakwater is similar to the one shown in Figure 5.30. We also observe the peak values at the same locations (*i.e.* DN04 and DN13) and approximately the same maximal evolution rate between DN05 and DN06 (9,8%). However the values are much lower than the ones computed with the spectral transfer function.

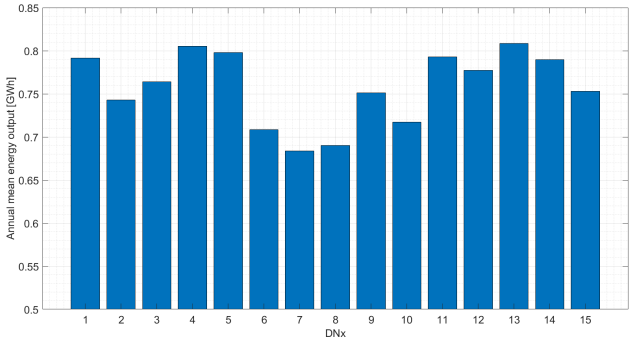

Figure 5.32: Annual mean production over 10 year computed with the power matrix

As stated in the paragraph above, although the shape of the evolution of the annual mean production of energy along the breakwater looks similar whether it has been computed with the spectral transfer function or the power matrix, the absolute values are quite different. We can see in Figure 5.33 that in fact, the estimates in energy production between the two computation methods varies between 90 and 99%, representing absolute values around 400MWh per year.

This difference may be due to the fact that real sea spectra might be multi-modal and thus have various H_s and T_p. In Figure 5.34, a forcing spectra from the BOBWA database is compared to a JONSWAP spectra with the same bulk parameters. We observe that although the two spectra are supposed to represent the same sea state, the BOBWA forcing spectra, which is considered to be the real spectra, has indeed multi-modal components that may affect the estimation of the energy output of a WEC. Then it appears that the first uncertainty in the computation of the energy output with a power matrix is the nature of the power matrix itself. Indeed, since an hypothesis on the shape of the spectra has to be made for its construction, a power matrix can not handle varying spectral shapes.

Another source of uncertainty lies in the fact that by construction, the occurrence matrix is a discrete function. Indeed, when estimating occurrence numbers for each $[H_s, T_p]$ duets, the bulk parameters of each sea-states have to be rounded to their closest values present in the occurrence matrix. Given that the output power is not strictly linear with the increase in H_s and T_p, the rounding process necessary to build the occurrence matrix may induce errors in the estimation of

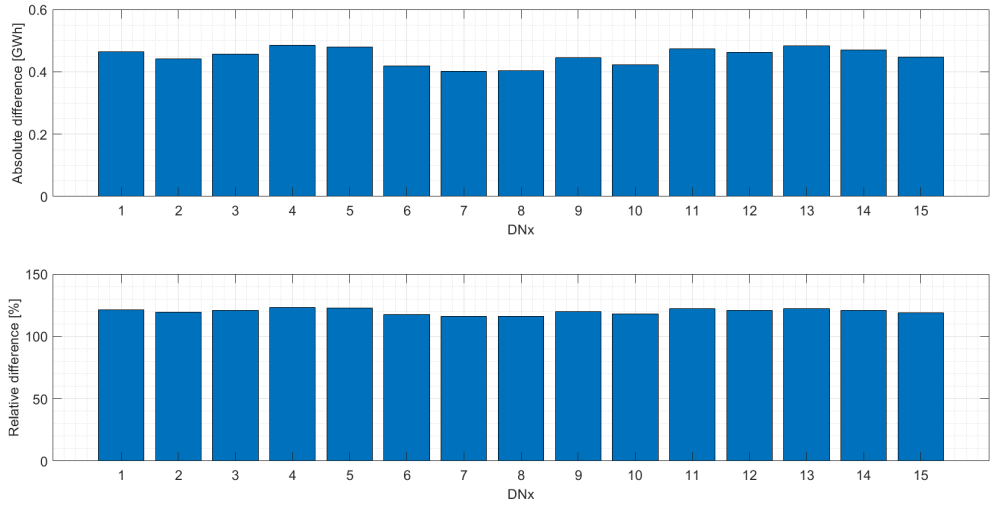

Figure 5.33: Absolute and relative difference between annual mean energy output computed with the spectral transfer function and the power matrix

the extracted power of the WEC.

5.3 Conclusion

This Chapter investigates the origin of the wave energy distribution over the domain studied in Chapter 4. First, a parametric study on the offshore boundary condition investigated the influence of incident H_S, T_p and wave direction values on the nearshore wave distribution. The very strong influence of the wave period was especially highlighted. In Chapter 4, the role of the submarine canyon was mentioned as the reason of the North/South gradient observed. To verify this hypothesis, an artificially homogenized bathymetry was created without the presence of the gouf. This new bathymetry allowed to conclude on the local role of the submarine canyon on the variability. However, it also suggested that the origin of the North/South gradient of energy across the domain is to be searched more offshore than our initial domain limits. To further determine this origin, a larger domain was created to investigate further the cause of the gradient. Again, refraction was identified as the main driver of the variability over the domain. In fact, the refraction over the continental slope seems to be the cause of the North/South gradient aforementioned. This refraction affects particularly the longest waves, which are also the most energetic ones. In Chapter 4, a high intra-annual variability was shown (see Figure 4.7), with higher levels of variability in winter. This higher variability, and consequently the mean wave energy flux, appears to be fueled by the refraction effect of long waves occurring in winter. It has to be noted that in addition to the reason mentioned here, the gradient may be fueled by a sheltering effect of western swells cause by the Iberian peninsula. This aspect is not studied in the present manuscript and would benefit from further investigations.

The influence of the wave energy distribution on WEC production estimates was also studied in

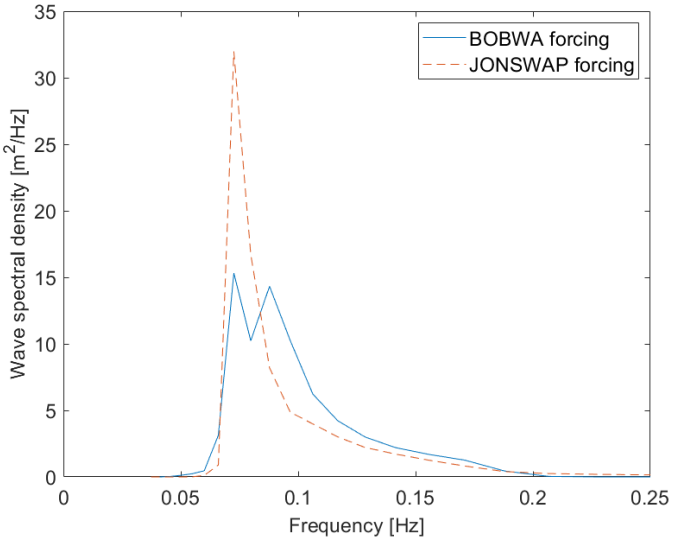

Figure 5.34: Comparison of forcing spectra taken from the BOBWA database (in blue) and corresponding JONSWAP spectra (in red)

this chapter. High spatio-temporal variability was highlighted at small scale, with spatial variations up to 12.8 % for two points 40m apart, or with variations up to 25% for two consecutive years. Then, two computation methods were compared, one using a spectral transfer function and the other one using a power matrix. The difference in energy output for the two computation methods was around 100%. This difference was expected to be caused by the nature of the power matrix which considers a single spectral shape, and/or during the computation of the occurrence matrix (i.e. rounding of the bulk parameters). This result emphasizes the added value of using the full spectral information, instead of limiting it to bulk parameters when predicting the energy production by a WEC.

Chapter 6

Spatial distribution of the impact load on a generic WEC

After studying the spatio-temporal variability of the resource, this chapter will focus on the spatial variability of the forcing acting on a generic WEC. Depending on their magnitude, loads can affect the operation of the WEC and even permanently harm the devices. Therefore, it is essential to understand the mechanism of loading. Two types of loading can affect WECs : slamming loads and quasi-static loads inducing fatigue. Those two types of loading do not occur at the same time-scale but are both to be considered for design purposes. Slamming events will induce extreme loads over very short period of times (i.e. magnitude of seconds) while quasi-static loads will have much lower levels but will be applied almost consistently over the lifetime of the WEC. However, given the short lifetime of the WEC devices that were placed in the ocean (e.g. the WaveDragon prototype survived only 2 years [Christensen 2005]), we decided to focus on what seemed the priority. Therefore, only the impact loads will be studied in this manuscript.

Wave impact on WECs can take many forms, including overtopping and slamming. Overtopping occurs when waves are higher than the WEC's crest level, causing water to flow over the device and potentially causing damage to the structure and mechanical components. Slamming happens when a breaking wave comes into contact with a solid object (e.g. a WEC), which can cause damage to the device and its mooring system. Resonant failure occurs when the natural frequency of the WEC's structure matches the frequency of the incoming waves, causing the device to vibrate excessively and potentially leading to structural failure.

The mechanisms by which wave impact causes damage and failure are complex and not fully understood. However, it is believed that wave impact can cause damage to the WEC's structure and mechanical components by applying high loads and strains, by causing fatigue and corrosion, and by inducing vibration and resonance ([Elhanafi et al. 2017], [Bliss 2020], [Kami Delivand and Murphy 2022]). To mitigate wave impact on WECs, a number of methods have been developed [Ambühl 2015], including structural optimization, active and passive control systems, and advanced materials and coatings. These methods can be used to improve the WEC's resistance to wave impact.

As a first attempt to estimate the maximal loads impacting a WEC over a given return period, the computation of a new design parameter, the Maximum Expected Slamming Force (MESF), is proposed. To that end, this chapter will provide a review of the literature on wave breaking, including estimation of extreme event and load computation. Additionally, this chapter will also

highlight current research gaps and future research directions in this field.

In order to be able to compute loads, a specific geometry has to be considered. As a a first step, a vertical cylinder of 5m diameter embedded at the sea bottom is chosen in the present study. The choice of this simple geometry allows to use formulations available in the literature, instead of using complex fluid dynamics related to floating and moored devices. As mentioned before, considering a cylinder simplifies the computation, although some WEC may have completely different geometries (e.g. Oscillating Water Columns), thus inducing different impact behaviours. For the same simplification purpose, the studied cylinder was considered embedded at the sea bottom. Regarding this hypothesis, if the WEC was considered to be floating, the magnitude of the impact loads applied to it is expected to be different. Indeed, floating devices will have different relative positions with respect to the breaking wave, thus modifying the impact mechanisms. Therefore the results presented in this manuscript may not be accurate, and the analysis of the respective influence of the aforementioned hypothesis are left for further studies.

The dimensions of the cylinder are similar to the generic WEC's presented in [Babarit et al. 2012], and therefore the loads computed with this structure are expected to reproduce the magnitude of the loads on a generic WEC. However, given that the chosen geometry is not the geometry of an actual WEC, the results provided here for the magnitude of the loads should not be used as design values. The results shown here allow to compare the breaking behaviours of extreme sea-states and to compare the spatial distributions of impact loads. The methodology proposed here can also be used to carry a similar analysis for offshore wind turbines installation where a compromise between wind resource available on site and risk induced by waves could be key.

6.1 Methodology

Usually, the wave loading is studied in detail at a specific location for specific waves [Poncet 2021], to obtain the most precise value of the load. Here, the approach differs in the sense that the spatial variability of the upper limits of expected loads is studied.

The objective of this section is to derive the value of the Maximal Expected Slamming Force (MESF) acting on a cylinder embedded in seafloor for a given return period. Slamming events, depending on the localization, can be either frequent or very rare. The rate of breaking waves depends on the local bathymetry but also on the wave conditions.

First, a formulation for the slamming load will be presented alongside the hypothesis that are made. Once the required parameters are identified, the methodology to compute them will be detailed. This will include computation of extreme sea states events through the so-called environmental contours and breaking wave height estimation. Then, the results will be presented and analyzed. Finally, the results will be discussed and conclusions drawn.

6.1.1 Slamming forces acting on a WEC

The objective of this section is to derive the value of the slamming force acting on a cylinder embedded in seafloor. Wave loading on structures has been extensively studied over the years. The first analytical formulations were derived by [Kármán 1929] and [Wagner 1932] from analyzing impact pressures on seaplanes during landing. A new factor, the curling factor λ, representing the height of the impact area in function of the incident wave height, was introduced later by [Goda, Haranaka, and Kitahata 1966]. Later, from experimental studies, [Tanimoto et al. 1987] observed

that the slamming load had a vertical triangular distribution over the impact area. All the slamming loads formulations are in the form of :

$$F_s(z,y,t) = \frac{1}{2}\rho V^2 \,.\, C_m \,.\, f(t) \,.\, \lambda.H_b.D \,.\, g(z,y) \tag{6.1.1}$$

With,

- $F_s(z,y,t)$: Slamming load [N]
- $\frac{1}{2}\rho V^2$: Dynamic pressure [Pa]
- C_m : Added mass coefficient [/]
- $f(t)$: Temporal development [/]
- D : Diameter of the cylinder [m]
- H_b : Breaking wave height [m]
- λ : Curling factor [/]
- $g(z,y)$: Spatial distribution [/]

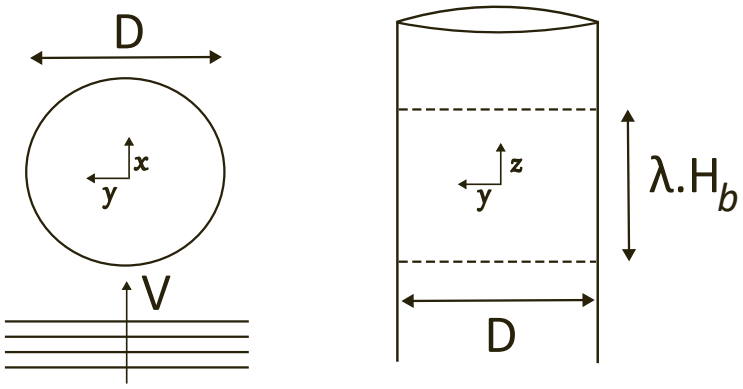

Figure 6.1: Sketch of the slamming load formulation

[Paulsen et al. 2019] derived a simplified form of equation 6.1.1 by making some hypothesis. First, regarding the added mass coefficient, which is depending on the wetted area of the cylinder, [Paulsen et al. 2019] made the assumption that the temporal variability of $F_s(z,y,t)$ was fully governed by an independent function $f(t)$. Therefore, the added mass coefficient C_m is considered constant and equal to 2π as first derived by [Wagner 1932] and later also used by [Goda, Haranaka, and Kitahata 1966] and [Wienke and Oumeraci 2005]. The temporal variation is taken in [Paulsen et al. 2019] as a sinusoidal function. Focusing on the maximal impact load, $f(t)$ will be taken equal to 1. Finally, measurements made in lab by [Paulsen et al. 2019] suggest that the curling factor should be taken such as :

$$\lambda = 0.29\frac{H_B}{H_s} \tag{6.1.2}$$

This leads to the following expression :

$$F_{s_{max}} = \rho \, . \, V^2 \, . \, 0.29 \frac{{H_B}^2}{H_s} \, . \, \frac{2D}{\pi} \tag{6.1.3}$$

In order to be able to compute equation 6.1.3, additional hypothesis and computations are required to estimate the particle velocity at the crest V and the breaking wave height H_B. Laboratory experiments carried out by [Paulsen et al. 2019] show that approximating the particle velocity in the crest of a breaking wave by the wave celerity $\sqrt{gh}$ gives conservative results for shallow to intermediate water depths (i.e. $kh < 2$). Further offshore, experimental results from [Lim et al. 2015] showed that the maximal horizontal velocity is close to $1.3C_p$, with C_p the phase speed of the wave computed with the linear wave theory. However, [Paulsen et al. 2019] measured horizontal velocities around C_p for kh=2.5. Therefore, in order to avoid applying a sharp frontier over the domain, we choose to approximate the horizontal velocities by the phase speed everywhere in the domain. Given that the considered waves are irregular, the phase speed will be computed through the spectral mean values of the wavelength and the period (i.e. $C_p = \frac{L_{m01}}{T_E}$). We then have :

$$V = \frac{L_{m01}}{T_E} \tag{6.1.4}$$

The computation of the significant wave height H_s and breaking wave height H_b for given return periods need additional statistical tools and modeling, therefore the following subsections will focus on detailing those methodologies.

6.1.2 Estimating the long-term extreme sea states : environmental contours

Although the hindcast data provided in Chapter 4 covers almost half a century, it can not be used as such to analyze the long term distribution of waves. Indeed, since sea-states associated with the 50-year and 100-year return periods are usually used to design WECs [DNV 2010], this would mean that over our data set such sea-states may appear once or even not appear at all. To overcome this issue, a popular approach is the use of environmental contours. Environmental contours [S. Haver and Kleiven 2004] define iso-values of non-exceeding probabilities for different sea-states. They are based on past measurements or hindcast data to fit probabilistic models that can infer long-term behaviour of sea-states, allowing to determine the sea states associated with the required return periods.

An example of the data used in this section is plotted in fig 6.2 for one point of the domain. It represents the hindcast data of a point off the Bayonne breakwater over 44 years with 3-hour time step from [Lastiri et al. 2020]. This represents a total of 135 307 $[H_s, T_p]$ duets.

Joint probability distribution

The first step to build environmental contours is the modelling of the joint probability distribution of the sea-state's bulk parameters. In this work the joint distribution of H_s and T_E is studied, which is the probability distribution for all $[H_s, T_E]$ duet. There are two types of probabilistic models : parametric and non parametric. This work will focus on hierarchical conditional models [Winterstein et al. 1993], where the density function of H_s is multiplied by the density function of H_s given T_E (noted as $T_E|H_s$)[DNV 2010].

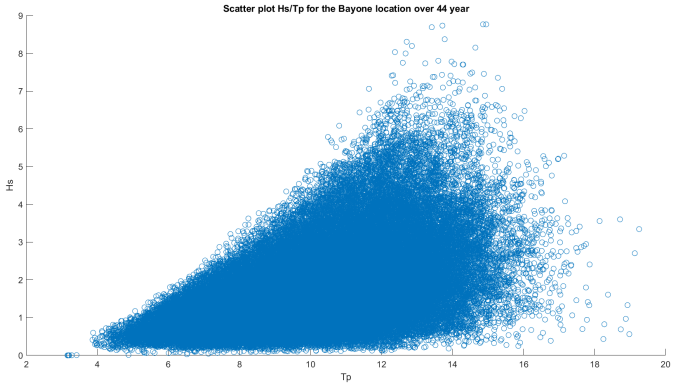

Figure 6.2: Scatter plot of H_s vs T_p at Bayonne location

The joint probability density function of H_s and T_E is then given by :

$$f_{Hs,T_E}(hs,t_E) = f_{H_s}(hs) f_{T_E|H_s}(t_E|H_s) \tag{6.1.5}$$

With, f_{H_s} the probability density function of H_s and $f_{T_E|H_S}$ the probability density function of T_E given H_s.

In the present work, the probability density function of H_s, noted $f_{H_s}(h_s)$, is modelled with a Weibull law :

$$f_{H_s}(h_s < H_s) = \frac{k}{c}\left(\frac{h_s}{c}\right)^{k-1} e^{-\left(\frac{h_s}{c}\right)^k} \tag{6.1.6}$$

The scale and location parameter of the Weibull law are estimated by fitting the probability law over the hindcast data. Two methods of fitting were tested here. The goodness of fit is presented in Figure 6.3 for the Weighted Least Square (WLSQ) method and in Figure 6.4 for the Maximum Likelihood Estimation (MLE) method. We observe that both the fitting methods produce similar results regarding the estimation of the mean wave period T_E. The model is in good agreement with the data for wave periods between 8 and 12s, however outside these values the results differ from the data. Regarding the significant wave height, the WLSQ fitting method provides better results (except from values for significant wave height higher than 8m) and will thus be chosen.

The next step is to compute the conditional distribution of T_E given H_s [Lian and S. K. Haver 2016]. The following formulation, establishes a relationship for the probability density function on T_E with a condition on the significant wave period H_s :

$$f_{T_E|H_s}(T_E|H_s) = \frac{1}{T_E.\sigma\sqrt{2\pi}} e^{\left(-\frac{(ln(T_E)-\mu)^2}{2.\sigma^2}\right)} \tag{6.1.7}$$

With $\mu = E\left(ln(T_E|H_s\right)$ and $\sigma^2 = Var\left(ln(T_E)|H_s\right)$

The dependencies function on μ and σ are :

$$\mu = a_1 + a_2\left(H_s^{a_3}\right) \tag{6.1.8}$$

$$\sigma^2 = b_1 + b_2 exp(b_3 h_s) \tag{6.1.9}$$

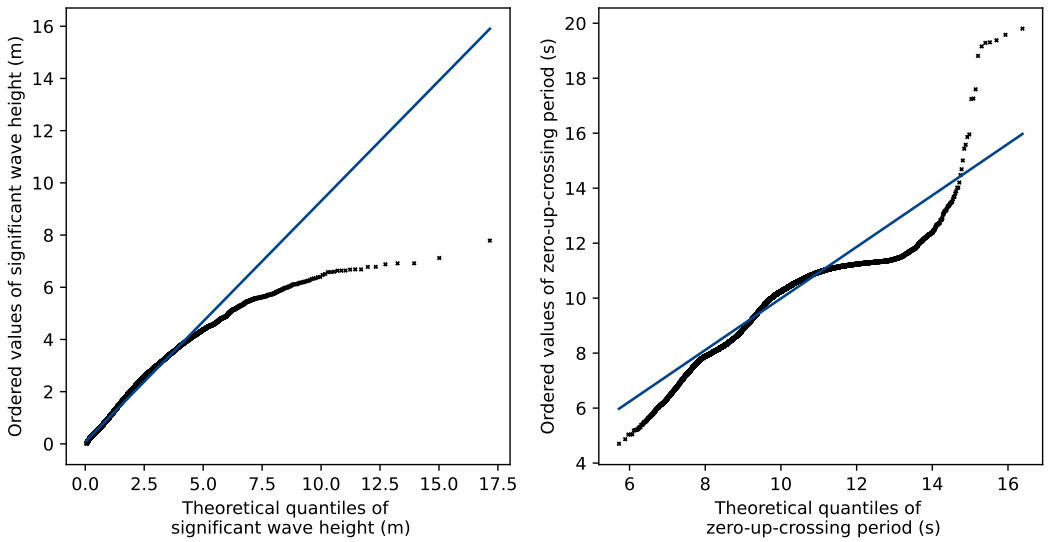

Figure 6.3: Quantile plot of H_s and T_E with the MLE fitting method

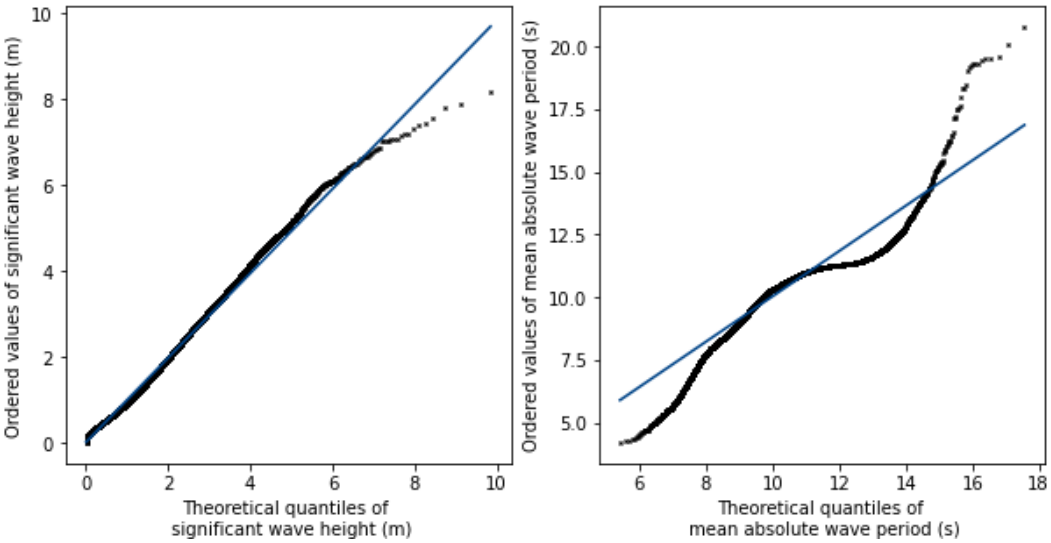

Figure 6.4: Quantile plot of H_s and T_E with the WLSQ fitting method

Environmental Contour Method

The classical way to compute environmental contours is through the Inverse First Order Reliability Method (IFORM) [Winterstein et al. 1993]. It consists in transforming the original environ-

mental parameters to standard normal variables through the so-called Rosenblatt transformation [Rosenblatt 1952], to be able to identify a circle in the standard normal space with a radius equal to the failure probability P_f (the return periods in our case). The points corresponding to this circle are then transformed back into the original space with the inverse Rosenblatt transformation. The main issue with classical IFORM transformation is that due to the Rosenblatt transformation between the physical and the standard normal spaces, the failure probabilities might be overestimated or underestimated [Bang Huseby, Vanem, and Natvig 2013]. An alternative method is the use of the Direct Sampling method. The Direct Sampling method consists in using Monte Carlo simulations of the joint environmental model described in the previous section to build the environmental contour directly in the original parameter space [Bang Huseby, Vanem, and Natvig 2013].

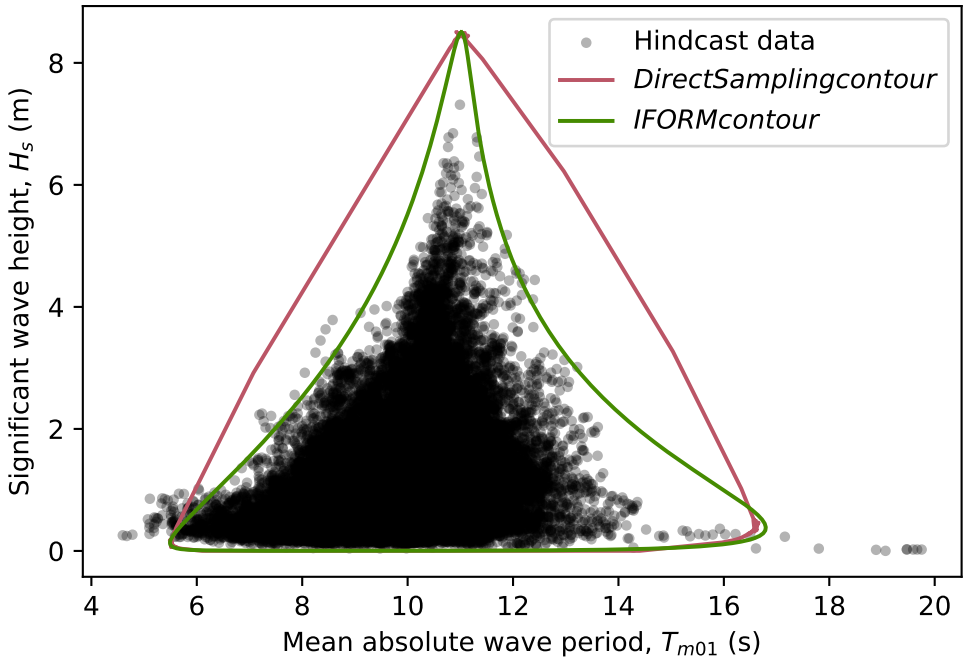

Figure 6.5: Environmental contours built with a 50 year return period with the Direct Sampling and IFORM methods

We observe in Figure 6.5, that both methods provide similar results regarding maximal values for H_s and T_E. However, the IFORM method provides results obviously closer to the observed values for intermediate values. Indeed, for $T_E = 8s$, the value of H_s read on the environmental contour computed with the Direct sampling method is two times higher than the value of H_s read on the environmental contour computed with the IFORM method. For, $T_E = 14s$ the value is three times higher. The same result was observed in various locations, representative of various water depths. Therefore, for this work, the IFORM method is preferred since it provides better results. It has to be noted that some data points of the 44 year hindcast appear outside the 50

year contour. Although counter-intuitive, this results was also observed in previous works related to environmental contours (e.g. [Haselsteiner et al. 2019]).

Given the large size of the computational domain, and given time constraint for the computation, a regular grid with a spatial resolution of 1 km was created using a nearest neighbour interpolation. This process was chosen so that the computations depict real sea states and to avoid averaging effect that could smooth eventual peak values.

6.1.3 Estimating spectral distribution with parametric shape

The methodology presented above allows to estimate $[H_s; T_E]$ duets associated with extreme events with a given return period. However, additional information is required to estimate the breaking wave height necessary to compute the maximal slamming force presented in equation 6.1.3. Namely, the wave spectra is necessary to compute the Breaking Wave Height Distribution (BWHD) that will be detailed in the next subsection.

At a given location, for each $[H_s; T_E]$ duet, we make the assumption that the sea state can be represented with a JONSWAP spectra. [Goda 2008] provided an approximate formulation of the JONSWAP spectra based on the statistical wave parameters $[H_s; T_p]$ and γ which is the peak enhancement factor a constant value :

$$S_{JONS}(f) = B_J.H_s^2.T_p^{-4}.f^{-5}exp(-1.25(T_p.f)^{-4})\gamma^{exp(-\frac{(T_p.f-1)^2}{2\sigma^2})} \tag{6.1.10}$$

$$\text{With, } \sigma = 0.07 \text{ if } f \leq f_p \text{ or } \sigma = 0.09 \text{ if } f \geq f_p \tag{6.1.11}$$

$$\text{And, } B_j \approx \frac{0.0624(1.094 - 0.01915 \times ln(\gamma)}{0.230 + 0.0336\gamma - 0.185(1.9 + \gamma)^{-}1} \tag{6.1.12}$$

In order to verify that the wave spectrum inside the computational domain could be modeled with a JONSWAP spectra, JONSWAP spectrum were fitted to the forcing spectra from the BOBWA database. Regarding the present study, the focus is made on the energetic events that are expected to reproduce larger events. For each forcing point, over each time step with $H_s > 5m$ the best peak enhancement factor γ is computed. Finally, a peak enhancement factor γ_{mean} is taken as the average of all the previously computed γ. An example of a fitted JONSWAP spectra for an energetic event ($H_s = 5m$, $T_p = 10s$) is presented in the left panel of Figure 6.6. We observe that the fitted JONSWAP spectra reproduces well the BOBWA forcing although some components (around 0.07Hz and 0.13Hz) are misrepresented. From these computations, the peak enhancement factor γ was found to be close to 1.2. These value seems to be in agreement with the results of [Mazzaretto 2022], although γ values up to 7 were reported for the study area. The author of the manuscript acknowledges that the used JONSWAP spectra is not able to reproduce accurately multi-modal sea states. Therefore further studies are required to quantify the occurrence of these sea states in order to properly model the wave spectra.

In Chapter 4, the influence of the wind was shown to be negligible for moderate winds up to 10 $m.s^{-1}$. However, we may expect stronger winds to affect the breaking behaviour of extreme sea states. Therefore, additional tests were carried out to verify this hypothesis for energetic events in presence of homogeneous strong winds of 15 $m.s^{-1}$ (winds corresponding to extreme storm events reported in [Rasilla et al. 2018]). Additional test cases were run with and without a homogeneous wind over the domain. The right panel of Figure 6.6 shows the results of the two simulations carried out. The first simulation was carried out with a homogeneous JONSWAP spectra along the borders of the domain and a second simulation was carried out with the same forcing but with a

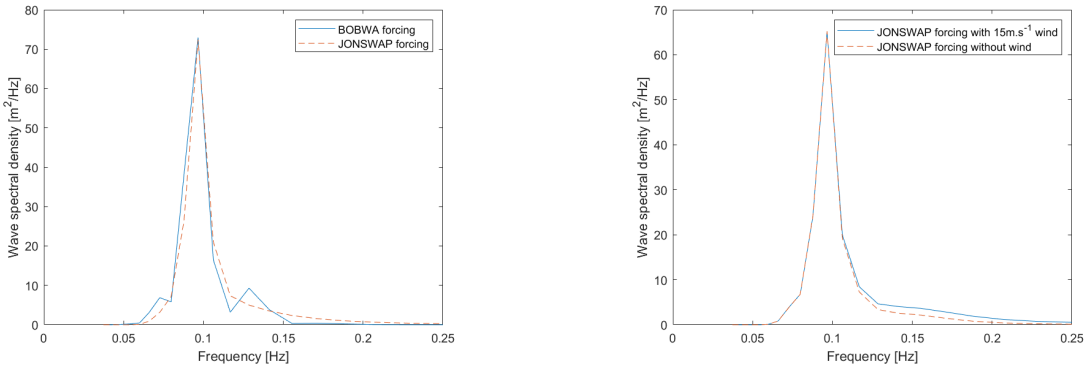

Figure 6.6: (left) Comparison of forcing spectra taken from the BOBWA database (in blue) and fitted JONSWAP spectra (in red) (right) Comparison of spectrum computed with a JONSWAP spectra forcing and an homogeneous 15 $m.s^{-1}$ wind (blue) and without wind (red)

homogeneous wind of $15m.s^{-1}$ over the domain. The right panel of Figure 6.6 shows the spectra for the two simulations taken at the same location (approximately 10km off the coast at 60m water depth). As could be expected, the wind increases the spectral components for high frequencies (i.e. higher than 0.13Hz), but the spectral component around the peak frequency f_p are not modified.

6.1.4 Estimating the breaking probability of a sea state

WECs may be installed in different water depths, ranging from onshore locations (e.g. on top of breakwaters), in shallow waters (e.g. flapping devices) or further offshore (e.g. heaving buoys). Wave breaking may occur at these locations due to too high wave steepness or the decrease of the water depth. This needs to be accounted for to evaluate the amount of risk of a local placement with respect to WEC survivability. Estimating the breaking probability of a sea-state (or fraction of breaking waves Q_B) equals to summing the breaking probability of all the wave heights ($\int_0^{+\infty} P_B(H)dH$). This reads as :

$$Q_B = \int_0^{+\infty} P_B(H)dH \tag{6.1.13}$$

Approaches looking for a deterministic threshold for random wave succeeded only at establishing a threshold for spectral density [Banner, Babanin, and Young 2000]. So far, only a probabilistic threshold could be derived, where breaking consists in assigning a breaking probability to each wave height component.

$$P_B(H) = P(H).W(H) \tag{6.1.14}$$

The objective of this subsection is therefore to compute the wave height distribution of a sea state $P(H)$ and assigning the corresponding weight function $W(H)$.

Physically, wave start breaking when the velocity of the wave particles u_c at the crest exceed the wave phase speed C (i.e. $\alpha = \frac{u_c}{C} > 1$). However, some waves may break before reaching a value of $\alpha = 1$ because of their instability [Stansell and MacFarlane 2002]. For one-dimensional, periodic,

irrotational waves over a flat bottom [Miche 1944] showed that α can be written in the following form :

$$\alpha = \frac{kH_{max}}{\beta_{max} tanh(kh)} \tag{6.1.15}$$

with, k the wave number, H_{max} the maximum wave height, h the water depth and β_{max} a constant equal to 0.88. From there, studies based on shallow water theory derived a breaking threshold dependent on the water depth [J. A. Battjes 1972] in the form :

$$H_{max} = \overline{\gamma} h \tag{6.1.16}$$

with $\overline{\gamma}$, an empiric constant value. This formulation means that the waves smaller than H_{max} are not breaking while the other waves are limited to H_{max} and are breaking [J. Battjes and Janssen 1978]. In terms of breaking weight function W, this leads to :

$$W_{BJ}(H) = \begin{cases} 0 & \text{if } H < H_{max} \\ 1 & \text{if } H = H_{max} \end{cases} \tag{6.1.17}$$

[Thornton and Guza 1983] proposed a refined approach where the Breaking Wave Height Distribution (BWHD) depends on $\overline{\gamma} = H_{RMS}/h$. It has to be noted that although $\overline{\gamma}$ is similar to the parameter expressed in 6.1.16, the approach is different in the sense that the weight function does not apply a strict on/off switch for wave breaking and allows waves to be higher than H_{max} before breaking. The computation consists in computing the BWHD $P_B(H)$ based on the Rayleigh distribution $P_R(H)$ and W_{TG}, a weight function associated to wave breaking :

$$P_B(H) = P_R(H) \times W_{TG} \tag{6.1.18}$$

The Rayleigh distribution of the wave heights is :

$$P_R = \frac{2H}{(H_{rms})^2} exp(-(\frac{H}{H_{rms}})^2 \tag{6.1.19}$$

In shallow waters, the shape of the weight function associated to wave breaking as computed in [Thornton and Guza 1983] is :

$$W_{TG} = \left(\frac{\gamma_{RMS}}{\tilde{\gamma}}\right)^2 \left(1 - exp\left[-(\frac{\gamma}{\tilde{\gamma}})^2\right]\right) \tag{6.1.20}$$

With, $\gamma_{RMS} = \frac{H_{RMS}}{h}$, and $\gamma = \frac{H}{h}$ and $\tilde{\gamma} = 0,88$ according to [Miche 1944].

Since the formulation developed by [Thornton and Guza 1983] is valid only in shallow waters, it cannot be used to compute the breaking wave height H_B over the whole computational domain studied in this manuscript, since it contains also intermediate and deep waters. More recently, the formulation of [Thornton and Guza 1983] was extended in intermediate and deep water by [Filipot, Ardhuin, and Babanin 2010]. Their intention was to provide a unified parametrization for the dissipation source term related to breaking in shallow, intermediate and deep waters. They introduced the use of wave scales as presented by [Banner, Babanin, and Young 2000]. The wave scales define spectral windows centered at frequency f_i that describe the components of random sea states (an example of a spectrum decomposed into 4 wave scales is given in Figure 6.7). The separation in wave scales allows the use of the formulation presented in equation 6.1.20 for different

frequency ranges. For each wave scales, representative values can be computed (e.g. H_{repr} the representative wave height or k_{repr} the representative wave number). The breaking probability at a given wave scale f_i noted $P_B(H, f_i)$ is then given by :

$$P_B(H, f_i) = P_R(H, f_i) \times W_{FAB}(H, f_i) \tag{6.1.21}$$

With, $P_R(H, f_i)$ the Rayleigh distribution of wave height for the wave scale f_i, and $W_{FAB}(H, f_i)$ the weight function associated with breaking for the wave scale f_i, as computed by [Filipot, Ardhuin, and Babanin 2010].

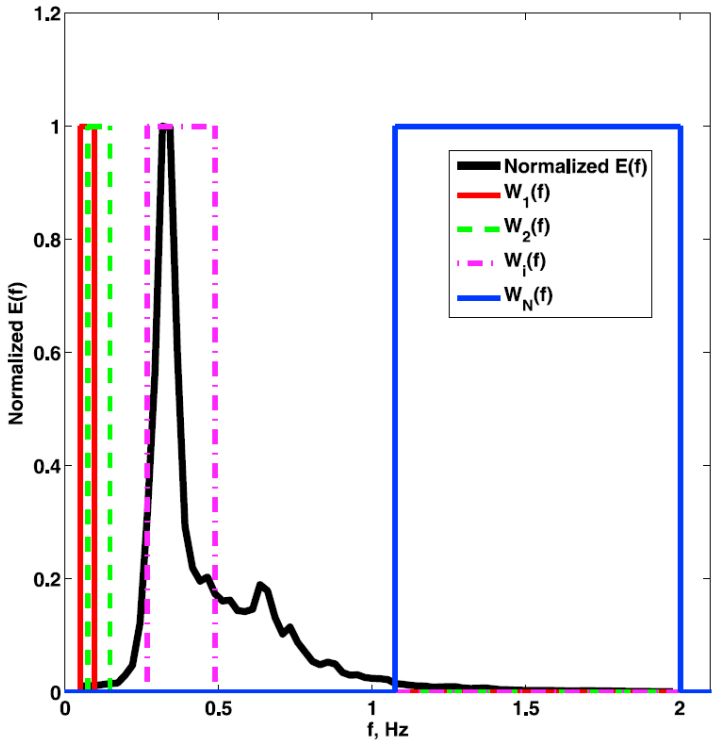

Figure 6.7: Waves scales as presented in [Filipot, Ardhuin, and Babanin 2010]

The Rayleigh distribution of the wave height at a given frequency f_i is :

$$P_r(H, f_i) = \frac{2H}{(H_{repr}(f_i))^2} exp(-(\frac{H}{H_{repr}(f_i)})^2 \tag{6.1.22}$$

With, H_{repr} at a given frequency f_i calculated as

$$H_{repr}(f_i) = \frac{4}{\sqrt{2}} \int_{0.7f_i}^{1.3f_i} S(f_i) df \tag{6.1.23}$$

And,

$$T_{E_{repr}}(f_i) = \frac{\int_{0.7f_i}^{1.3f_i} \frac{S(f_i)df}{f}}{\int_{0.7f_i}^{1.3f_i} S(f_i)df} \tag{6.1.24}$$

In [Filipot, Ardhuin, and Babanin 2010], the shape of the weight function associated to wave breaking for the wave scale centered at frequency f_i is generalized as :

$$W_{FAB}(H, f_i) = 1.5(\frac{\beta_{repr}}{\beta_{lin}})^2 \left(1 - exp(-(\frac{\beta}{\beta_{lin}})^4)\right) \tag{6.1.25}$$

Where,

$$\beta_{repr} = \frac{k_{repr}.H_{repr}}{tanh(\overline{k_{repr}}h)} \tag{6.1.26}$$

with,

$$k_{repr}(f_i) = \frac{\int_{0.7f_i}^{1.3f_i} k(f_i)S(f_i)df}{\int_{0.7f_i}^{1.3f_i} S(f_i)df} \tag{6.1.27}$$

β_{lin} is the linearized breaking onset which is assumed to be linearly correlated to the maximal breaking onset $\beta_{max,lin}$. We then have :

$$\beta_{lin} = b \times \beta_{max,lin} \tag{6.1.28}$$

In [Thornton and Guza 1983], the waves were not filtered into different wave scales. Given that filtering linearizes the waves, their work corresponds to the use of the maximal given by [Miche 1944] (i.e. $\beta_{max} = 0.88$). However, in [Filipot, Ardhuin, and Babanin 2010], due to the filtering of the waves, the breaking criterion needs adjusting since the linearization might induce underestimation of the wave heights. They provided a polynomial fit of $\beta_{max,lin}$ as a function of tanh(kh):

$$\beta_{max,lin} = 1.0314(tanh(kh)^3 - 1.9958(tanh(kh)^2 + 1.5522(tanh(kh) + 0.1885 \tag{6.1.29}$$

Using the recordings carried out in Lake George, Asutralia, [Filipot, Ardhuin, and Babanin 2010] estimated the constant b from equation 6.1.28 to be equal to 0.48 which is consistent with the value from [Miche 1944].

From equation 6.1.21, it is now possible to compute the fraction of breaking wave for this wave scale :

$$Q_{Bi}(f_i) = \int_0^{+\infty} P_B(H, f_i)dH \tag{6.1.30}$$

With the time step for the wave hindcast presented in Chapter 4 equal to 3 hours, the mean spectral wave period T in s and Q_B the fraction of breaking waves, the number of breaking waves in a single time step is :

$$n = \frac{3h \times 3600}{T} \times Q_B \tag{6.1.31}$$

To consider that a sea state is breaking, we arbitrarily assume that at least one wave must break (i.e. n must be greater or equal to 1), which leads to :

$$Q_{B,lim}(f_i) = \frac{T_{E_{repr}}(f_i)}{10800} \tag{6.1.32}$$

In order to consider that a given 3h stationary sea state is breaking, the fraction of breaking wave Q_B must be higher than $Q_{B,lim}$. However, given the stochastic nature of wave breaking and considering that breaking occurs at one precise location, $Q_{B,lim}$ might be over conservative. Indeed, since the focus is made on impact loads on WECs, the breaking has to occur at the exact location of the WEC. Therefore multiple values of Q_B higher than $Q_{B,lim}$ will be tested further.

6.1.5 Estimating the significant breaking wave height

In the previous section 6.1.4, a methodology to compute the breaking probability and the BWHD for a wave scale was presented. However, the wave height distribution 6.1.22 only accounts for a portion of the spectrum centered around f_i. To compute the significant wave height of the actual waves breaking on a WEC, the full spectra should be accounted for.

For a given irregular sea state, breaking waves can have different heights. Therefore, we propose the introduction of the Significant Breaking Wave Height (SBWH) similar to the significant wave height H_S called H_{Bs}. It means that a third of the breaking waves will have a height greater than H_{Bs}. For the different wave scales, it is computed as :

$$\int_{H_{BS_i}}^{+\infty} P_B(H, f_i) dH = \frac{1}{3} Q_{B_i} \tag{6.1.33}$$

Then, for each wave scale i, the spectral moment m_{0b_i} associated with the significant breaking wave height is computed.

$$m_{0b_i} = \frac{H_{BS_i}}{16} \tag{6.1.34}$$

Finally, for a decomposition in n wave scales, the total significant breaking wave height is computed :

$$H_{BS} = 4\sqrt{\sum_{i=1}^{n} m_{0b_i}} \tag{6.1.35}$$

One flaw of this previous equation lies in the assumption that the energy associated with each wave scale is linearly summed to obtain the total energy of the breaking waves. Further work assessing the influence of each wave scale on the breaking behaviour is expected to provide more refined results. Another uncertainty that is yet to be accounted for is the fact that the SBWH represents a mean value for the highest breaking waves, as opposed to the more commonly used breaking wave height definition which is the height of an individual wave that is breaking.

6.1.6 Selection of the design sea state

The last step consists in selecting the most critical sea states characterized by a $(H_s; T_E)$ duet. The environmental contour method presented in 6.1.2 provides 72 $(H_s; T_E)$ duets at each location of the computational domain. Each of this duets represent a sea state that should appear once over the chosen return period. Following the methodology presented above, it is possible to compute the slamming force $F_{s_{max}}$ (eq. 6.1.3) for each duet along the environmental contour. Finally, the design sea state is defined as the $(H_s; T_E)$ duet with the highest $F_{s_{max}}$.

Although the proposed methodology here is expected to provide reasonable results, it works on the assumption that the MESF for a given return period is associated with a sea state (defined by

a $(H_s; T_E)$ duet) with the same return period. Alternative approaches looking at defining return periods in terms of spectral parameters may thus allow to estimate more accurately the maximal expected slamming force.

6.1.7 Summary of the computation for one point of the domain

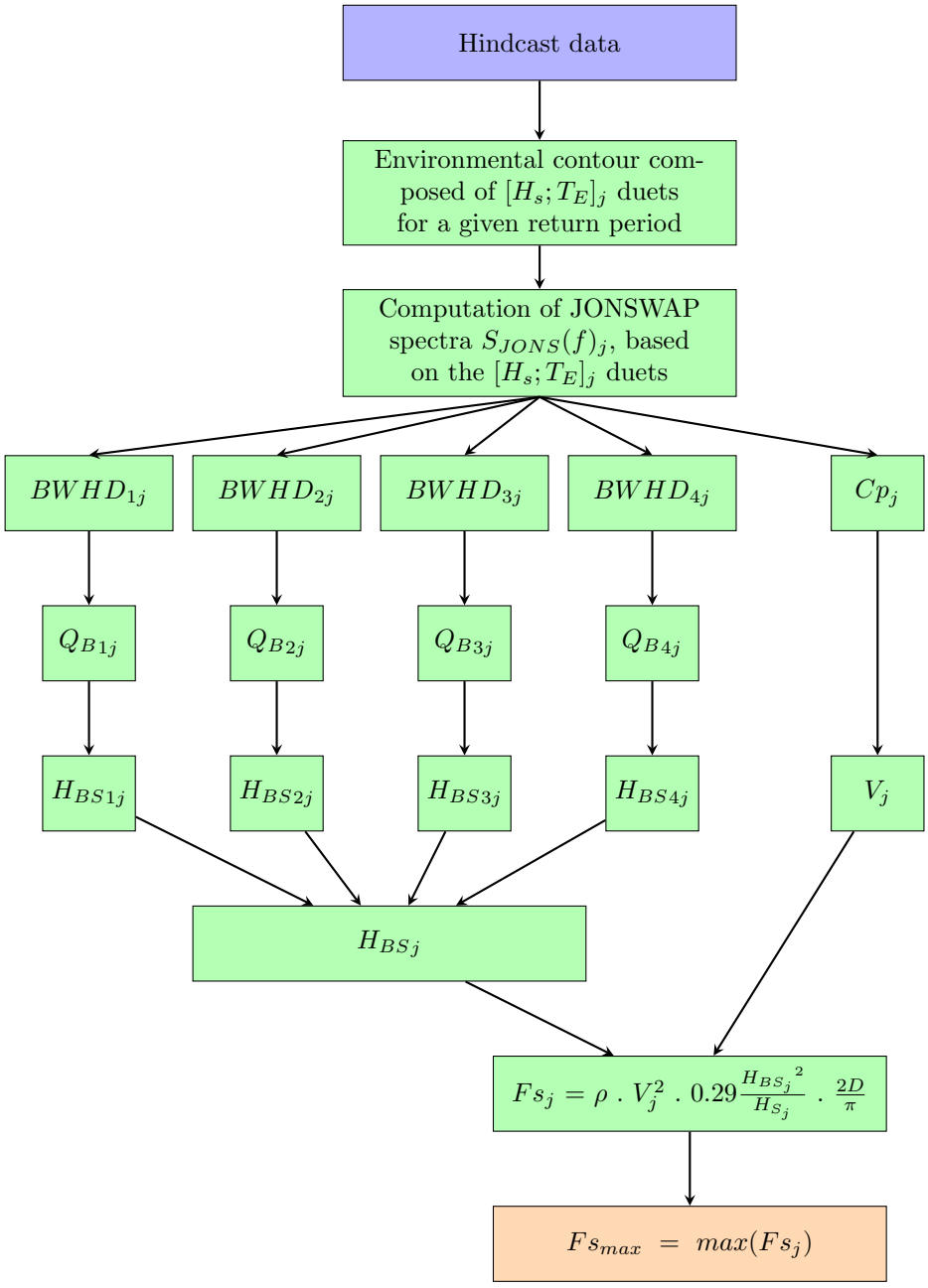

6.2 Results

6.2.1 Variability of the breaking probabilities

The division of the spectra in wave scales implies that the breaking behaviour of all the wave scales should be studied separately. Therefore, the computational model was forced with an homogeneous JONSWAP spectra ($H_s = 8$, $T_p = 11$). The Figure 6.8 shows the fraction of breaking waves Q_b computed at each location for each wave scale. We observe that the wave scale centered at the peak frequency f_p tends to break the most while the wave scale centered at 1,86 f_p also contains breaking waves. However, the wave scales centered at 0,55 f_p and 3,45 f_p do not contain breaking waves. The fact that the shortest waves (i.e. the wave scale centered at 3,45 f_p) do not contain breaking waves seems unlikely. This unrealistic result is caused by the fact that the BOBWA spectra is not refined enough at higher frequencies (the cut-off frequency is 0.25Hz). Therefore, with an approximate value of f_p around 0.1 Hz, it appears that the wave scale centered at 3,45 f_p will not contain any wave energy, thus resulting in an absence of breaking wave. Overall, since most of the breaking waves are contained in the wave scale centered at f_p, the breaking behaviour of this wave scale will be further studied.

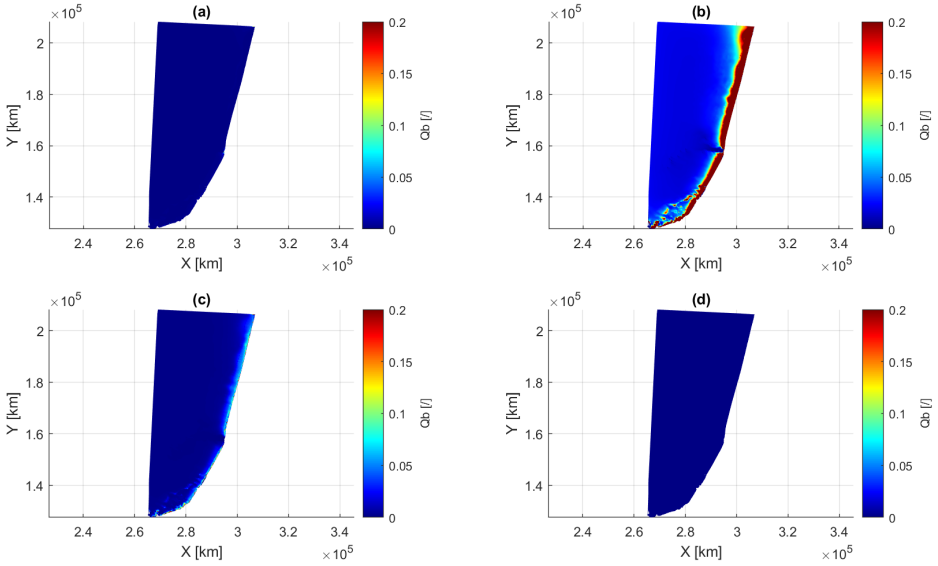

Figure 6.8: Fraction of breaking waves Q_b computed for the the different wave scale centered at (a) f_i= 0,55 f_p (b) f_i= 1 f_p (c) f_i= 1,86 f_p (d) f_i= 3,45 f_p

As explained in section 6.1.4, considering that a sea state is breaking if it contains one breaking wave might be over-conservative when considering wave impact on a WEC. Indeed, considering such a breaking threshold would mean that on average, over a 3 hour sea-state, one wave is breaking. But conversely, that would also mean that it is possible to observe no breaking wave over 3hour sea states. Additionally even if a wave would break it would have to break exactly over the WEC in order to create an impact. To understand better the evolution of the fraction of breaking waves

Q_b, the domain was forced with a series of homogeneous JONSWAP spectra. Then the fraction of breaking waves Q_b for the wave scale centered at f_p was computed at each location for the corresponding incident sea state (see Figure 6.9). Using homogeneous forcing will allow to observe the breaking behaviour over the area, with controlled wave conditions at the borders.

As could be expected, we observe that when the significant height of the wave forcing is increased, the fraction of the breaking waves tends to increase. Close to the shore, the values of Q_B are higher than 0.5 but rapidly decreases when going further offshore. We also observe that in the southern part of the domain, higher levels of Q_B are observed around 5km from the shore compared to locations in the northern part at the same distance from the coast. This effect can be explained by the irregular rocky bathymetry of the bask coast (Figure 6.10), where the highest waves might break over shallower area that can be found offshore (are located in the south-western part of the domain).

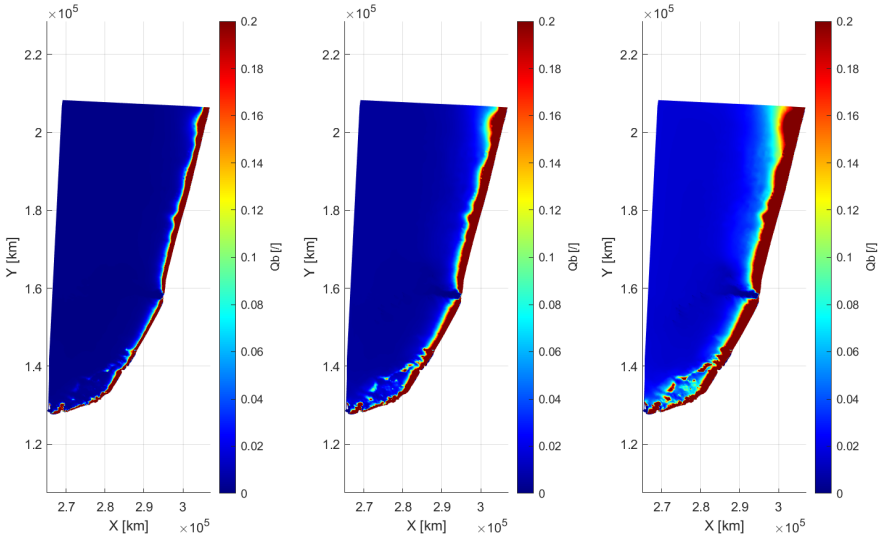

Figure 6.9: Fraction of breaking wave Q_B for different JONSWAP forcings : (left) $H_s = 5m$, $T_p = 11s$ (middle) $H_s = 8m$, $T_p = 11s$ (left) $H_s = 11m$, $T_p = 11s$

In order to assess more in detail this effect, the following figures present a Breaking Index for different forcing sea state. The Breaking Index applies a strict on/off switch if a certain value $Q_{B,lim}$ is reached. This means that if the Breaking Index is equal to 1, the sea state is considered to be breaking and if it is equal to 0 it means that there is no breaking waves. This approach allows to identify if a certain sea state is breaking or no at a certain location. In Figure 6.11, the threshold for $Q_{B,lim}$ was set to 10^{-3}. This means that for a 3h sea state with a mean period of 11s, one wave will be breaking. We observe that for a forcing wave height of 5m, breaking sea state appear in the coastal area (approximately up to 3km from the shore) with the exception of very localized spots off the bask coast as mentioned earlier. For a forcing wave height of 8m breaking sea state appear more offshore up to 6 to 7 km. When considering very extreme forcing wave height of 11m, breaking should occur over almost all the computational domain apart from the coastal area of the

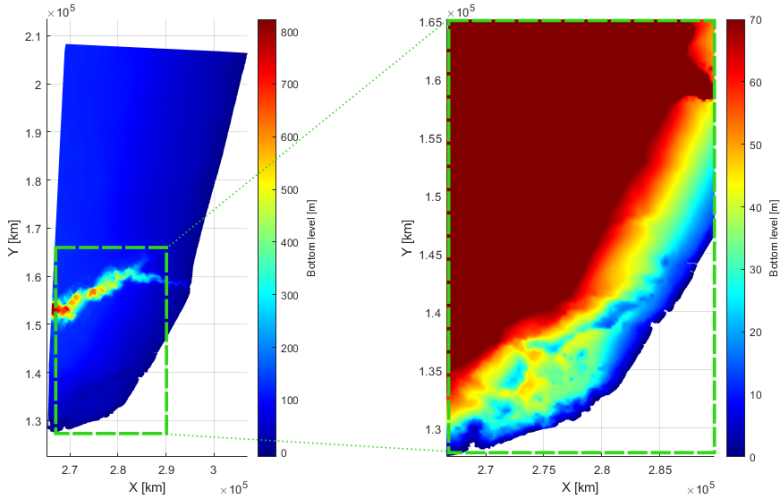

Figure 6.10: (left) Bathymetry of the domain and (right) zoom on the nearshore domain of the bask coast

submarine canyon of Capbreton.

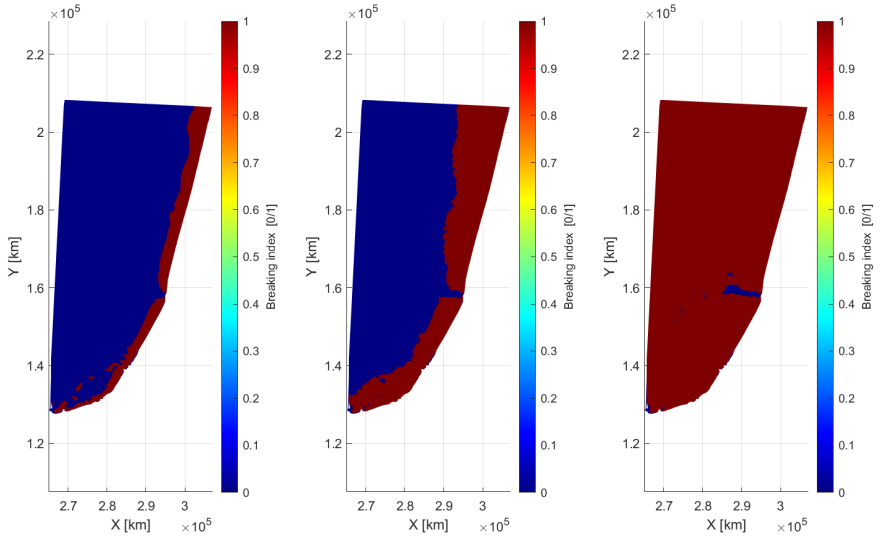

Figure 6.11: Breaking Index with a limit threshold of 10^{-3} for (left) $H_s = 5m$,$T_p = 11s$ (middle) $H_s = 8m$,$T_p = 11s$ (left) $H_s = 11m$,$T_p = 11s$

As mentioned before, a breaking threshold of 10^{-3} (i.e. only one wave is breaking for a given

sea-state of 3h) might be over-conservative when studying impact loads on a WEC (i.e. the breaking wave must break right on the WEC). Therefore other threshold values are studied in Figure 6.12 to identify areas where breaking can appear but to an acceptable level. It appears clearly that the very nearshore area is the most subject to wave breaking since for all the limit threshold studied these locations are considered to contain breaking waves. However some area where the Breaking Index is equal to 1 for $Q_{B,lim} = 10^{-3}$ but equal to 0 for $Q_{B,lim} = 5.10^{-2}$ are worth noticing.

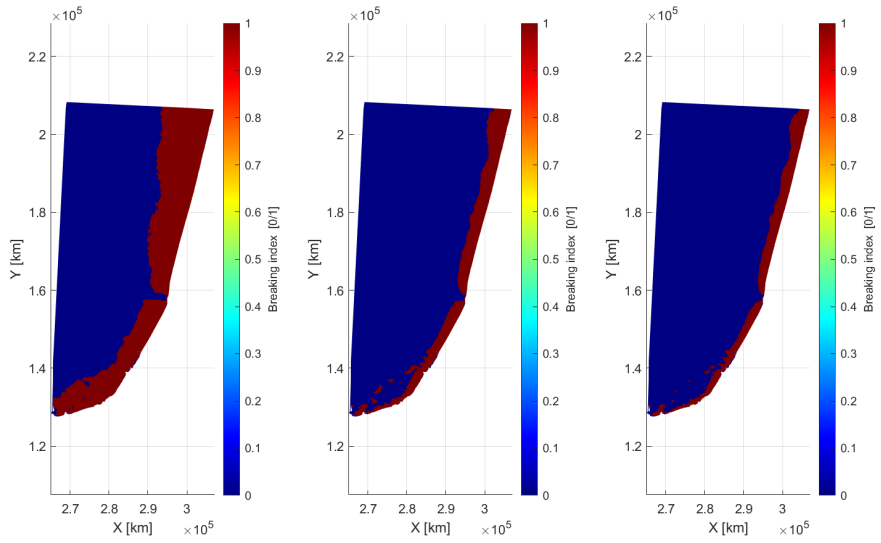

Figure 6.12: Breaking Index with $H_s = 8m$,$T_p = 11s$ forcing and limit thresholds $Q_{B,lim}$ of 10^{-3}(left) 10^{-2} (middle) 5.10^{-2} and (right) 10^{-1}

6.2.2 Variability of the maximal expected loading

Spatial distribution of extreme sea state parameters

The environmental contours obtained allow to analyze the spatial distributions of extreme sea state parameters. In this section, the hindcast data presented in Chapter 4 is used to compute corresponding environmental contours, over each point of the domain. It is underlined that the significant breaking wave height used to compute the MESF is computed from all the wave scales (i.e. using equation 6.1.35) and that the breaking threshold $Q_{B,lim}$ was set to 10^{-3}. In order to analyze the reason of the variability of $F_{S_{max}}$ the variability of H_S, H_{BS} and V should be studied since that for a cylinder of known diameter the Equation 6.1.3 reduces to :

$$F_{S_{max}} = \alpha.\frac{H_{BS}^2}{H_S}.V^2 \tag{6.2.1}$$

With, $\alpha = \rho.0.29.\frac{2D}{\pi}$.

In Figure 6.13 the scatter plot of the significant breaking wave height versus the significant wave height shows that the two values are linearly correlated. It is then possible to compute a constant parameter called χ such as $H_{BS} = \chi.H_S$. Here, a value χ of 1.22 was found while [DNV 2010] proposes a value of 1.4.

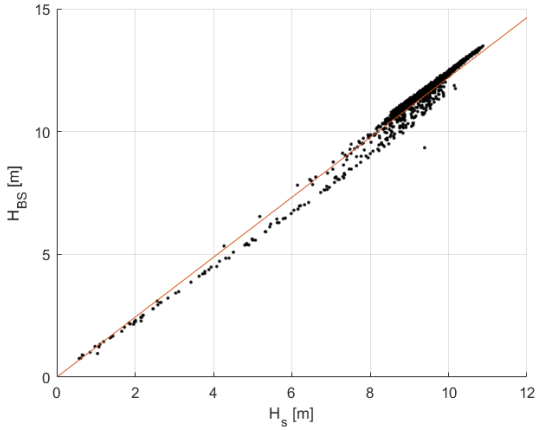

Figure 6.13: Scatter plot of the significant breaking wave height versus the significant wave height

The spatial distribution of the χ parameter (Figure 6.14) shows two main behaviours over the studied coastal domain. Near the coastline, the value of χ ranges between 1.06 and 1.2, while further offshore the value is almost constant at 1.24. This figure seems to lead to the preliminary conclusion that close to the shore a broader portion of the wave spectrum is affected by wave breaking compared to the offshore, since the energy associated with the breaking portion of the spectrum (H_{BS}) is closer to the energy associated with the complete spectrum (H_s).

Since a linear relation exists between H_B and H_S it is now possible to further reduce Equation 6.2.1 to :

$$F_{S_{max}} = \alpha.\chi^2.H_s.V^2 \tag{6.2.2}$$

Therefore when studying the variability of the the Maximal Expected Slamming Force (MESF), the variability of both H_S and C_p should also be analyzed. Spatial distribution of the MESF is shown in Figure 6.15 alongside the corresponding $H_s; C_p$ duets.

Two main behaviours can be observed for the evolution of H_s. Along cross-shore profiles, H_s increases rapidly from 1m up to 10m with the increase in water depths. Along long-shore profiles, especially in the southern part of the domain, a higher variability is observed, with maximal evolution between adjacent points of 50%. For the wave celerity, similar observations can be made regarding its cross-shore and long-shore evolution. Again the southern part of the domain presents the highest level of variability with maximal variation between two adjacent point of 45%.

The MESF distribution plotted in Figure 6.15 shows a homogeneous distribution of the load. The MEFS over a 50-year return period varies between 100 kN in the coastal area and 4.7 MN more offshore. Although it is possible to observe some global trends, such as higher loads in the offshore, some local patterns need to be highlighted. As was explained in previous Chapters, both the area of the submarine canyon and the Bask coast show high levels of spatial variability. Regarding the MESF, high levels of variability are also observed over these areas. In the top panel of Figure 6.16,

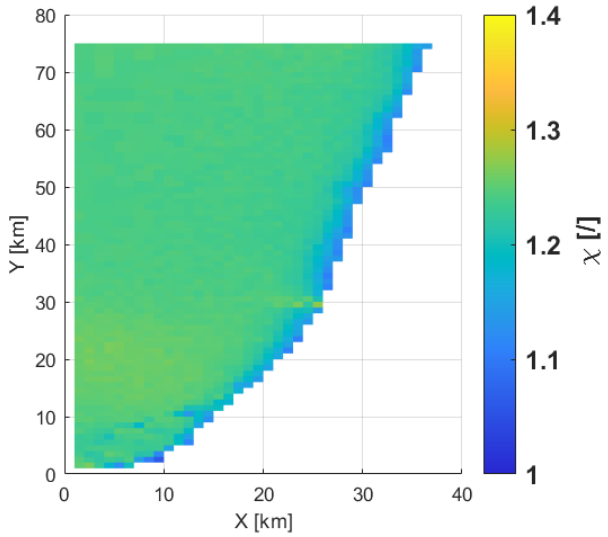

Figure 6.14: Spatial distribution of the χ parameter

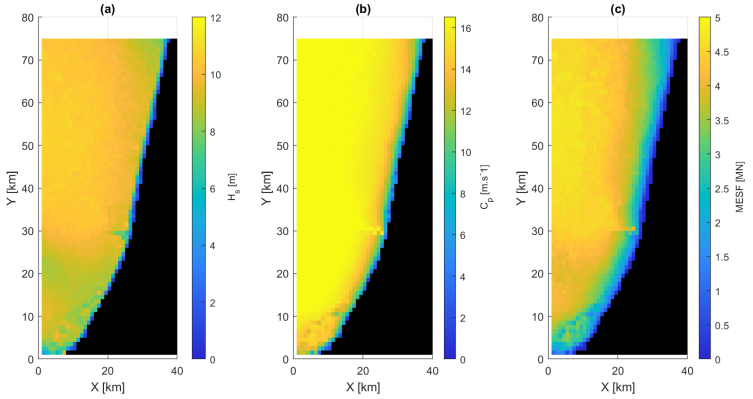

Figure 6.15: Maximal expected value of (a) H_s , (b) C_p and (c) MESF over a 50 year return period

right over the canyon, the values are in the range of the offshore domain although being close to the shore. Over this area, a MESF of 4.2 MN is reached (X=24 km Y= 30 km) next to a location where the MESF is 2MN. In the bottom right panel of figure 6.16, high levels of spatial variability are observed for the MESF in the Bask Coast. Values range from 70kN in the coastal area up to 3.7 MN. Over this region the spatial variability reaches a maximal value of 50% between adjacent points representing an absolute difference around 1 MN.

This variability can be explained by looking at equations 6.1.3. The slamming force is driven by the evolution of H_s and the phase speed squared ${C_p}^2$ which are in turn driven by water depth. In Figure 6.17, the maximal expected impact force is plotted against the water depth. We observe

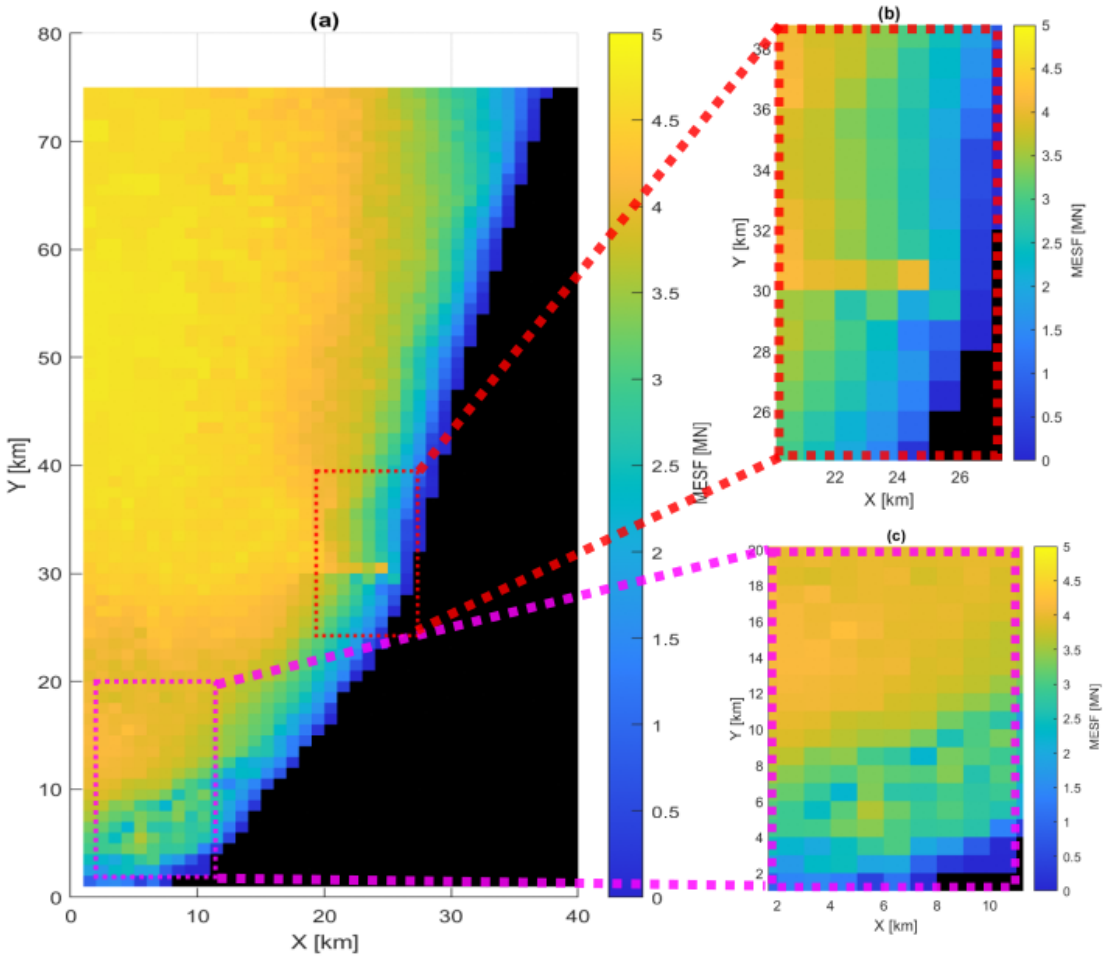

Figure 6.16: Spatial distribution of the Maximal Expected Slamming Force [MN] for a 50 year return period over (top) the Capbreton submarine canyon area and (bottom) the Bask coast

two different types of behaviour. Between 0 and 60m, a very strong correlation between the water depth and the impact force clearly appears. In that region, both the significant wave height and the wave celerity increase drastically (see Figure 6.18). For water depths higher than 60m, both the significant wave height and the wave celerity have reach their maximum values around 9m and 16 $m.s^{-1}$ respectively. For this range of water depth, the MESF also reaches a plateau between 4MN and 4.5 MN.

In order to understand better the respective influence of H_s and C_p on the MESF the ratio $H_s/({C_p}^2)$ versus the water depth is plotted in Figure 6.19. We observe three types of evolution.

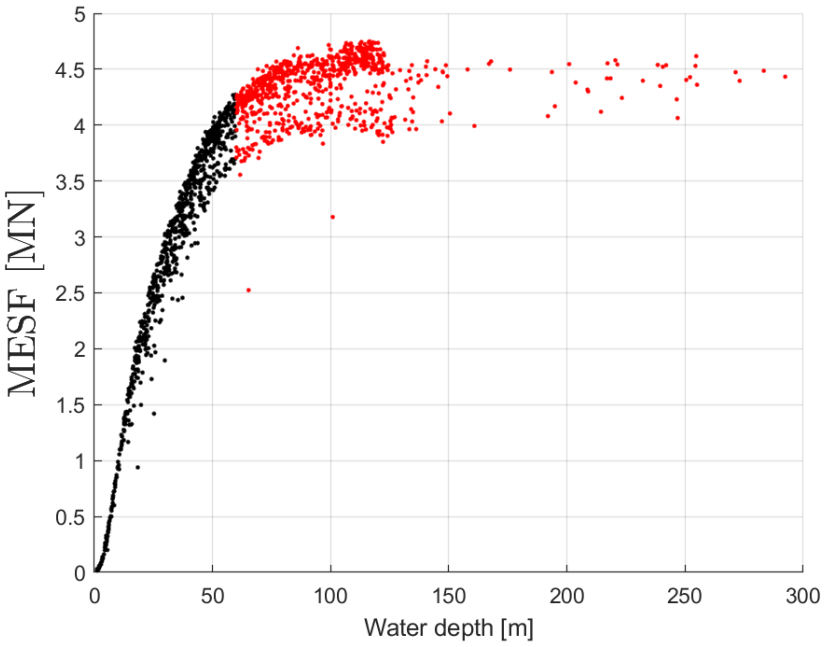

Figure 6.17: Scatter plot of MESF [MN] versus water depth smaller than 60m (black) and higher than 60m (red)

For very small water depths (i.e. less than 8m), H_s increases faster than C_p^2 while for water depth between 8 and 60 m, C_p^2 increases faster. Finally, for water depth higher 60m, H_s and C_p^2 evolve the same way since the ratio $H_s/({C_p}^2)$ remains constant. Overall, Figure 6.19 shows the preponderant role of C_p in the absolute value of the MESF since H_s only represents 3 to 10 % of C_p^2. However we also observe in Figure 6.18, that for a given water depth that C_p is almost constant while variations up to 50% are observed for H_s. This means that although the magnitude of the MESF is mainly driven by C_p, its variability for a given water depth is driven by H_S.

Influence of the return period on the maximal expected values

The return period is a key parameter when studying extreme sea states and its consequences. In the previous sections, the spatial distribution of wave parameters (H_s, C_p and MESF) where studied for a 50-year return period. However, less extreme sea state (e.g. with return period of 5 and 10 year) may also induce slamming forces to WECs. The left panel of Figure 6.20 shows the relative difference in H_s for a 5-year return period compared to a 50-year return period. We observe an almost uniform difference, with a 20% increase when looking at values computed with a 50-year return period. It also has to be noted that at the points close to the shore (less than 1km) there is less decrease with the lowering of the return period. Regarding the relative difference for wave celerity, only a slight increase is observed in the middle panel of Figure 6.20. The decrease value of few percents may be related only to computation approximation in the contour.

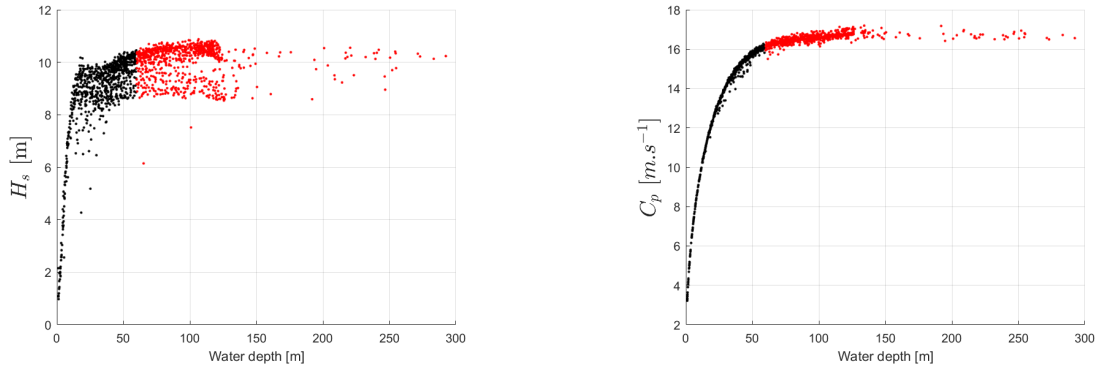

Figure 6.18: (left) Scatter plot of H_s versus water depth with water depths smaller than 60m in black and water depths higher than 60m in red. (right) Scatter plot of C_p versus water depth with water depths smaller than 60m in black and higher than 60m in red.

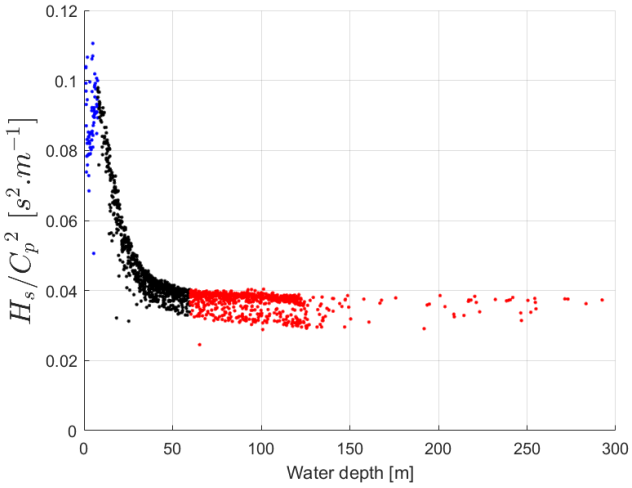

Figure 6.19: Scatter plot of $H_s/({C_p}^2)$ versus water depth with water depths smaller than 7.8m in blue, water depths higher between 7.8m and 60m in black and water depths higher than 60m in red.

Consequently, the relative difference pattern observed for the MESF (right panel of Figure 6.20) is very similar to the one presented for H_s with increase values around 20%. However, for some locations (located in the coastal area at Y=30 km, in black in the Figure) the MESF computed with reduced return period is equal to 0, meaning that at these location no breaking should occur for the 5-year return period.

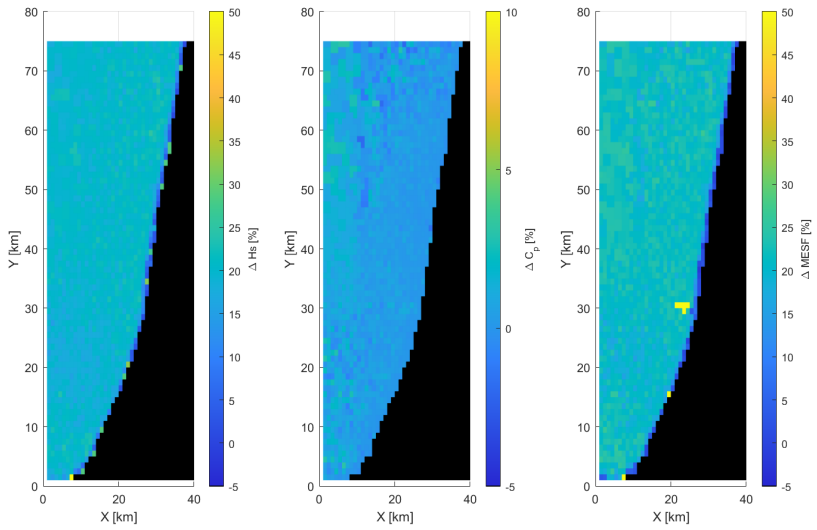

Figure 6.20: Relative difference for a 5-year return period compared to a 50-year return period in (left) H_s, (middle) C_p and (right) MESF. Positive values represent higher values for the parameters computed with the 50-year return period.

Influence of the sample size on the maximal expected values

The contour line approach used to estimate extreme value is based on hindcast data. For one point of the domain studied in this PhD, we have a data sample of 128 480 data points (3 hour output time step over 44 years). However, other wave hindcast [Delpey et al. 2021]; [Iglesias, López, et al. 2009]; [Robertson et al. 2016], may cover smaller periods. Therefore, the influence of the sample size on the maximal expected values is of interest. In this section, the hindcast data presented in Chapter 4, is divided into smaller datasets of 5 years representing 14 600 data points. Then, the contour of extreme sea state are computed for a 50-year return period. The results of the difference between the two sample sizes are shown in Figure 6.21.

We observe that the maximal expected values are overall the same despite the sample size. However in the coastal domain, relative variations around 50% are visible. This result supports the fact that the joint distribution model presented in equation 6.1.2 fitted over a 5 year sample (i.e. 14 600 data points) produces accurate results.

6.3 Discussion

6.3.1 Expected MESF

In the results section, the maximal load that could be expected over certain periods (i.e. 5 year, 10 year and 50 year return periods) were discussed. But these loads may not have the same probability of appearance. Indeed, for a given return period, although each $[H_s; T_E]$ duets read from the environmental contours have the same probability of appearance, the considered sea states may

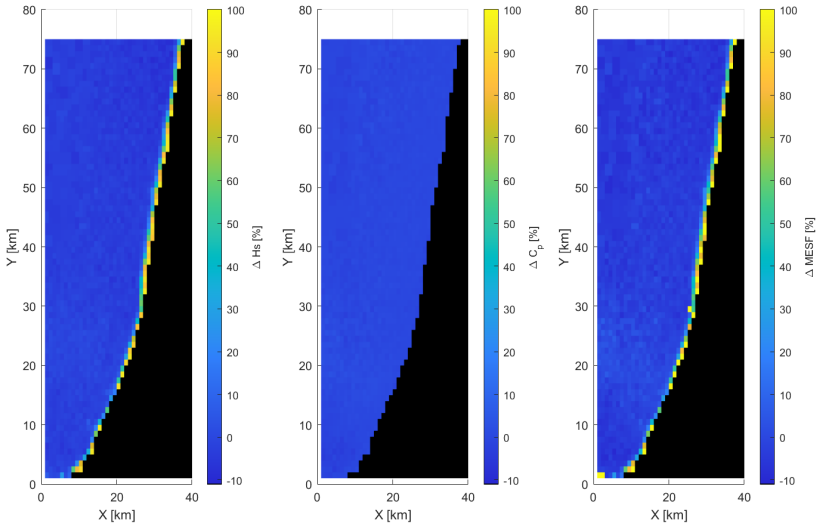

Figure 6.21: Relative difference between the extreme sea state parameters computed with a 5 year sample and the full 44 year hindcast. (left) Relative difference in H_s (middle) Relative difference in C_p (right) Relative difference in $MESF$. Positive values represent higher values for the parameters computed with the 44 year hindcast.

not have the same breaking probability Q_b. Therefore, the probability of a MESF for a given return period (noted $P(MESF_{T_r})$ is :

$$P(MESF_{T_r}) = \frac{1}{Tr} * Q_b \tag{6.3.1}$$

The expected MESF is then given by :

$$E(MESF_{T_r}) = MESF_{T_r} * P(MESF_{T_r}) \tag{6.3.2}$$

The expected MESF is expected to provide the stakeholders of a WEC project an objective indicator regarding the wave impact risk for a device. The expected MESF intends to account for both the magnitude of the load and the likelihood of breaking.

Figure 6.22 shows in the upper panels ((a) (b) and (c)) the MESF associated with 5, 10 and 50 year return periods and the lower panels ((d), (e) and (f)), the corresponding expected MESF. We observe in Figure 6.22 that although the highest MESFs are found in the offshore area the highest levels of expected MESF are to be found in the nearshore area. This holds true for all the return periods considered. This can be explained by the fact that the variation in Q_b is much higher than the variation in the MESF. We can also observe that the locations of the highest expected MESFs are the same for all the return periods. Another interesting aspect, that has already been discussed in previous chapters, is the high spatial variability. Here, regarding the expected MESF, we can observe variations up to 500% between adjacent points.

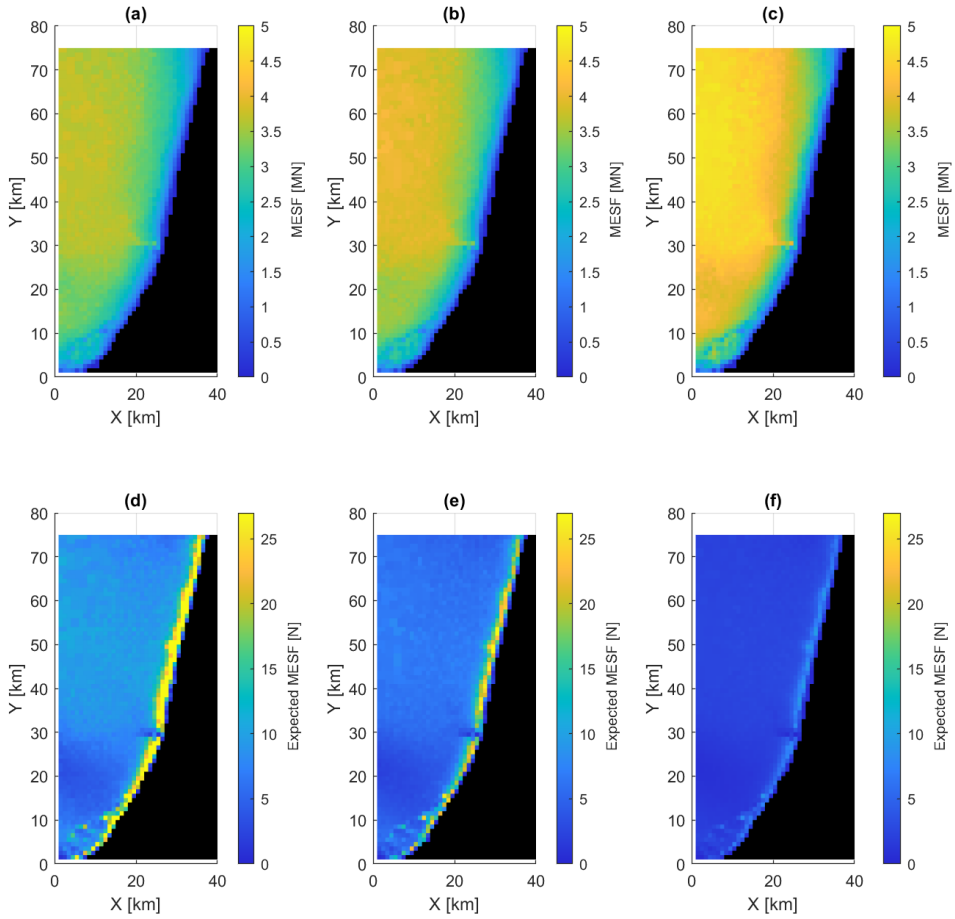

Figure 6.22: (a) MESF for a 5 year return period (b) MESF for a 10 year return period (c) MESF for a 50 year return period (d) Expected MESF for a 5 year return period (e) Expected MESF for a 10 year return period (f) Expected MESF for a 50 year return period

6.3.2 From the force to the stress

In order to compute the stress acting on the structure we propose the mechanical model shown in Figure 6.23. A cylinder of exterior diameter D_1 and interior D_2 and height L_t is considered embedded in the sea bottom. The wave loading is considered as an equally distributed load noted q_{impact}. The impact load is applied over λH_b noted L_1. Therefore the value of the distributed load is $\frac{F_{impact}}{\lambda H_{Bs}}$. The center of the load is located at $z = h + \eta_b$. The height from the bottom level to the start of the load q_{impact} is noted L_2.

The first moment of inertia for a cylindrical section is computed as :

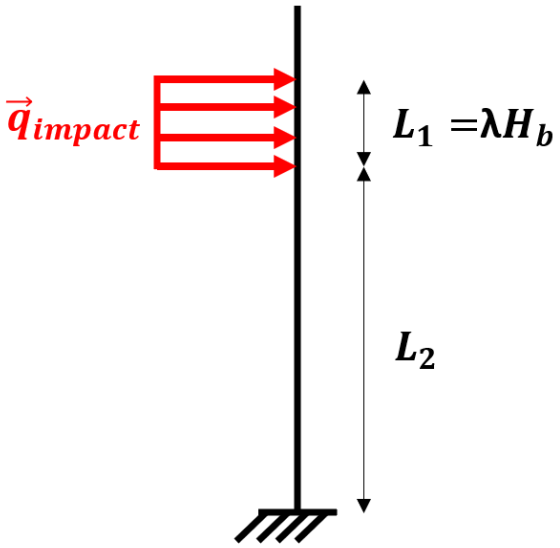

Figure 6.23: Sketch of the mechanical model with only the force related to the breaking part of the waves

$$Sy(z') = D_2 e\sqrt{Dz' - z'^2} \tag{6.3.3}$$

The second moment of area for any surface is given by :

$$Igx = \int\int y^2 dA \tag{6.3.4}$$

Therefore for a circular shape the second moment of area is given by :

$$Igx = \pi\frac{D^2}{64} \tag{6.3.5}$$

Finally, for a cylindrical shape the second moment of area is given by :

$$Igx = \pi\frac{{D_2}^2 - {D_1}^2}{64} \tag{6.3.6}$$

For the first load case, the shear and bending moment along the beam are given by the following expressions

For $z \subset [0, L_2]$:

$$V_1(z) = -q_{impact} L_1 \tag{6.3.7}$$

$$M_1(z) = -q_{impact} L_1 \left(L_2 + \frac{L_1}{2}\right) + q_{impact} L_1 z \tag{6.3.8}$$

For $z \subset [L_2, L_2 + L_1]$:

$$V_2(z) = -q_{impact} L_1 + q_{impact}(z - L_2) \tag{6.3.9}$$

$$M_2(z) = -q_{impact}\frac{z^2}{2} + q_{impact} z(L_1 + L_2) - q_{impact}\frac{(L_1 + L_2)^2}{2} \tag{6.3.10}$$

For $z \subset [L_2 + L_1, L_t]$:

$$V_3(z) = 0 \tag{6.3.11}$$

$$M_3(z) = 0 \tag{6.3.12}$$

The we can obtain the maximal values of shear and bending moment which are located at seabed level at z=0.

The shear stress is expressed as follows :

$$\tau(y, z) = \frac{V(z) S_y(y')}{b(y) Igy} \tag{6.3.13}$$

With,

- V(z) : The shear at height z
- $S_y(y)$: The first moment of area at position y
- b (y) : the width of the section at position y
- I_{gy} : The second moment of inertia of the section

We finally obtain the following expression for the maximal shear stress :

$$\tau_{max} = -\frac{16 q_{impact} L_1 D_2^2}{\pi(D_2^4 - D_1^4)} \tag{6.3.14}$$

The normal stress is expressed as follows :

$$\sigma(y, z) = \frac{M(z) y)}{Igy} \tag{6.3.15}$$

With,

- M(z) : The bending moment at height z
- y : The position where the normal stress is computed
- I_{gy} : The second moment of inertia of the section

We finally obtain the following expression for the maximal normal stress :

$$\sigma_{max} = -\frac{32 q_{impact} L_1 \left(L_2 + \frac{L_1}{2}\right) D_2}{\pi(D_2^4 - D_1^4)} \tag{6.3.16}$$

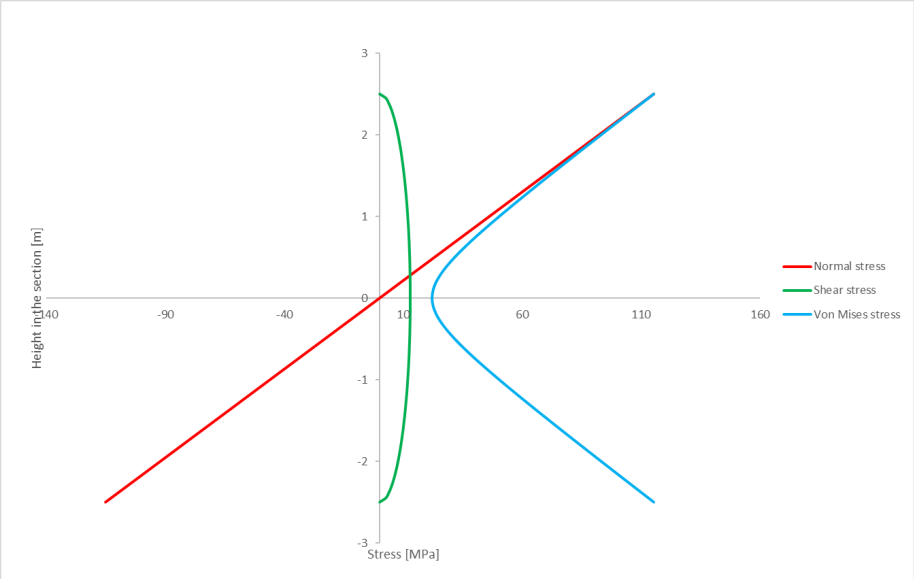

Figure 6.24: Evolution of the stress along the section

The von Mises stress σ_{VM} is given by :

$$\sigma_{VM} = \sqrt{\sigma^2 + 3\tau^2} \tag{6.3.17}$$

Spatial distribution of the stress

We observe that the maximal von Mises stress is located at the top and bottom of the section. In fact, the maximal von Mises stress corresponds to the maximal normal stress. Therefore the maximal von Mises stress in the section is :

$$\sigma_{VM\,max} = \frac{32 q_{impact} L_1 \left(L_2 + \frac{L_1}{2}\right) D_2}{\pi (D_2^4 - D_1^4)} \tag{6.3.18}$$

When looking at the expression of the von Mises stress, for a given cylinder (i.e. fixed value of D_1 and D_2), we observe that the von Mises stress is positively correlated with q_{impact}, L_1, L_2. L_1, L_2 are dependent of the water depth and breaking wave height(which is in turn dependant of H_s). This means that for a similar wave load the water depth has also an influence on the value of the maximal von Mises stress.

When looking at the integrity of a structure, the important parameter to consider is the stress in the material. In the result section presented before, the focus was made on the impact force. In Figure 6.25, the spatial distribution of the stress for the structure presented in the Methodology section is shown. This spatial distribution is very similar to the spatial distribution of the force (see Figure 6.15). When looking at the values obtained, we observe that values are ranging between 0 and 700 MPa. These values need to be compared to the elastic resistance of steel which varies between 200 and 500 MPa depending on the grade of the steel. We observe that the first limit value of 200 MPa is reached in the nearshore area for water depth around 20 to 30m.

The stress magnitude mentioned here relates to an embedded slender structure which may not be the most optimized solution given the high bending moment induced. Other solutions, such as floating WECs would be more appropriate regarding this issue but other problems would then emerge such as force transmission between mooring lines and the WEC among other.

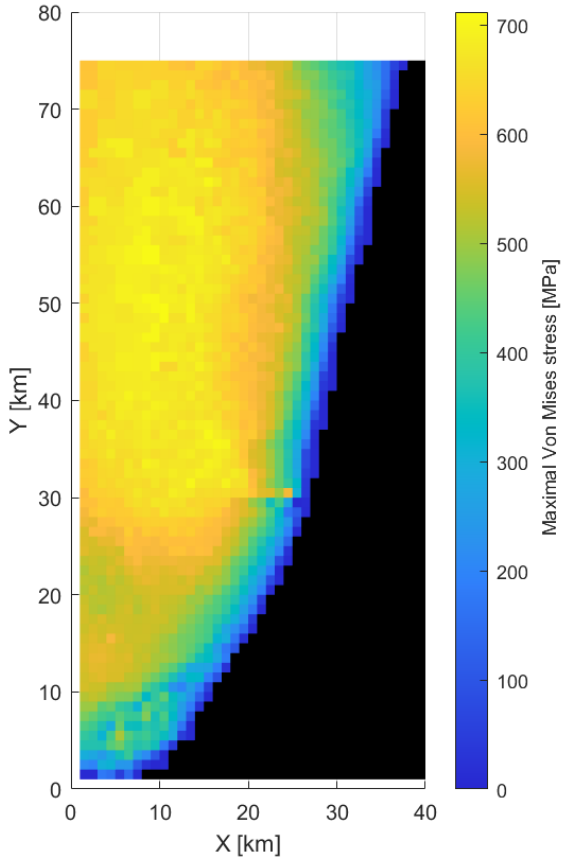

Figure 6.25: Spatial distribution of the maximal von Mises stress induced by the maximal expected breaking force over 50 year.

6.4 Conclusion

The objective of this chapter was to compute the maximal loads acting on a generic WEC over a large computational domain. From a 44-year hindcast data, long term sea-state distributions were computed using environmental contours. At each location of the domain, the Maximal Expected Slamming Load (MESF) was computed for a given return period. For a 50 year return period,

maximal values ranging between 0 and 4.5 MN were computed. The strongest values were computed for water depths higher than 50m. A high correlation level between the MESF and the water depth was also underlined. A sensitivity analysis was also carried out regarding the influence of the return periods and the sample size used for computing environmental contours. Then the expected MESF was computed in order a different perspective to the subject. Although higher levels of MESF are computed in the offshore, the expected values appear to be higher in the nearshore area where more waves are breaking. Finally, a first attempt to compute the stress in the structure is presented and shows that the magnitude of the load may overpass the mechanical capacity of the structure when going offshore.

This methodology and the related sensitivity analysis would benefit greatly from being applied on another domain to verify the preliminary conclusions drawn in this chapter. Furthermore, this methodology has been design in a modular way where it is possible to change part of the tools used. Indeed some of the tools used here are independent from each other allowing to replace them. For example it would be possible to change the contour method or change the load model.

Chapter 7

Optimization of WEC location based on cross-comparison of resource and efforts

In order for wave energy to become a reliable source of energy, several critical challenges must be addressed, with the optimization of the localization standing as a key aspect. Finding the optimal location for deploying WECs is crucial to ensure the Lowest Levelized Cost Of Energy (LCOE). The latter is achieved by maximizing energy harvest, while minimizing economic cost. Although it is understood that other factors may affect the process of choosing a localization (e.g. environmental impact), this chapter uses the results from Chapter 4 and 6, and focuses on the combination of wave energy resource and wave impact loads information.

Once both the spatial distributions of the wave energy resource and the impact loads are computed, one should be able to search an efficient compromise between the related opportunities and constraints for the WECs. However, the best location with respect to wave energy might not be the best choice regarding impact loads, and vice versa. Therefore, the co-existence of these two often conflicting criteria requires to consider the trade-off between them. For this purpose, a methodology is proposed and discussed in this chapter to characterize and compare the suitability of a WEC location in the coastal/nearshore area. The suitability is evaluated through the creation of indexes as inspired by [Galparsoro et al. 2012].

This chapter first introduces the methodology leading to compute various indexes that are compared in the results section. The results are then discussed together with possibilities of application and improvements. Finally, conclusions are drawn and perspective of this work are mentioned.

7.1 Methodology

A Suitability Index (SI) qualifies each location of a study domain with respect to WEC installation [Galparsoro et al. 2012]. The Suitability Index typically ranges from 0 for unsuitable areas, to 1 for very suitable areas (i.e. small loads and high resource). [Galparsoro et al. 2012] proposes to compute the SI as follows :

$$SI(x,y) = \frac{\Sigma_{i=1}^{N} V^{i}_{limiting-factor}(x,y)}{N} \Pi_{j=1}^{M} V^{j}_{excluding-factor}(x,y) \tag{7.1.1}$$

where, $V^{i}_{limiting-factor}$ is a value between 0 and 1, associated with the i-th factor, and $V^{j}_{excluding-factor}$, is either 0 or 1 depending if the location is affected by the j-th factor. In this work, the focus is set exclusively on two factors : the wave energy resource and the impact loads.

The first limiting factor is associated with the Maximal Expected Slamming Force (MESF) (see Chapter 6), and is named Impact Index (II). It is computed as :

$$II_{limiting}(x,y) = 1 - \frac{MESF(x,y)}{max(MESF)} \tag{7.1.2}$$

For the purpose of this work, the lower limit of $II_{limiting}$ is set to the maximal value of the MESF computed over the domain. This means that for the location where the MESF is maximal the $II_{limiting}$ will be equal to 0.

It has been mentioned before that impact loads may exceed the maximal resistance of a WEC. Therefore, in order to maintain its integrity, a design value should not be exceeded. For illustration purposes, this threshold was chosen arbitrarily as the 90% of the maximal MESF over the domain. This reads as :

$$II_{excluding}(x,y) = 0, \text{ if } MESF(x,y) > 0.9 \times max(MESF) \tag{7.1.3}$$

Or,

$$II_{excluding}(x,y) = 1, \text{ if } MESF(x,y) < 0.9 \times max(MESF) \tag{7.1.4}$$

The second limiting factor is associated with the Resource Index, which represents the available wave energy resource at each point of the domain. For the present application, the mean annual resource will be considered. However, for a realistic scenario of electricity production by the WEC, the time windows when the WEC is effectively functioning should be considered when computing the annual energy resource. Indeed, each WEC has a specific range of operating conditions. Outside of this range, no energy is produced by the WEC. Therefore, the resource will be computed for the periods when the energy flux is lower than 100 kW/m. This restriction allows to discard very energetic events, during which WEC usually go into safety mode and are thus not producing energy. The RI is then computed as follows :

$$RI_{limiting}(x,y) = \frac{Resource_{mean}(x,y)}{max(Resource_{mean})} \tag{7.1.5}$$

Considering the aforementioned limiting and excluding factors, the SI is computed as :

$$SI(x,y) = \frac{II_{limiting}(x,y) + RI(x,y)}{2} II_{excluding}(x,y) \tag{7.1.6}$$

7.2 Results

The scatter plot of the limiting Impact Index versus the limiting Resource Index is shown in Figure 7.1 for all the points in the study domain (Figure 6.16). For a significant number of points, the II and RI seem to be correlated, where a high RI implies a low II. However, it also appears that a set of points located in the top right corner of the scatter plot, has both high RI and II. These points are then very interesting regarding WEC installation, since at these locations, the wave energy resource should be high and the MESF low.

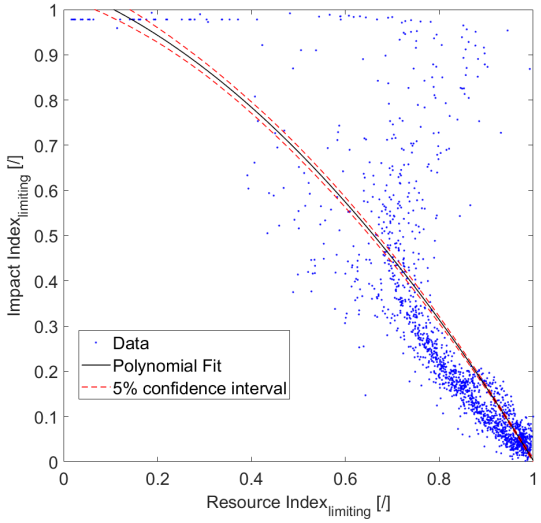

Figure 7.1: Scatter plot of the limiting Impact Index versus the limiting Resource Index

Figure 7.2 shows the spatial distribution of the 3 indexes defined in the previous section. Looking at the Impact Index, one can see that the best location regarding WEC installation are located in the nearshore area. This result is in agreement with Chapter 6, where the MESF was shown to increase rapidly with water depth (Figure 6.17). Some locations (e.g. X=12km;Y=10 km or X=7km;Y=8km) in the southern part of the domain are worth noticing. These areas have a higher Impact index compared to other areas located at the same distance from the coast. Additionally, offshore locations appear to be unsuited for WEC installation (i.e. $II_{excluding} = 0$).

The spatial distribution of the Resource Index, is also in agreement with the results from Chapter 4, where the highest levels of wave energy resource are located in the offshore area with the notable exception of focusing areas in the nearshore. However, the magnitude of these hotspots appears to be reduced compared to the results from the hindcast (see Figure 4.3), indicating that the mean value of the wave energy resource at these locations is partly driven by extreme events, where the wave energy flux is higher than 100 kW/m.

Then, using Equation 7.1.1, the Suitability Index is shown in Figure 7.3. One can see that, the highest levels of SI are located in the nearshore area. Specifically, the highest levels of SI are found at the nearshore locations where the wave energy resource was focused.

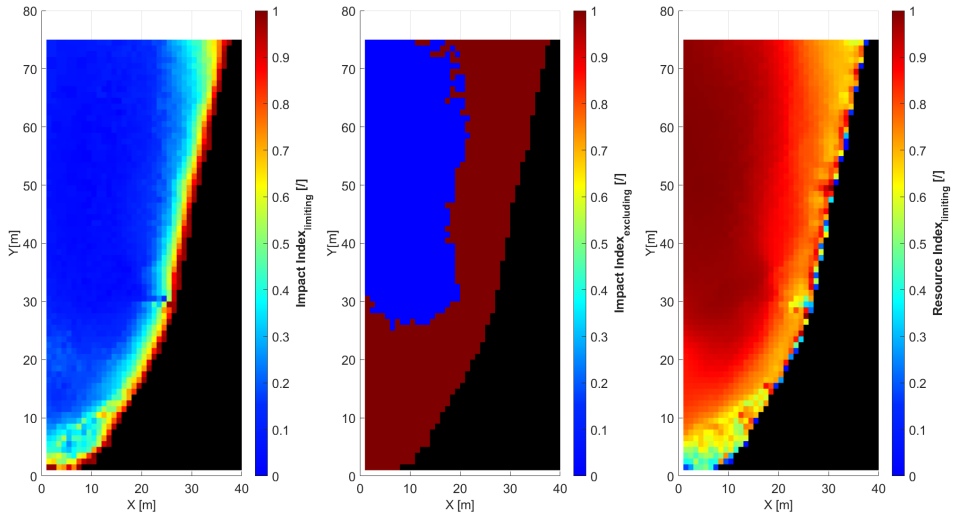

Figure 7.2: (left) Limiting Impact Index II computed with a 50-year return period, (middle) Excluding Impact Index II and (right) Resource Index RI computed from the 44-year hindcast data

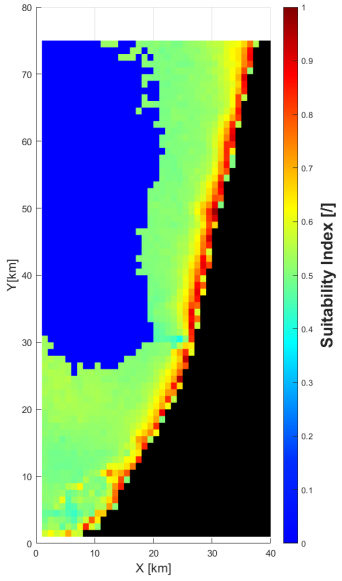

Figure 7.3: Spatial distribution of the Suitability Index

7.3 Discussion

It appears that the proposed method of computation of SI is not able to discriminate locations with high difference between II and RI. For example, averaging the limiting factors would provide the same SI for a location with $(II = 0.1, RI = 0.9)$ and an other one with $(II = 0.5, RI = 0.5)$. If such locations must be differentiated by the SI, an alternative computation for the Suitability Index could be proposed as a product of the individual indexes instead of a sum, giving :

$$SI(x,y) = \Pi_{i=1}^{N} V^{i}_{limiting-factor} . \Pi_{j=1}^{M} V^{j}_{excluding-factor} \tag{7.3.1}$$

An alternative spatial distribution of the Suitability Index computed with Equation 7.3.1 is shown in Figure 7.4. The highest levels of SI are still located in the nearshore but higher levels of variability are obvious, allowing to better discriminate each location. Additionally, it appears that the newly computed SI does not affect the position of the locations with the highest SI observed in Figure 7.3 (i.e. X=24km;Y=24km and X=30km;Y=49km).

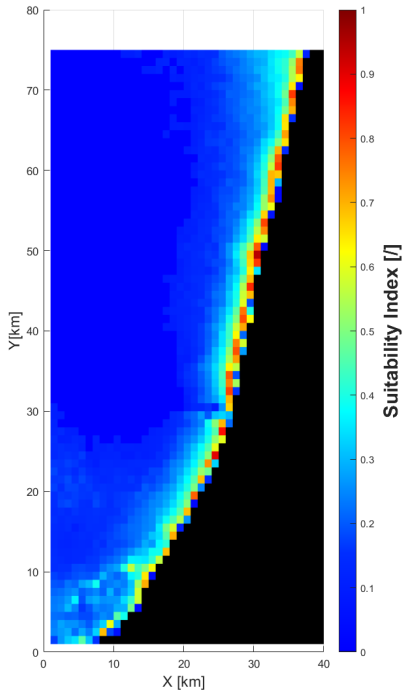

Figure 7.4: Spatial distribution of the Suitability Index computed from Equation 7.3.1

The use of Equation 7.1.6 or 7.3.1 implies that all the limiting factors have the same importance although it may not be the case. When deciding the location of a WEC, the stakeholders should consider the relative importance of each limiting factor. For example, if a WEC could be designed to resist to all wave impacts with no additional costs, the weight applied to the factors related to

wave impact should be equal to 0. Alternatively, if one would want to increase the lifetime of a WEC, the weight applied to the limiting factors related to wave loading should be increased with respect to the one related to the energy resource. The SI would then be computed as :

$$SI(x,y) = \frac{\Sigma_{i=1}^{N} \alpha_i . V^i_{limiting-factor}(x,y)}{\Sigma_{i=1}^{N} \alpha_i} \Pi_{j=1}^{M} V^j_{excluding-factor}(x,y) \tag{7.3.2}$$

where, α_i corresponds to the weight applied to the limiting factor $V^i_{limiting-factor}$.

In the Discussion section of Chapter 6, to account for the probability of appearance of a given wave impact, the "expected MESF" was introduced. The study of its spatial variability showed that the highest levels of expected MESF were located in the nearshore area, where most of the wave breaking occurs (see figure 6.22). To account for the expected MESF in the computation of the SI, a new limiting index, the Expected Impact Index (EII) is proposed :

$$EII_{limiting}(x,y) = 1 - \frac{\text{Expected } MESF(x,y)}{max(\text{Expected } MESF)} \tag{7.3.3}$$

The spatial variability of the EII is shown in the left panel of Figure 7.5. The most nearshore points appears to be the best locations with EEI values higher than 0.7. Although the breaking probabilities are higher at these location, very low MESF values induce low values for the EEI. However this result has to be nuanced, since the chosen resolution of the regular grid may not be able to capture the rapid increase in MESF occuring at these water depths (see Figure 6.17). Approximately 1km off the coast, one can see that a band approximately 2 km wide appears to be less appropriate for WEC installation. At these locations, both high MESF and breaking probabilities induce low EII values. Further offshore the decrease of the breaking probabilities results in an increase in EII indicating that this area may be the most suited for WEC installation. Even further offshore (around X=10km and Y=50km), although the breaking probability is still low, higher MESF values increase the hazard for potential WECs.

Finally, the SI computed from Equation 7.3.1 including the limiting EII and RI and the excluding II, is shown in right panel of Figure 7.5. It is interesting to observe that the results provided by Figure 7.5 are completely different compared to the results shown in Figure 7.3. This contradictory results highlights the fact that although promising, the methodology proposed here is extremely sensitive to the used parameters. A better understanding of the failure mechanisms of the WECs would allow to better weigh the respective importance of the load and the frequency of breaking, thus allowing to use the most appropriate one or to build a new parameter more suited to describe the hazard the WECs are facing.

7.4 Conclusions

The choice of placing a WEC project is a multi-criteria problem. In this chapter, the methodology proposed by [Galparsoro et al. 2012] is applied to the South-Aquitaine nearshore area. Two aspects are studied : wave induced impact loads and the wave energy resource. The creation of the corresponding indexes allows to qualify a point with respect to its suitability for WEC installation. Overall, it results that the best area with respect to the wave energy resource, are also the worst ones regarding wave impact loads. However, this study shows the existence of nearshore locations that combine both high levels of wave energy resource and low levels of impact loads. These type

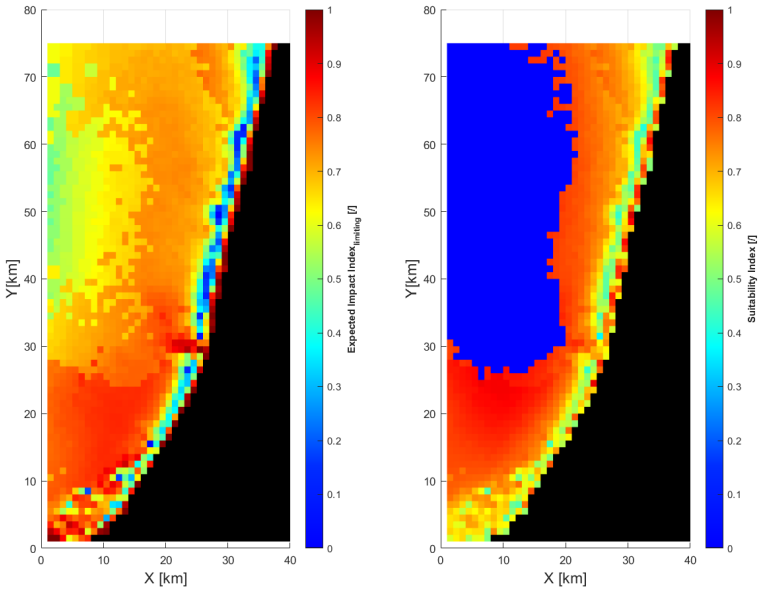

Figure 7.5: (left) Expected Impact Index (EII) (right) Spatial distribution of the Suitability Index computed from Equation 7.3.1 including the EII

of localization should obviously be prioritized for WEC installation.

Computing indexes such as the SI requires a non-negligible amount of arbitrary choices. The amount and type of limiting and excluding factors to include, is the first one. Depending on the number of included parameters, the final result on the SI may give a false sense of accuracy in addition to complexifying its understanding. In fact, the more parameters are used, the harder it is to draw conclusions, due to the fact that the limiting factors can balance each other out. The decision to add weighting to the limiting factors may also affect significantly the SI. The computation of these weights requires additional computation and hypothesis and is therefore beyond the scope of this manuscript.

Chapter 8

Conclusions

8.1 Main results

High levels of spatio-temporal variability were identified both at local and regional scale for the wave energy resource. At regional scale, a North/South gradient of wave energy flux was identified, with higher values in the northern part of the domain. At local scale, strong gradients were also identified inducing wave energy hotspots. Wave refraction was shown to be the main driver of this variability. This refraction affects particularly the longest waves, which are also the most energetic waves. Consequently, it appears that wave refraction over the submarine canyon of Capbreton may be the reason of the North/South gradient of the mean wave energy observed over the domain. The strong influence of the spectral distribution of wave energy on WEC production estimates was also shown, highlighting the need for the spectral information when computing wave energy output of a WEC.

Regarding the hazard induced by wave impacts on structures, the objective of this manuscript was to compute the spatial distribution of the Maximal Expected Slamming Force (MESF) for a given return period on a generic structure. First, from the sea state's statistical parameters, using environmental contours, extreme events occurring for a given return period were computed. The MESF was shown to be strongly correlated with water depth, with higher values offshore. Additionally, high levels of spatial variability were highlighted in the nearshore area in the presence of strong bathymetric gradients.

Finally, the wave energy resource distribution and the MESF distribution were compared to identify the best location for WEC installation over the South-Aquitaine nearshore area. Although, a correlation between the resource and the loads was observed, some locations were the resource is high and the hazard low were identified.

8.2 Limits and perspectives

Although wave refraction was identified as one of the main driver of the spatio-temporal variability of wave energy, further investigations would permit to refine this conclusion. In fact, larger oceanic circulation processes are also expected to affect the spatio-temporal distribution of wave energy. Among them, it is possible that a shadowing effect induced by the shape of the Iberian peninsula reduces the influence of western swells on the southern part of the South-Aquitaine coast.

The high-resolution hindcast used in Chapter 5 allowed to study the influence of the wave energy distribution at small scale. However, the variability levels identified may be in the uncertainty range of the model. Investigating the precision of spectral wave models at such high resolutions would then permit to increase the confidence in the produced results. Since the spectral distribution of wave energy was shown to influence the production estimates of WECs, investigating further this spectral distribution over hindcast periods would allow to improve the design of WEC for specific locations.

The methodology proposed in Chapter 6 is thought as a first step towards the computation of the spatial distribution of loads on a real WEC. To that end, additional studies would need to use a load model specific to the WEC considered. Additionally, to ensure the structural integrity of the WEC, the role of fatigue loads on WECs should be investigated. Finally, modelling the dynamic behaviour of a WEC in response of a wave loading, would allow to understand what type of wave load could lead to the failure of the considered WEC.

The work carried out during this PhD intended to provide a better understanding of the processes that induce nearshore variability on both wave energy resource and loads. These results were used to propose a method to find an optimal location for a wave energy converter. It is also noted that the methodology presented here may be useful for other marine renewable energy devices, since the wave energy resource parameter could be replaced by, or adapted to another energy source. It is therefore expected that the work presented in this manuscript could also be used to optimize the placement of offshore wind turbines.

Bibliography

Abadie, Stéphane ([]). *Theorie des vagues*. ISA BTP.

Abadie, Stéphane et al. (Oct. 2006). "Wave climate and longshore drift on the South Aquitaine coast". en. In: *Continental Shelf Research* 26.16, pp. 1924–1939. ISSN: 02784343. DOI: 10.1016/j.csr.2006.06.005. URL: https://linkinghub.elsevier.com/retrieve/pii/S027843430600207X (visited on 08/19/2020).

Ambühl, Simon (2015). "Reliability of Wave Energy Converters". en. In: pp. 1–96. DOI: 10.13052/rp-9788793379053. URL: http://riverpublishers.com/dissertations_xml/9788793379053/9788793379053.xml (visited on 02/02/2023).

Babarit, A. et al. (May 2012). "Numerical benchmarking study of a selection of wave energy converters". en. In: *Renewable Energy* 41, pp. 44–63. ISSN: 09601481. DOI: 10.1016/j.renene.2011.10.002. URL: https://linkinghub.elsevier.com/retrieve/pii/S0960148111005672 (visited on 07/01/2020).

Bang Huseby, Arne, Erik Vanem, and Bent Natvig (Mar. 2013). "A new approach to environmental contours for ocean engineering applications based on direct Monte Carlo simulations". en. In: *Ocean Engineering* 60, pp. 124–135. ISSN: 00298018. DOI: 10.1016/j.oceaneng.2012.12.034. URL: https://linkinghub.elsevier.com/retrieve/pii/S0029801812004532 (visited on 07/04/2022).

Banner, Michael L., Alexander V. Babanin, and Ian R. Young (Dec. 2000). "Breaking Probability for Dominant Waves on the Sea Surface". en. In: *Journal of Physical Oceanography* 30.12, pp. 3145–3160. ISSN: 0022-3670, 1520-0485. DOI: 10.1175/1520-0485(2000)030<3145:BPFDWO>2.0.CO;2. URL: http://journals.ametsoc.org/doi/10.1175/1520-0485(2000)030%3C3145:BPFDWO%3E2.0.CO;2 (visited on 08/10/2023).

Battjes, J A (1972). "Set-up due to irregular waves". en. In: *Coastal engineering*.

Battjes, J.A. and J.P.F.M. Janssen (1978). "Energy loss and set-up due to breaking of random waves". In: *Proceedings of 16th Conference on Coastal Engineering, Hamburg, Germany*. ISSN: 2156-1028.

Bliss, Nice Sam (2020). *Qualitative risks analysis on wave energy technologies*. Master Programme in Renewable Electricity Production. Uppsala Universitet.

Booij, N., R. C. Ris, and L. H. Holthuijsen (Apr. 1999). "A third-generation wave model for coastal regions: 1. Model description and validation". en. In: *Journal of Geophysical Research: Oceans* 104.C4, pp. 7649–7666. ISSN: 01480227. DOI: 10.1029/98JC02622. URL: http://doi.wiley.com/10.1029/98JC02622 (visited on 02/03/2020).

Boudière, Edwige et al. (Dec. 2013). "A suitable metocean hindcast database for the design of Marine energy converters". en. In: *International Journal of Marine Energy* 3-4, e40–e52. ISSN:

22141669. DOI: 10.1016/j.ijome.2013.11.010. URL: https://linkinghub.elsevier.com/retrieve/pii/S2214166913000362 (visited on 02/03/2020).

Bucchi, Andrea and Grant E. Hearn (Dec. 2016). "Analysis of the SEA-OWC-Clam wave energy device part B: Structural integrity analysis". en. In: *Renewable Energy* 99, pp. 253–269. ISSN: 09601481. DOI: 10.1016/j.renene.2016.06.059. URL: https://linkinghub.elsevier.com/retrieve/pii/S0960148116305833 (visited on 02/03/2020).

Cahill, Brendan and Tony Lewis ([]). "Wave period ratios and the calculation of wave power". en. In: (), p. 10.

Carnegie ([]). "Carnegie". In: (). URL: https://www.carnegiece.com/.

Charles, Elodie et al. (Mar. 2012). "Present Wave Climate in the Bay of Biscay: Spatiotemporal Variability and Trends from 1958 to 2001". en. In: *Journal of Climate* 25.6, pp. 2020–2039. ISSN: 0894-8755, 1520-0442. DOI: 10.1175/JCLI-D-11-00086.1. URL: http://journals.ametsoc.org/doi/10.1175/JCLI-D-11-00086.1 (visited on 02/03/2020).

Christensen, Lars (2005). "The wave energy challenge : the wave dragon case". en. In.

Cornett, Andrew M. (2008). "A global wave energy resource assessment". eng. In: International Offshore and Polar Engineering Conference, July 6-11, 2008, Vancouver, Canada. Collection / Collection : NRC Publications Archive / Archives des publications du CNRC: International Society of Offshore and Polar Engineers, ISOPE–2008–TPC–579.

Dean, Robert G. and Robert A. Dalrymple (1984). *Water wave mechanics for engineers and scientists*. Vol. 2. Advanced Series on Ocean Engineering. World Scientific.

Delpey, Matthias et al. (Nov. 2021). "Characterization of the wave resource variability in the French Basque coastal area based on a high-resolution hindcast". en. In: *Renewable Energy* 178, pp. 79–95. ISSN: 09601481. DOI: 10.1016/j.renene.2021.05.167. URL: https://linkinghub.elsevier.com/retrieve/pii/S0960148121008569 (visited on 07/05/2021).

Dietrich, J. C. et al. (Aug. 2012). "Performance of the Unstructured-Mesh, SWAN+ADCIRC Model in Computing Hurricane Waves and Surge". en. In: *Journal of Scientific Computing* 52.2, pp. 468–497. ISSN: 0885-7474, 1573-7691. DOI: 10.1007/s10915-011-9555-6. URL: http://link.springer.com/10.1007/s10915-011-9555-6 (visited on 02/03/2020).

DNV (2010). *Environmental Conditions and Environmental Loads*. en. Tech. rep., p. 124.

Dodet, Guillaume, Xavier Bertin, and Rui Taborda (2010). "Wave climate variability in the North-East Atlantic Ocean over the last six decades". en. In: *Ocean Modelling*.

Dufour, G et al. (2013). "EMACOP Project: Assessment of Wave Energy Resource Along France's Coastlines". en. In: *Marine Structures*, p. 10.

Eldeberky, Yasser and J.A. Battjes (1995). "Parameterization of triad interactions in wave energy models". In: *Coastal Dynamics '95*.

Elhanafi, Ahmed et al. (Oct. 2017). "Experimental and numerical investigations on the intact and damage survivability of a floating–moored oscillating water column device". en. In: *Applied Ocean Research* 68, pp. 276–292. ISSN: 01411187. DOI: 10.1016/j.apor.2017.09.007. URL: https://linkinghub.elsevier.com/retrieve/pii/S0141118717302341 (visited on 02/03/2020).

Filipot, Jean-François, Fabrice Ardhuin, and Alexander V. Babanin (Apr. 2010). "A unified deep-to-shallow water wave-breaking probability parameterization". en. In: *Journal of Geophysical Research* 115.C4, p. C04022. ISSN: 0148-0227. DOI: 10.1029/2009JC005448. URL: http://doi.wiley.com/10.1029/2009JC005448 (visited on 10/20/2022).

French-Government (2017). "Loi n 2015-992 du 17 aot 2015 relative la transition nergtique pour la croissance verte". In.

Galparsoro, Ibon et al. (Jan. 2012). "A Marine Spatial Planning Approach to Select Suitable Areas for Installing Wave Energy Converters (WECs), on the Basque Continental Shelf (Bay of Biscay)". en. In: *Coastal Management* 40.1, pp. 1–19. ISSN: 0892-0753, 1521-0421. DOI: 10.1080/08920753.2011.637483. URL: http://www.tandfonline.com/doi/abs/10.1080/08920753.2011.637483 (visited on 02/03/2020).

Goda, Yoshimi (2008). *Random seas and design of maritime structures*. en. 2. ed., Reprint. Advanced series on ocean engineering 15. New Yersey: World Scientific. ISBN: 978-981-02-3256-6.

Goda, Yoshimi, S. Haranaka, and M. Kitahata (1966). "A study on impulsive breaking wave force upon a vertical pile". Japanese. In: *Report of the Port and Harbour Institute* 5.6, pp. 1–30.

Gonçalves, Marta, Paulo Martinho, and C. Guedes Soares (Feb. 2014). "Wave energy conditions in the western French coast". en. In: *Renewable Energy* 62, pp. 155–163. ISSN: 09601481. DOI: 10.1016/j.renene.2013.06.028. URL: https://linkinghub.elsevier.com/retrieve/pii/S0960148113003212 (visited on 02/03/2020).

Hanna, Steven and David Heinold (1985). "Development and application of a simple method for evaluating air quality models". In: *American Petroleum Institute, Health and Environmental Affairs Department: Washington,WA, USA*.

Haselsteiner, Andreas F et al. (2019). "A Benchmarking Exercise on Estimating Extreme Environmental Conditions: Methodology & Baseline Results". en. In.

Hasselmann, K et al. (1973). *Measurements of wind-wave growth and swell decay during the Joint North Sea Wave Project (JONSWAP)*. Tech. rep. UDC 551.466.31. Deutches Hydrographisches Institut.

Haver, Sverre and Gudmund Kleiven (Jan. 2004). "Environmental Contour Lines for Design Purposes: Why and When?" en. In: *23rd International Conference on Offshore Mechanics and Arctic Engineering, Volume 1, Parts A and B*. Vancouver, British Columbia, Canada: ASMEDC, pp. 337–345. ISBN: 978-0-7918-3743-6 978-0-7918-3738-2. DOI: 10.1115/OMAE2004-51157. URL: https://asmedigitalcollection.asme.org/OMAE/proceedings/OMAE2004/37432/337/304302 (visited on 07/08/2021).

Heath, Tom (2003). "Islay LIMPET project monitoring final report". In: p. 40.

— (2009). "The Construction, Commissioning and Operation of the LIMPET Wave Energy Collector". en. In.

Hequette, Arnaud and David Aernouts (July 2010). "The influence of nearshore sand bank dynamics on shoreline evolution in a macrotidal coastal environment, Calais, northern France". en. In: *Continental Shelf Research* 30.12, pp. 1349–1361. ISSN: 02784343. DOI: 10.1016/j.csr.2010.04.017. URL: https://linkinghub.elsevier.com/retrieve/pii/S0278434310001561 (visited on 02/06/2023).

Holthuijsen, L.H. (2007). *Waves in Oceanic and Coastal Waters*. Cambridge University Press. ISBN: 978-0-511-61853-6.

Iglesias, G. and R. Carballo (Nov. 2009). "Wave energy potential along the Death Coast (Spain)". en. In: *Energy* 34.11, pp. 1963–1975. ISSN: 03605442. DOI: 10.1016/j.energy.2009.08.004. URL: https://linkinghub.elsevier.com/retrieve/pii/S0360544209003454 (visited on 02/03/2020).

— (Nov. 2010). "Wave energy and nearshore hot spots: The case of the SE Bay of Biscay". en. In: *Renewable Energy* 35.11, pp. 2490–2500. ISSN: 09601481. DOI: 10.1016/j.renene.2010.03.016. URL: https://linkinghub.elsevier.com/retrieve/pii/S0960148110001333 (visited on 02/03/2020).

Iglesias, G., M. López, et al. (Nov. 2009). "Wave energy potential in Galicia (NW Spain)". en. In: *Renewable Energy* 34.11, pp. 2323–2333. ISSN: 09601481. DOI: 10.1016/j.renene.2009.03.030. URL: https://linkinghub.elsevier.com/retrieve/pii/S0960148109001517 (visited on 02/03/2020).

Kami Delivand, Mitra and Jimmy Murphy (July 2022). *FMECA DataBase H2020 IMPACT D4.1*. en. Type: dataset. DOI: 10.5281/ZENODO.6962297. URL: https://zenodo.org/record/6962297 (visited on 07/11/2023).

Kármán, Theodore von (1929). *The impact on seaplance floats during landing*. Technical Notes 321. Aachen: Aerodynamical Institute of the Technical High School, p. 9.

Komen, Gerbrand Johan, Luigi Cavaleri, and Mark Donelan (1996). *Dynamics and modelling of ocean waves*. Cambridge University press. ISBN: ISBN : 0-521-57781-0.

Lastiri, Ximun et al. (Mar. 2020). "Wave Energy Assessment in the South Aquitaine Nearshore Zone from a 44-Year Hindcast". en. In: *Journal of Marine Science and Engineering* 8.3, p. 199. ISSN: 2077-1312. DOI: 10.3390/jmse8030199. URL: https://www.mdpi.com/2077-1312/8/3/199 (visited on 07/01/2020).

Leishman, JM and G Scobie (1976). *The development of wave power : A techno-economic study*. Tech. rep. National Engineering Laboratory, Glasgow.

Lian, Gunnar and Sverre K. Haver (Oct. 2016). "Estimating Long-Term Extreme Slamming From Breaking Waves". en. In: *Journal of Offshore Mechanics and Arctic Engineering* 138.5, p. 051101. ISSN: 0892-7219, 1528-896X. DOI: 10.1115/1.4033935. URL: https://asmedigitalcollection.asme.org/offshoremechanics/article/doi/10.1115/1.4033935/376491/Estimating-LongTerm-Extreme-Slamming-From-Breaking (visited on 11/06/2020).

Lim, Ho-Joon et al. (Mar. 2015). "Experimental study on plunging breaking waves in deep water". en. In: *Journal of Geophysical Research: Oceans* 120.3, pp. 2007–2049. ISSN: 21699275. DOI: 10.1002/2014JC010269. URL: http://doi.wiley.com/10.1002/2014JC010269 (visited on 07/25/2023).

Longuet-Higgins, M. S. and R. W. Stewart (Aug. 1962). "Radiation stress and mass transport in gravity waves, with application to 'surf beats'". en. In: *Journal of Fluid Mechanics* 13.4, pp. 481–504. ISSN: 0022-1120, 1469-7645. DOI: 10.1017/S0022112062000877. URL: https://www.cambridge.org/core/product/identifier/S0022112062000877/type/journal_article (visited on 02/04/2020).

Magne, Rudy et al. (2007). "Evolution of surface gravity waves over a submarine canyon". en. In.

Maisondieu, Christophe and Marc Le Boulluec (Dec. 2016). "Benefits of using a spectral hindcast database for wave power extraction assessment". en. In: *The International Journal of Ocean and Climate Systems* 7.3, pp. 83–87. ISSN: 1759-3131, 1759-314X. DOI: 10.1177/1759313116649967. URL: http://journals.sagepub.com/doi/10.1177/1759313116649967 (visited on 07/01/2020).

Martinez, A (2020). "Wave exploitability index and wave resource classification". en. In: *Renewable and Sustainable Energy Reviews*.

Mazzaretto, Ottavio Mattia (2022). "A global evaluation of the JONSWAP spectra suitability on coastal areas". en. In: *Ocean Engineering*.

Medina-Lopez, Encarnacion et al. (July 2017). "Conjectures on the Failure of the OWC Breakwater at Mutriku". en. In: *Coastal Structures and Solutions to Coastal Disasters 2015*. Boston, Massachusetts: American Society of Civil Engineers, pp. 592–603. ISBN: 978-0-7844-8030-4. DOI: 10.1061/9780784480304.063. URL: http://ascelibrary.org/doi/10.1061/9780784480304.063 (visited on 02/03/2020).

Mentaschi, L. et al. (Dec. 2013). "Problems in RMSE-based wave model validations". en. In: *Ocean Modelling* 72, pp. 53–58. ISSN: 14635003. DOI: 10.1016/j.ocemod.2013.08.003. URL: https://linkinghub.elsevier.com/retrieve/pii/S1463500313001418 (visited on 08/20/2020).

Miche, Robert (1944). "Mouvements ondulatoires de la mer en profondeur croissante ou décroissante. Première partie. Mouvements ondulatoires périodiques et cylindriques en profondeur constante". In: *Annales des Ponts et Chaussées*.

Paulsen, Bo Terp et al. (Jan. 2019). "Probability of wave slamming and the magnitude of slamming loads on offshore wind turbine foundations". en. In: *Coastal Engineering* 143, pp. 76–95. ISSN: 03783839. DOI: 10.1016/j.coastaleng.2018.10.002. URL: https://linkinghub.elsevier.com/retrieve/pii/S0378383917301928 (visited on 03/24/2021).

Penalba, Markel et al. (Aug. 2018). "Wave energy resource variation off the west coast of Ireland and its impact on realistic wave energy converters' power absorption". en. In: *Applied Energy* 224, pp. 205–219. ISSN: 03062619. DOI: 10.1016/j.apenergy.2018.04.121. URL: https://linkinghub.elsevier.com/retrieve/pii/S0306261918306895 (visited on 02/03/2020).

Poncet, Pierre-Antoine (2021). "Characterization of wave impact loading on structures at full scale : field experiment, statistical analysis and 3D advanced numerical modeling." PhD thesis. Agnlet: Université de Pau et des Pays de l'Adour.

Rasilla, Domingo et al. (Aug. 2018). "Extreme Wave Storms and Atmospheric Variability at the Spanish Coast of the Bay of Biscay". en. In: *Atmosphere* 9.8, p. 316. ISSN: 2073-4433. DOI: 10.3390/atmos9080316. URL: http://www.mdpi.com/2073-4433/9/8/316 (visited on 08/18/2023).

Reguero, B.G., I.J. Losada, and F.J. Méndez (June 2015). "A global wave power resource and its seasonal, interannual and long-term variability". en. In: *Applied Energy* 148, pp. 366–380. ISSN: 03062619. DOI: 10.1016/j.apenergy.2015.03.114. URL: https://linkinghub.elsevier.com/retrieve/pii/S030626191500416X (visited on 02/03/2020).

Robertson, Bryson et al. (Feb. 2016). "Influence of wave resource assessment methodology on wave energy production estimates". en. In: *Renewable Energy* 86, pp. 1145–1160. ISSN: 09601481. DOI: 10.1016/j.renene.2015.09.020. URL: https://linkinghub.elsevier.com/retrieve/pii/S0960148115302998 (visited on 11/12/2020).

Roland, Aron and Fabrice Ardhuin (June 2014). "On the developments of spectral wave models: numerics and parameterizations for the coastal ocean". en. In: *Ocean Dynamics* 64.6, pp. 833–846. ISSN: 1616-7341, 1616-7228. DOI: 10.1007/s10236-014-0711-z. URL: http://link.springer.com/10.1007/s10236-014-0711-z (visited on 08/26/2020).

Rosenblatt, Murray (1952). "Remarks on a Multivariate Transformation". In: *The Annals of Mathematical Statistics* 23.3, pp. 470–472. URL: http://www.jstor.org/stable/2236692..

RTE (2019). "Bilans électriques nationaux." In: URL: https://www.%20rte-france.com/fr/article/bilans-electriques-nationaux.

Santo, H. et al. (June 2015). "Decadal wave power variability in the North-East Atlantic and North Sea: wave power variability". en. In: *Geophysical Research Letters* 42.12, pp. 4956–4963. ISSN: 00948276. DOI: 10.1002/2015GL064488. URL: http://doi.wiley.com/10.1002/2015GL064488 (visited on 11/02/2020).

Sierra, Joan Pau et al. (Dec. 2017). "Assessment of the intra-annual and inter-annual variability of the wave energy resource in the Bay of Biscay (France)". en. In: *Energy* 141, pp. 853–868. ISSN: 03605442. DOI: 10.1016/j.energy.2017.09.112. URL: https://linkinghub.elsevier.com/retrieve/pii/S0360544217316328 (visited on 09/03/2020).

Stansell, Paul and Colin MacFarlane (May 2002). "Experimental Investigation of Wave Breaking Criteria Based on Wave Phase Speeds". en. In: *Journal of Physical Oceanography* 32.5, pp. 1269–1283. ISSN: 0022-3670, 1520-0485. DOI: 10.1175/1520-0485(2002)032<1269:EIOWBC>2.0.CO;2. URL: http://journals.ametsoc.org/doi/10.1175/1520-0485(2002)032%3C1269:EIOWBC%3E2.0.CO;2 (visited on 06/09/2023).

Tanimoto, K. et al. (Nov. 1987). "Impulsive Breaking Wave Forces on an Inclined Pile Exerted by Random Waves". en. In: *Coastal Engineering 1986*. Taipei, Taiwan: American Society of Civil Engineers, pp. 2288–2302. ISBN: 978-0-87262-600-3 978-0-7844-7956-8. DOI: 10.1061/9780872626003.168. URL: http://ascelibrary.org/doi/10.1061/9780872626003.168 (visited on 07/21/2023).

Thornton, Edward B. and R. T. Guza (1983). "Transformation of wave height distribution". en. In: *Journal of Geophysical Research* 88.C10, p. 5925. ISSN: 0148-0227. DOI: 10.1029/JC088iC10p05925. URL: http://doi.wiley.com/10.1029/JC088iC10p05925 (visited on 02/20/2023).

Ulazia, Alain et al. (Dec. 2017). "Wave energy trends over the Bay of Biscay and the consequences for wave energy converters". en. In: *Energy* 141, pp. 624–634. ISSN: 03605442. DOI: 10.1016/j.energy.2017.09.099. URL: https://linkinghub.elsevier.com/retrieve/pii/S0360544217316183 (visited on 02/03/2020).

Varing, Audrey et al. (2020). "Spatial distribution of wave energy over complex coastal bathymetries: development of methodologies for comparing modeled wave fields with satellite observations". en. In: *Coastal Engineering*.

Vicinanza, D., P. Contestabile, and V. Ferrante (Feb. 2013). "Wave energy potential in the northwest of Sardinia (Italy)". en. In: *Renewable Energy* 50, pp. 506–521. ISSN: 09601481. DOI: 10.1016/j.renene.2012.07.015. URL: https://linkinghub.elsevier.com/retrieve/pii/S0960148112004417 (visited on 02/03/2020).

Visbeck, Martin H et al. ([]). "The North Atlantic Oscillation: Past, present, and future". en. In: ().

Wagner, Herbrt (1932). "Über Stoß- und Gleitvorgänge an der Oberfläche von Flüssigkeiten". de. In: *ZAMM - Zeitschrift für Angewandte Mathematik und Mechanik* 12.4, pp. 193–215. ISSN: 00442267, 15214001. DOI: 10.1002/zamm.19320120402. URL: https://onlinelibrary.wiley.com/doi/10.1002/zamm.19320120402 (visited on 07/20/2023).

Whitham, Gerald (1974). *Linear and nonlinear waves*. John Wiley & Sons. ISBN: 0-471-94090-9.

Wienke, J. and H. Oumeraci (May 2005). "Breaking wave impact force on a vertical and inclined slender pile—theoretical and large-scale model investigations". en. In: *Coastal Engineering* 52.5, pp. 435–462. ISSN: 03783839. DOI: 10.1016/j.coastaleng.2004.12.008. URL: https://linkinghub.elsevier.com/retrieve/pii/S0378383904001735 (visited on 07/21/2023).

Winterstein, S R et al. (1993). "Environmental parameters for extreme response : Inverse FORM with omission factors". en. In: Innsbruck, Austria, p. 9.

Yemm, Richard et al. (2023). "Pelamis: experience from concept to connection". en. In.